



Degree Project in Electrical Engineering

Second cycle, 30 credits

# **Automatic Identification of Machine Parameters for Motor Drives**

Double degree in Electric Power Engineering

**CARLA PETTA**



# **Automatic Identification of Machine Parameters for Motor Drives**

**Double degree in Electric Power Engineering**

CARLA PETTA

Degree Programme in Electrical Engineering

Date: February 28, 2024

Supervisor: Gustaf Falk Olson

Examiner: Luca Peretti, Iustin Radu Bojoi

Royal Institute of Technology School of Electrical Engineering and Computer Science and Polytechnic of Turin Energy Department

Host company: Imperix Ltd

Supervisors at the host company: Nicolas Cherix, Simon Strobl

Swedish title: Automatisk identifiering av maskinparametrar för motor drivenheter

Swedish subtitle: Dubbel examen i elkraftteknik



## Abstract

In industrial settings, a common challenge associated with electrical machines is the lack of parameters, which are not always available from the machine manufacturer. These parameters play a crucial role in tuning the control gains of **Field-Oriented Control (FOC)**. Traditional parameter identification methods, widely accepted in the literature, are the standard IEEE tests such as DC measurement, no-load test, locked-rotor test, and short circuit test. However, their implementation can be impractical as they necessitate additional equipment that may be costly and not readily accessible.

This thesis addresses self-commissioning procedures as a solution to this challenge, aiming to automatically identify electrical parameters of machine equivalent circuits. Specifically, this study focuses on the Imperix motor testbench, comprising **Induction Machine (IM)** and **Surface Mounted Permanent Magnet Synchronous Machine (SPMSM)**. Self-commissioning is a standstill procedure that utilizes signal injection through a power converter and the available sensors, with minimal operator intervention and no additional equipment.

For the **SPMSM**, the parameters under study include the stator resistance, the synchronous inductance, and the **Permanent Magnets (PM)**-flux. The resistance is estimated through direct current injection considering the inverter non-linearity. The synchronous inductance and its saturation characteristic are examined using high-frequency sinusoidal injection with and without DC bias via a **Current Controller (CC)**, and square wave voltage injection through hysteresis control. The **PM**-flux is determined by accelerating the **SPMSM** using the **IM** as a prime mover in an open circuit configuration. This deviation from the standstill constraint of the self-commissioning procedure is necessary as the **PM**'s effect becomes visible only when the rotor speed is non-zero.

For the **IM**, the stator resistance, the leakage inductance, the rotor resistance, and the magnetizing inductance are analyzed. The stator resistance and inverter non-linearity are identified using the same method as for the **SPMSM**. The leakage inductance is tested with a high-frequency sinusoidal injection with stepped DC bias, with which the saturation characteristic is built. Then, a DC-biased low-frequency sinusoidal injection identifies the rotor resistance. The magnetizing inductance is not identified in this work because of the extensive nature of the problem and time constraints.

Comparison with standard IEEE tests serves as validation, demonstrating close alignment of the results, except for discrepancies in the unsaturated **SPMSM** synchronous inductance estimation. The introduced innovation

involves adapting existing procedures, initially developed for other AC machines, to **SPMSM** applications, for which only limited literature is available. Overall, this work makes a valuable contribution to understanding the influence of inverter non-linearity and saturation behavior on parameter identification. It also opens the door to integrating saturation effects into control algorithms, which enables dynamic adjustment of **FOC** gains, potentially enhancing control performance.

## **Keywords**

Parameter estimation, Machine vector control, Motor drives, **IM**, **Permanent Magnet Synchronous Machine (PMSM)**, **Variable Speed Drives (VSD)**.

## Sammanfattning

I industriella miljöer är en vanlig utmaning i samband med elektriska maskiner bristen på parametrar, som inte alltid är tillgängliga från maskintillverkaren. Dessa parametrar spelar en avgörande roll för att ställa in kontrollförstärkningarna för **FOC**. Traditionella metoder för parameteridentifiering, som är allmänt accepterade i litteraturen, är standard IEEE-tester som DC-mätning, nollbelastningstest, låst rotortest och kortslutningstest. Implementeringen av dessa kan dock vara opraktisk eftersom de kräver ytterligare utrustning som kan vara kostsam och svåråtkomlig.

Denna avhandling behandlar procedurer för självavstängning som en lösning på denna utmaning och syftar till att automatiskt identifiera elektriska parametrar för maskinens ekvivalenta kretsar. Studien fokuserar särskilt på Imperix motortestbänk, som består av **IM** och **SPMSM**. Självinkoppling är en stilleståndspå procedur som använder signalinjektion genom en kraftomvandlare och de tillgängliga sensorerna, med minimal operatörsintervention och utan extra utrustning.

För **SPMSM** studeras parametrarna statorresistans, synkroninduktans och **PM**-flöde. Motståndet uppskattas genom likströmsinjektion med hänsyn till växelriktarens olinjäritet. Den synkrona induktansen och dess mättnadskaraktistik undersöks med hjälp av högfrekvent sinusinjektion med och utan DC-bias via en **CC**, och fyrkantsvåginjektion genom hysteresstyrning. Flödet **PM** bestäms genom acceleration av **SPMSM** med hjälp av **IM** som drivmotor i en öppen krets-konfiguration. Denna avvikelser från stilleståndsbegränsningen i förfarandet för självavstängning är nödvändig eftersom **PM**:s effekt blir synlig först när rotorhastigheten är skild från noll.

För **IM** analyseras statorresistansen, läckinduktansen, rotorresistansen och den magnetiserande induktansen. Statorresistansen och inverterns olinjäritet identifieras med samma metod som för **SPMSM**. Läckageinduktansen testas med en högfrekvent sinusformad injektion med stegad DC-bias, med vilken mättnadskaraktistiken byggs. Därefter identifieras en DC-baserad lågfrekvent sinusinjektion rotorresistansen. Den magnetiserande induktansen identifieras inte i detta arbete på grund av problemets omfattande natur och tidsbegränsningar.

Jämförelse med standard IEEE-tester fungerar som validering och visar att resultaten ligger nära varandra, med undantag för avvikelser i uppskattningen av den omättade synkrona induktansen för **SPMSM**. Den introducerade innovationen innebär att befintliga procedurer, som ursprungligen utvecklats för andra AC-maskiner, anpassas till **SPMSM**-tillämpningar, för vilka

endast begränsad litteratur finns tillgänglig. Sammantaget ger detta arbete ett värdefullt bidrag till förståelsen av hur omriktarens icke-linjäritet och mätnadsbeteende påverkar parameteridentifieringen. Det öppnar också dörren för att integrera mätnadseffekter i regleralgoritmer, vilket möjliggör dynamisk justering av FOC-förstärkningar, vilket potentiellt kan förbättra reglerprestanda.

## Nyckelord

Parameterestimering, maskinvektorstyrning, motordrifter, Induktionsmaskiner, synkronmaskiner med permanent magnet, frekvensomriktare.



## Acknowledgments

I would like to thank imperix for allowing me to be part of their inspiring and professional environment, giving me the possibility to deepen my engineering knowledge by working on their experimental setup. A special thank goes to Nicolas Cherix, product director and co-founder of imperix, to whom I extend my heartfelt gratitude for his fundamental guidance, support, and encouragement, which have been significant to my professional development. Another pivotal figure during my journey at imperix has been the development engineer Simon Strobl. I would like to express my appreciation to him for his patience and unwavering commitment, his daily suggestions have been priceless for the understanding of the experimental part. In addition, I extend my gratitude to all my imperix colleagues who accompanied me with precious support, especially the power electronics engineer Jonathan Orsinger for his kind and constructive criticism.

Furthermore, I would like to thank my universities KTH and Polito. Particularly, irreplaceable support during this journey both in imperix and KTH comes from Professor Luca Peretti, examiner of this master thesis. His expertise, kindness, humanity, availability, and understanding make him an important professional guide on my path. Moreover, I would like to thank the KTH doctoral student Gustaf Falk Olson for his invaluable technical support in this master's thesis project. He inspired me to test new different solutions for the parameter identification procedures.

Additionally, I extend my deep appreciation to Professor Iustin Radu Bojoi, supervisor of this project in Polito, for his excellence, expertise, and dedication. His professional advice has been a vital contribution to the identification of the technical solutions implemented in this work.

Sion, Switzerland, February 2024

Carla Petta



# Contents

<b>1</b>	<b>Introduction</b>	<b>1</b>
1.1	Evolution of commissioning procedures . . . . .	1
1.2	Problem and definition . . . . .	2
1.3	Purpose . . . . .	3
1.3.1	Host company . . . . .	3
1.3.2	Academic community . . . . .	3
1.3.3	Sustainability . . . . .	3
1.4	Method . . . . .	4
1.5	Delimitations . . . . .	5
1.6	Structure of the thesis . . . . .	5
<b>2</b>	<b>Background knowledge</b>	<b>6</b>
2.1	Mechanical Dynamic Model of Motor Drives . . . . .	6
2.2	Machine Electrical Dynamic Model . . . . .	7
2.2.1	Permanent Magnet Synchronous Machine (PMSM) . . . . .	7
2.2.2	Induction Machine (IM) . . . . .	12
2.3	Magnetic saturation . . . . .	18
2.4	Inverter non-linearity . . . . .	20
2.5	Control strategies . . . . .	23
2.5.1	Rotor Field Oriented Control (RFOC) . . . . .	23
<b>3</b>	<b>Theory of parameter identification techniques</b>	<b>27</b>
3.1	Methodological classification . . . . .	27
3.1.1	Literature review of parameter identification methods for SPMSM . . . . .	28
3.1.2	Literature review of parameter identification methods for IM . . . . .	34
3.2	Parameter Estimation for SPMSM . . . . .	43
3.2.1	SPMSM stator resistance . . . . .	43

3.2.2	SPMSM synchronous inductance . . . . .	50
3.2.3	SPMSM PM-flux . . . . .	57
3.3	Parameter Estimation for IM . . . . .	61
3.3.1	IM stator resistance . . . . .	61
3.3.2	IM leakage inductance . . . . .	62
3.3.3	IM rotor resistance . . . . .	65
<b>4</b>	<b>Practical implementation</b>	<b>68</b>
4.1	Software tools . . . . .	68
4.1.1	Full self-commissioning routine . . . . .	69
4.2	Hardware tools . . . . .	70
4.2.1	Control stage . . . . .	71
4.2.2	Power stage . . . . .	72
4.2.3	Dual Motor testbench . . . . .	73
<b>5</b>	<b>Results and Analysis</b>	<b>75</b>
5.1	Results for SPMSM . . . . .	75
5.1.1	SPMSM stator resistance . . . . .	75
5.1.2	SPMSM synchronous inductance . . . . .	82
5.1.3	SPMSM PM-flux . . . . .	89
5.2	Results for IM . . . . .	92
5.2.1	IM stator resistance . . . . .	92
5.2.2	IM leakage inductance . . . . .	94
5.2.3	IM rotor resistance . . . . .	98
<b>6</b>	<b>Conclusions and Future work</b>	<b>101</b>
6.1	Conclusions . . . . .	101
6.2	Limitations . . . . .	104
6.3	Future work . . . . .	104
	<b>References</b>	<b>107</b>
<b>A</b>	<b>Electrical machines specifications</b>	<b>115</b>

## List of acronyms and abbreviations

ACG	Automated Code Generation
CC	Current Controller
DFT	Discrete Fourier Transform
DTC	Direct Torque Control
DUT	Device Under Test
EMF	Electromagnetic Force
FEA	Finite Element Analysis
FOC	Field-Oriented Control
IM	Induction Machine
LLS	Linear least-squares
LUT	Lookup Table
MLR	Multiple Linear Regression
MMF	Magneto Motive Force
OL	Open Loop
PI	Proportional Integral
PM	Permanent Magnets
PMSM	Permanent Magnet Synchronous Machine
PR	Proportional Resonant
PWM	Pulse Width Modulation
RCP	Rapid Control Prototyping
RFOC	Rotor Field Oriented Control
RMS	Root Mean Square
SC	Speed Controller
SDK	Software Development Kit
SMO	Sliding-Mode Observer

SPMSM	Surface Mounted Permanent Magnet Synchronous Machine
SynRM	Synchronous Reluctance Machines
VSD	Variable Speed Drives

# List of Symbols Used

The following symbols will be later used within the body of the thesis.

$\mathbf{i}_m^s$	Magnetizing current space vector in the $\alpha\beta 0$ stationary reference frame
$\mathbf{i}_r^r$	Rotor current space vector in the rotor reference frame
$\mathbf{i}_R^s$	Rotor current space vector in the $\alpha\beta 0$ stationary reference frame in the inverse- $\Gamma$ equivalent circuit
$\mathbf{i}_r^s$	Rotor current space vector in the $\alpha\beta 0$ stationary reference frame in the T-circuit
$\mathbf{i}_R^{dq0}$	Rotor current space vector in the dq0 reference frame in the inverse- $\Gamma$ equivalent circuit
$\mathbf{i}_s^s$	Stator current space vector in the $\alpha\beta 0$ stationary reference frame
$\mathbf{i}_s^{dq0}$	Stator current space vector in the dq0 reference frame
$\mathbf{v}_r^r$	Rotor voltage space vector in the rotor reference frame
$\mathbf{v}_s^s$	Stator voltage space vector in the $\alpha\beta 0$ stationary reference frame
$\mathbf{v}_s^{dq0}$	Stator voltage space vector in the dq0 reference frame
$\omega_e$	Synchronous angular speed of the dq0 reference frame
$\omega_m$	Mechanical angular rotor speed
$\omega_r$	Electrical angular rotor speed
$\omega_{slip}$	Angular slip speed
$\psi_r^r$	Rotor flux space vector in the rotor reference frame

$\psi_R^s$	Rotor flux space vector in the $\alpha\beta 0$ stationary reference frame in the inverse- $\Gamma$ equivalent circuit
$\psi_r^s$	Rotor flux linkage space vector in the $\alpha\beta 0$ stationary reference frame
$\psi_r^s$	Rotor flux space vector in the $\alpha\beta 0$ stationary reference frame in the T-circuit for IM
$\psi_R^{dq0}$	Rotor flux space vector in the dq0 reference frame in the inverse- $\Gamma$ equivalent circuit
$\psi_s^s$	Stator flux space vector in the $\alpha\beta 0$ stationary reference frame
$\theta$	Phase angle of the rotor flux linkage space vector in the $\alpha\beta 0$ stationary reference frame
$\theta_e$	Synchronous angle between d-axis and $\alpha$ -axis
$\theta_r$	Rotor position in the $\alpha\beta 0$ stator reference frame
$L_M$	Transformed magnetizing inductance in the inverse- $\Gamma$ equivalent circuit
$L_m$	Magnetizing inductance in the T-circuit
$L_s$	Synchronous inductance
$L_\sigma$	Total leakage inductance in the inverse- $\Gamma$ equivalent circuit
$L_{rl}$	Rotor leaked edge inductance in the T-circuit
$L_{sl}$	Stator leaked edge inductance in the T-circuit
$R_R$	Transformed rotor resistance in the inverse- $\Gamma$ equivalent circuit
$R_r$	Rotor resistance in the T-circuit
$R_s$	Stator resistance



# Chapter 1

## Introduction

### 1.1 Evolution of commissioning procedures

The general definition of "commissioning" in an electrical environment is the systematic process of testing equipment, systems, or facilities to ensure that they meet the design and operational requirements of the owner.

In the field of electrical machines and drives, a preliminary action, necessary to perform the normal routine of a motor (start-up and the various control strategies), is the knowledge of machine parameters. Electrical machines are characterized by a nameplate in which basic information under rated and limit conditions is provided, such as current, voltage, power, torque, and speed. On the other side, electrical parameters (resistances, inductances of the machine's equivalent circuit) and mechanical parameters (inertia and viscous friction coefficient) should be found in the datasheet. However, the datasheet of the available machines in the market does not always present all these necessary information.

This represents a typical problem in industrial environments. The motor commissioning is thus related to the development of control techniques for **Variable Speed Drives (VSD)**. For this reason, the subject has been dealt with since the 1990s, as shown by the publication of Peter Vas in [1]. In fact, around the 1980s, **VSD** were introduced. Thanks to the development of AC control techniques, AC motors spread into new fields of application where smooth control is required, partly replacing the DC motors used until then.

The advances in semiconductor technology led to improvements in power electronics components (for instance higher switching frequencies), which made **VSD** even more popular in industrial and commercial settings. With the ever-changing industrial sector over the years, the need to

automate manufacturing processes has increased. Therefore, electric motor commissioning processes have also been automated to keep up.

Motor commissioning is always evolving in parallel with industrial and electric drive progress, the reason why different methods have been developed over the years, as discussed in Section 3.1.

## 1.2 Problem and definition

The subject of self-commissioning for AC motor drives, addressed in this thesis, refers to automatically configuring and tuning a motor drive system. Looking at the structure of the words, it is possible to derive its definition.

The meaning of "commissioning" is already presented in Section 1.1. The use of the prefix "self" highlights the automatic nature of this process, with minimal or no user involvement [2]. Self-commissioning is an automatic procedure performed when the machine is operated (online) or one time before its starting up (offline). It allows the initialization of the drive system and ensures that it operates efficiently and effectively in a given application. Specifically, calibration, identification of machine parameters, and automatic tuning are involved in this routine.

Different methods are presented in the literature, for instance, the standard tests proposed by the IEEE in [3] such as the DC, no-load, and locked-rotor tests. These tests are not automated and, depending on the particular application, it is not always possible to perform them on machines already placed on site. Their drawbacks are the use of additional equipment, which could be expensive and not always available, and the request of considerable time and effort, which, in an industrial environment, are translated into costs and loss of production. Moreover, the accuracy of machine parameters can be affected by the method and the type of equipment used. In fact, in high-performance control in which fast response, zero steady-state error, and accurate reference tracking are required from the motor drive, accurate knowledge of machine parameters is fundamental [4]. Optimization of costs, time, and accuracy is achieved by automating the process.

More specifically, the research question is:

How can a state-of-the-art automatic identification procedure of parameters be implemented for the Imperix motor testbench, which is composed of **Induction Machine (IM)** and **Surface Mounted Permanent Magnet Synchronous Machine (SPMSM)**?

## 1.3 Purpose

### 1.3.1 Host company

The main actor of this project is the Swiss company Imperix. The company offers high-end control and power solutions for research laboratories in power electronics. As part of its R&D activities, Imperix seeks to continuously develop state-of-the-art control techniques for all sorts of power converters. It provides its customers with a set of examples of standard control techniques implemented on its products, creating a publicly accessible knowledge base via the website. The continuously growing knowledge base is essential to effectively support its customers, mostly world-leading universities and industries. This purpose involves also electrical drives. Imperix wishes to include the procedure under study of self-commissioning for motor drives in its existing **Field-Oriented Control (FOC)** examples. **FOC** is a control technique that relies on knowledge of machine parameters for tuning.

Incorporating the self-commissioning procedure into Imperix's knowledge base will strengthen its support for electrical drives, potentially enhancing competitiveness in the market and offering customers more advanced solutions.

### 1.3.2 Academic community

For the academic community, this work is scientifically relevant because it keeps track of the progress made in the field of self-commissioning over the years, summarizing a very vast and constantly evolving topic. This could serve as a valuable resource for identifying machine parameters in the future. Moreover, this work contributes to develop scientific knowledge on machine parameter identification because it adapts existing procedures on new applications.

### 1.3.3 Sustainability

The final purpose is addressed to the world and the sustainability process. The project contributes in an indirect way to sustainability questions because it addresses techniques that do not require additional hardware, which means a reduction of electronic waste, by promoting sustainable design. This improves also the long-term impact, reducing maintenance and improving durability.

## 1.4 Method

To address the research question defined in Section 1.2, the following goals have to be reached.

### Goal 1 Machine modeling:

**Task 1** Define the theoretical knowledge of the AC motors.

**Task 2** List all the parameters that should be identified for FOC.

### Goal 2 Literature review:

**Task 1** Study and classify existing parameters' identification techniques for the AC motors. This set a full understanding of the possible procedures available from the literature.

**Task 2** Select and justify which method will be implemented among those available from the literature.

### Goal 3 Simulation design:

**Task 1** Implement the chosen method in simulation using the parameters provided by the machine manufacturer.

### Goal 4 Experimental validation:

**Task 1** Test and validate the selected self-commissioning procedures on the experimental imperix motor testbench, identifying strengths and drawbacks of the tested procedure.

**Task 2** Test and validate the IEEE standard tests in [3] and [5] on the imperix motor testbench, identifying strengths and drawbacks of the tested procedure.

### Goal 5 Comparison and conclusions:

**Task 1** Compare the obtained results from the self-commissioning procedures and the IEEE standard.

- If the results of both self-commissioning and standard tests align and this comparison can be scientifically explained, the self-commissioning method can be considered technically relevant.
- If the results of both self-commissioning and standard tests do not align, a conclusive determination cannot be made.

## 1.5 Delimitations

The following section aims to establish the boundaries and limits of the thesis project to clearly define what falls outside its scope. Due to time constraints, this project only includes offline identification of machine parameters through machine excitation with test signals while at a standstill, and not the online techniques, which instead require tracking the parameters during operation. These last techniques result in a more advanced study of the topic because they take into consideration the effects of the environment, such as temperature changes, on the drive system during work time. An offline procedure allows to have a first picture of motor parameters.

Furthermore, due to time constraints, only the electrical parameters of the machine's equivalent circuit are estimated in this study, while the mechanical parameters are not addressed.

Another limit is due to the available equipment in the laboratory, which restricts the power rating (up to 15 kW) and the types of machines investigated (**IM** and **SPMSM**). Higher power ranges cannot be tested due to a lack of corresponding equipment.

Additionally, only the **FOC** is considered, and no other control techniques, since this is the most sensitive control strategy to parameter variations between those implemented by the company imperix (**Direct Torque Control (DTC)**, scalar voltage-frequency control, and **Rotor Field Oriented Control (RFOC)**).

## 1.6 Structure of the thesis

Chapter **2** gives the theoretical background related to power electronics, electrical machines, and drives, necessary to understand the theoretical method for the chosen identification technique described in Chapter **3**. Following this, Chapter **4** gives an overview of the software and hardware tools used such as the general structure of Simulink models and the imperix experimental setup, respectively. Thereafter, Chapter **5** presents the result achieved, and discusses the drawbacks and the advantages of the different methods. Finally, the conclusion and the future works are shown in Chapter **6**.

## Chapter 2

# Background knowledge

In this chapter, the dynamic model of the two types of motors is described with their respective equations. The mechanical model is presented in Section 2.1 and the electrical one in Section 2.2.1 for the SPMSM and in Section 2.2.2 for the IM. Specific focus on the inverter and its effects on the self-commissioning methods is in Section 2.4. Subsequently, the theoretical background on the control strategies for motor drives is given in Section 2.5, specifically, the principle of RFOC in Section 2.5.1.

## 2.1 Mechanical Dynamic Model of Motor Drives

The dynamic model of an electric motor drive can be divided into electrical dynamic and mechanical dynamic. These are studied, following the reference [6]. The mechanical torque  $\tau_m$  is the input of the mechanical Equation (2.1),

$$J \frac{d\omega_m}{dt} = \tau_m - b_f \omega_m - \tau_L \quad (2.1)$$

where  $J$  is the inertia of the electric drive,  $b_f$  is the friction coefficient,  $\tau_L$  is the load torque.

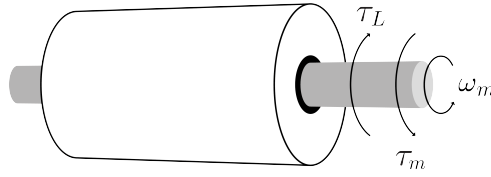


Figure 2.1: Rotating motor physics.

Specifically, the Imperix electric drive is a dual motor testbench, composed of two electrical machines coupled through the same shaft. One of the units performs as a motor/generator ( $\tau_m$ ), while the other unit serves as a variable load ( $\tau_L$ ). More details about the testbench are provided in Section 4.2.3.

## 2.2 Machine Electrical Dynamic Model

### 2.2.1 Permanent Magnet Synchronous Machine (PMSM)

In this section, the background theory necessary for the SPMSM parameter identification is explained. First, the general equation for the Permanent Magnet Synchronous Machine (PMSM) are defined, then they are particularized for the SPMSM. First, the ideal PMSM model is described under the following hypotheses, following the literature by A. Cavagnino [7]:

- no magnetic saturation;
- stator windings with theoretical sinusoidal distribution;
- no spatial harmonics in the Magneto Motive Force (MMF) and magnetic field distributions.

and the following conventions are used:

- motor conventions for supply voltages and currents;
- anti-clockwise sequence order of the stator winding triad;
- quadrature axis of rotor  $90^\circ$  in advance of direct axis.

Later in the analysis, the saturation effect is introduced in the model in Section 2.3. In the three-phase abc reference frame, the electrical and

magnetic vector equations are defined in Equation (2.2).

$$\begin{aligned}\mathbf{v}_s - R_s \mathbf{i}_s - \frac{d\boldsymbol{\psi}_s}{dt} &= 0 \\ \boldsymbol{\psi}_s &= L_s \mathbf{i}_s + \boldsymbol{\psi}_r\end{aligned}\quad (2.2)$$

where

$$\mathbf{v}_s = \begin{bmatrix} v_{sa} \\ v_{sb} \\ v_{sc} \end{bmatrix}; \quad \mathbf{i}_s = \begin{bmatrix} i_{sa} \\ i_{sb} \\ i_{sc} \end{bmatrix}; \quad \boldsymbol{\psi}_s = \begin{bmatrix} \psi_{sa} \\ \psi_{sb} \\ \psi_{sc} \end{bmatrix} \quad (2.3)$$

The subscript ‘s’ and ‘r’ identify the stator and rotor quantities, and the subscript indicates the phase of the reference frame. The three-phase reference frame is introduced because it is used for the single-phase configuration by L. Peretti in [8].

Subsequently, the electrical Equation (2.2) is transformed into the two-phase model  $\alpha\beta 0$  in Equation (2.5), thanks to the transformation matrix in Equation (2.4), where  $\mathbf{x}$  is a generic electric or magnetic quantity ( $\mathbf{v}$ ,  $\mathbf{i}$  or  $\boldsymbol{\psi}$ ).

$$\mathbf{x}_s^s = \begin{bmatrix} x_{s\alpha} \\ x_{s\beta} \\ x_{s0} \end{bmatrix} = \frac{2}{3} \cdot \begin{bmatrix} 1 & -1/2 & -1/2 \\ 0 & \sqrt{3}/2 & -\sqrt{3}/2 \\ 1/2 & 1/2 & 1/2 \end{bmatrix} \cdot \begin{bmatrix} x_{sa} \\ x_{sb} \\ x_{sc} \end{bmatrix} \quad (2.4)$$

Equation (2.5) is represented with the equivalent circuit in the  $\alpha\beta 0$  stationary reference frame in Figure 2.2. It models the electrical behavior of the stator because the **PMSM** is supplied from the stator side. Indeed, the **Permanent Magnets (PM)** are on the rotor side. The stator circuit is composed of the stator resistance  $R_s$  (representing the copper losses) in series with the synchronous inductance  $L_s$  (equivalent inductance of self-inductance and mutual-inductance) and with a voltage source, that represents the back-**Electromagnetic Force (EMF)**  $\mathbf{E}^s$  induced in the stator windings by the rotor magnetic field.

$$\begin{aligned}\mathbf{v}_s^s - R_s \mathbf{i}_s^s - \frac{d\boldsymbol{\psi}_s^s}{dt} &= 0 \\ \boldsymbol{\psi}_s^s &= L_s \mathbf{i}_s^s + \boldsymbol{\psi}_r^s\end{aligned}\quad (2.5)$$

where  $\boldsymbol{\psi}_r^s = \boldsymbol{\psi}_r^s e^{j\theta}$  is the rotor flux linkage, which is produced by the permanent magnets.



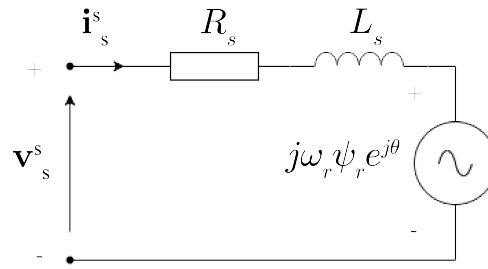


Figure 2.2: Synchronous machine dynamic vector equivalent circuit in the  $\alpha\beta 0$  stationary reference frame.

The derivative of the flux  $\psi_s^s$  in Equation (2.5) is:

$$\frac{d\psi_s^s}{dt} = L_s \frac{d\mathbf{i}_s^s}{dt} + j\omega_e \psi_r^s e^{j\theta} \quad (2.6)$$

Substituting Equation (2.6) in Equation (2.5),

$$L_s \frac{d\mathbf{i}_s^s}{dt} = \mathbf{v}_s^s - R_s \mathbf{i}_s^s - \underbrace{j\omega_e \psi_r^s e^{j\theta}}_{\mathbf{E}^s} \quad (2.7)$$

$\theta$  is the phase of the rotor flux  $\psi_r^s$  and the synchronous angle  $\theta_e$  is the angle between the  $\alpha$ -axis and the d-axis, (whose time derivative is the synchronous speed  $\omega_e$ ). Figure 2.3 clarifies the reference frame definition.

In perfect field-oriented conditions, the actual flux angle  $\theta$  and the synchronous coordinate system used in the dq0 transformation  $\theta_e$  are equal. In other words, the d-axis of the rotor should overlap the rotor flux linkage  $\psi_r^s$ . Moreover, since the slip in the **SPMSM** is null, the synchronous position  $\theta_e$  corresponds to the rotor position  $\theta_r$ .

$$\theta = \theta_e = \theta_r \quad (2.8)$$

The  $\alpha\beta 0$  reference frame is rotated at the angle  $\theta_e$ , through the complex exponential in Equation (2.9), where  $\omega_e = \frac{d\theta_e}{dt}$ .

$$\mathbf{x}^{dq0} = e^{-j\omega_e t} \mathbf{x}^s \quad (2.9)$$

Substituting Equation (2.9) in Equation (2.7) in perfect field orientation

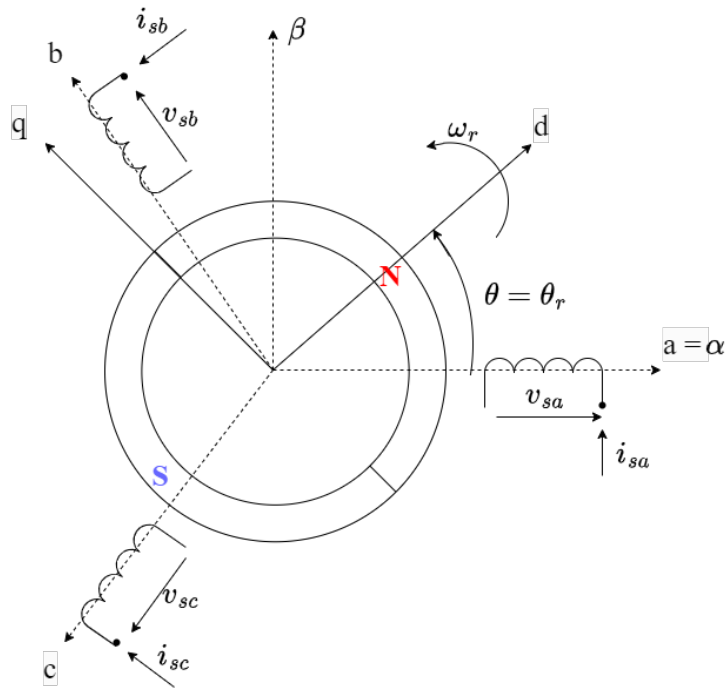


Figure 2.3: Reference frame definition for **SPMSM**.

results in Equation (2.10).

$$L_s \frac{d(e^{j\theta_e} \mathbf{i}_s^{dq0})}{dt} = e^{j\theta_e} \mathbf{v}_s^{dq0} - R_s e^{j\theta_e} \mathbf{i}_s^{dq0} - j\omega_e \psi_r \quad (2.10)$$

Simplifying the notation, the electrical dynamic is transformed to dq0 synchronous coordinates in Equation (2.11) in matrix form.

$$\mathbf{L}_s \frac{d\mathbf{i}_s^{dq0}}{dt} = \mathbf{v}_s^{dq0} - (R_s \mathbf{I} + \mathbf{J} \omega_e L_s) \mathbf{i}_s^{dq0} - \mathbf{J} \omega_e \psi_r \quad (2.11)$$

where,

$$\mathbf{L}_s = \begin{bmatrix} L_d & 0 \\ 0 & L_q \end{bmatrix}, \quad \mathbf{I} = \begin{bmatrix} 1 & 0 \\ 0 & 1 \end{bmatrix}, \quad \mathbf{J} = \begin{bmatrix} 0 & -1 \\ 1 & 0 \end{bmatrix}, \quad \boldsymbol{\psi}_r = \begin{bmatrix} \psi_r \\ 0 \end{bmatrix} \quad (2.12)$$

Subsequently, the voltage equations are written in component form, whose equivalent circuit is given in Figure 2.4.

$$\begin{aligned}
L_d \frac{di_{s,d}}{dt} &= v_{s,d} - R_s i_{s,d} + \omega_r L_q i_{s,q} \\
L_q \frac{di_{s,q}}{dt} &= v_{s,q} - R_s i_{s,q} - \omega_r (L_d i_{s,d} + \psi_r)
\end{aligned} \tag{2.13}$$

The **SPMSM** is assumed isotropic, which is reflected in the condition Equation (2.14).

$$L_d \approx L_q = L_s \tag{2.14}$$

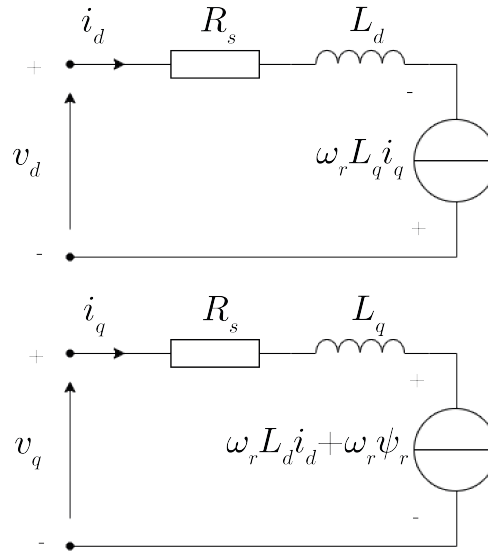


Figure 2.4: Dynamic equivalent circuit for the **PMSM** in d and q axis.

In steady-state the time derivative is null, so the steady-state equations for the **SPMSM** are given in Equation (2.15). This circuit is used for the self-commissioning procedure from Chapter 3.

$$\begin{aligned}
v_{s,d} &= R_s i_{s,d} - \omega_r L_s i_{s,q} \\
v_{s,q} &= R_s i_{s,q} + \omega_r (L_s i_{s,d} + \psi_r)
\end{aligned} \tag{2.15}$$

To complete the model of the **PMSM**, the mechanical torque  $\tau_m$  is calculated through the vector product of flux and current vectors, solved in Equation (2.16).

$$\tau_m = \frac{3n_p}{2K^2} [\psi_r i_{s,q} + (L_d - L_q) i_{s,d} i_{s,q}] \tag{2.16}$$

where  $n_p$  are the pole pairs and  $K$  is the scaling constant equal to 1 for

peak-value scaling,  $\frac{1}{\sqrt{(2)}}$  for **Root Mean Square (RMS)**-value scaling, and  $\sqrt{\left(\frac{3}{2}\right)}$  for power-invariant scaling. The only contribution of torque in a **SPMSM** comes from the **PM**. The reluctant torque  $\frac{3n_p}{2K^2} (L_{s,d} - L_{s,q}) i_{s,d} i_{s,q}$  is canceled since the reluctance all around the rotor circumference is assumed constant. In conclusion, substituting Equation (2.14) in Equation (2.16) results in Equation (2.17).

$$\tau_m = \frac{3n_p}{2K^2} \psi_r i_{s,q} \quad (2.17)$$

### 2.2.2 Induction Machine (IM)

First, the **IM** circuit from the standard 112-2017 [3] is introduced in Figure 2.5. Subsequently, the demonstration and the different types of **IM** electrical circuits useful for the self-commissioning algorithm are presented.

The parameters in the T-circuit model the physical behavior of the **IM**.  $R_s$  is the stator winding resistance representing the copper losses.  $L_{ls}$  is the total stator leakage inductance that includes all the effects of slot leakage, tooth tip leakage, end-winding leakage, leakage due to harmonics, slot skewing leakage, and pole leakage. The rotor quantities are referred to the stator side.  $R_r$  is the rotor resistance which models the copper losses in the winding resistance in the case of wound rotor induction motor and rotor bars' resistance for squirrel cage rotor.  $L_{lr}$  is the leakage inductance attributed to flux leakage due to rotor slots, slot skewing, and harmonics. The middle branch consists of a magnetizing inductance  $L_m$ , in parallel with the core loss equivalent resistance  $R_{Fe}$  (in this case neglected).  $L_m$  represents the fundamental harmonic of the rotating magnetic field at the polarity  $n_p$ . [2].

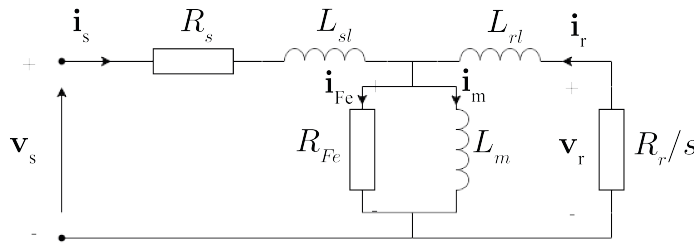


Figure 2.5: Steady-state vector T-equivalent circuit of a squirrel cage **IM** from the standard 112-2017 [3].

The ideal model is described by following the hypotheses from the reference in [2]:

- no magnetic saturation, so constant inductance;
- stator and rotor windings (and so **MMF**) with theoretical sinusoidal distribution;
- perfectly isotropic (slot openings neglected);
- perfectly cylindrical rotor with no saliencies;
- perfect stator and rotor laminations, which result in null eddy currents;
- hysteresis effects neglected in both stator and rotor;
- the magnetic flux lines always cross the air gap radially.

Later in the analysis, the saturation effect is introduced in the model in Section 2.3.

$$\begin{aligned} \mathbf{v}_s &= R_s \mathbf{i}_s + \frac{d\boldsymbol{\psi}_s}{dt} \\ \mathbf{v}_r &= R_r \mathbf{i}_r + \frac{d\boldsymbol{\psi}_r}{dt} \end{aligned} \quad (2.18)$$

where

$$\mathbf{v}_s = \begin{bmatrix} v_{sa} \\ v_{sb} \\ v_{sc} \end{bmatrix}; \quad \mathbf{i}_s = \begin{bmatrix} i_{sa} \\ i_{sb} \\ i_{sc} \end{bmatrix}; \quad \boldsymbol{\psi}_s = \begin{bmatrix} \psi_{sa} \\ \psi_{sb} \\ \psi_{sc} \end{bmatrix} \quad (2.19)$$

$$\mathbf{v}_r = \begin{bmatrix} v_{ra} \\ v_{rb} \\ v_{rc} \end{bmatrix}; \quad \mathbf{i}_r = \begin{bmatrix} i_{ra} \\ i_{rb} \\ i_{rc} \end{bmatrix}; \quad \boldsymbol{\psi}_r = \begin{bmatrix} \psi_{ra} \\ \psi_{rb} \\ \psi_{rc} \end{bmatrix} \quad (2.20)$$

In matrix form, the model of the **IM** is:

$$\begin{aligned} \begin{bmatrix} v_{sa} \\ v_{sb} \\ v_{sc} \end{bmatrix} &= \begin{bmatrix} R_s & 0 & 0 \\ 0 & R_s & 0 \\ 0 & 0 & R_s \end{bmatrix} \cdot \begin{bmatrix} i_{sa} \\ i_{sb} \\ i_{sc} \end{bmatrix} + \frac{d}{dt} \begin{bmatrix} \psi_{sa} \\ \psi_{sb} \\ \psi_{sc} \end{bmatrix} \\ \begin{bmatrix} v_{ra} \\ v_{rb} \\ v_{rc} \end{bmatrix} &= \begin{bmatrix} R_r & 0 & 0 \\ 0 & R_r & 0 \\ 0 & 0 & R_r \end{bmatrix} \cdot \begin{bmatrix} i_{ra} \\ i_{rb} \\ i_{rc} \end{bmatrix} + \frac{d}{dt} \begin{bmatrix} \psi_{ra} \\ \psi_{rb} \\ \psi_{rc} \end{bmatrix} \end{aligned} \quad (2.21)$$

Subsequently, the electrical equation is transformed into the two-phase model

thanks to the transformation matrix  $T$ .

$$\mathbf{x}_s^s = \begin{bmatrix} x_{s\alpha} \\ x_{s\beta} \\ x_{s0} \end{bmatrix} = \frac{2}{3} \cdot \begin{bmatrix} 1 & -1/2 & -1/2 \\ 0 & \sqrt{3}/2 & -\sqrt{3}/2 \\ 1/2 & 1/2 & 1/2 \end{bmatrix} \cdot \begin{bmatrix} x_{sa} \\ x_{sb} \\ x_{sc} \end{bmatrix} = T\mathbf{x}_s \quad (2.22)$$

where  $x$  is a generic electric or magnetic quantity ( $v$ ,  $i$  or  $\psi$ ).

Similarly as for the **SPMSM** in Section 2.2.1, the stator voltage equation in the stator reference frame is given in Equation (2.23)

$$\mathbf{v}_s^s - R_s \mathbf{i}_s^s - \frac{d\boldsymbol{\psi}_s^s}{dt} = 0 \quad (2.23)$$

Unlike the **SPMSM** in which the rotor is only characterized by the **PM**, the rotor in a **IM** has short-circuited windings or squirrel cage. For this reason, the rotor voltage equation in the rotor reference frame is given in Equation (2.24).

$$\mathbf{v}_r^r - R_r \mathbf{i}_r^r - \frac{d\boldsymbol{\psi}_r^r}{dt} = 0 \quad (2.24)$$

There are two different reference frames: the  $\alpha_s\beta_s0_s$  stator reference frame fixed to the stator in Equation (2.23), indicated with the superscript "s"; the  $\alpha_r\beta_r0_r$  rotor reference frame fixed to the rotor in Equation (2.24), indicated with the superscript "r". To simplify the notation, all the electrical quantities are referred to one reference frame. The rotor equation is transformed to the stationary reference frame, so the rotor space vectors are rotated at an angle equal to the rotor position with respect to the stationary reference frame  $\theta_r$ .

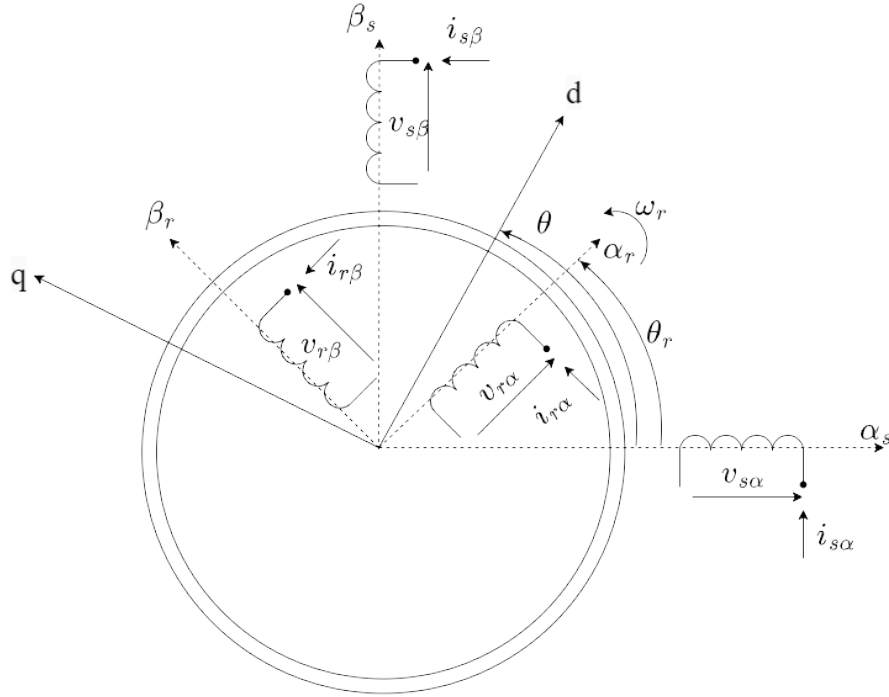
The position is

$$\begin{aligned} \mathbf{i}_r^s &= e^{j\theta_r} \mathbf{i}_r^r \\ \boldsymbol{\psi}_r^s &= e^{j\theta_r} \boldsymbol{\psi}_r^r \end{aligned} \quad (2.25)$$

The reference frames of the **IM** are shown in Figure 2.6 (which is an original hand-drawn representation like all the figures in this report).

Substituting Equation (2.25) in the Equation (2.24) and assuming  $\mathbf{v}_r^r = 0$  since the rotor windings are short-circuited, Equation (2.26) is found.

$$\begin{aligned} 0 - R_r e^{-j\theta_r} \mathbf{i}_r^s - \frac{d(e^{-j\theta_r} \boldsymbol{\psi}_r^s)}{dt} &= 0 \\ \Rightarrow -R_r e^{-j\theta_r} \mathbf{i}_r^s - \left( -j\omega_r e^{-j\theta_r} \boldsymbol{\psi}_r^s + e^{-j\theta_r} \frac{d\boldsymbol{\psi}_r^s}{dt} \right) &= 0 \\ \Rightarrow j\omega_r \boldsymbol{\psi}_r^s - R_r \mathbf{i}_r^s - \frac{d\boldsymbol{\psi}_r^s}{dt} &= 0. \end{aligned} \quad (2.26)$$

Figure 2.6: Reference frame of the **IM**.

In conclusion, the voltage equations of the **IM** in the  $\alpha_s\beta_s0_s$  stator reference frame are:

$$\begin{aligned}\frac{d\psi_s^s}{dt} &= \mathbf{v}_s^s - R_s \mathbf{i}_s^s \\ \frac{d\psi_r^s}{dt} &= j\omega_r \psi_r^s - R_r \mathbf{i}_r^s\end{aligned}\quad (2.27)$$

Subsequently, the magnetic equations are specified. The airgap flux  $\psi_a^s$  is related to the magnetizing inductance  $L_m$ :

$$\psi_a^s = L_m \mathbf{i}_m^s, \quad (2.28)$$

where

$$\mathbf{i}_m^s = \mathbf{i}_s^s + \mathbf{i}_r^s \quad (2.29)$$

The stator flux  $\psi_s^s$  and the rotor flux  $\psi_r^s$  in  $\alpha\beta0$  stator reference frame are

$$\begin{aligned}\psi_s^s &= L_m \mathbf{i}_m^s + L_{sl} \mathbf{i}_s^s \\ \psi_r^s &= L_m \mathbf{i}_m^s + L_{rl} \mathbf{i}_r^s\end{aligned}\quad (2.30)$$

Substituting Equation (2.30) in Equation (2.27) the T-circuit equations are found

$$\begin{aligned} \mathbf{v}_s^s - R_s \mathbf{i}_s^s - L_{sl} \frac{d\mathbf{i}_s^s}{dt} - L_m \frac{d\mathbf{i}_m^s}{dt} &= 0 \\ j\omega_r \psi_r^s - R_r \mathbf{i}_r^s - L_{rl} \frac{d\mathbf{i}_r^s}{dt} - L_m \frac{d\mathbf{i}_m^s}{dt} &= 0 \end{aligned} \quad (2.31)$$

Although the T-equivalent dynamic model is physically relevant, this circuit is not used for the control because it is over-parametrized. In fact, due to Equation (2.29), the three currents ( $\mathbf{i}_m^s, \mathbf{i}_s^s, \mathbf{i}_r^s$ ) are not linearly independent. For this reason, the circuit can be further simplified by considering one total leakage inductance.

Substituting Equation (2.29) in Equation (2.28), the flux in Equation (2.30) can be rewritten as:

$$\begin{aligned} \psi_s^s &= L_s \mathbf{i}_s^s + L_m \mathbf{i}_r^s \\ \psi_r^s &= L_m \mathbf{i}_s^s + L_r \mathbf{i}_r^s \end{aligned} \quad (2.32)$$

where,

$$\begin{aligned} L_s &= L_m + L_{sl} \\ L_r &= L_m + L_{rl} \end{aligned} \quad (2.33)$$

The inverse- $\Gamma$  equivalent circuit is relevant for the control of the machine. Its parameters are estimated in this work, but as explained before, they do not have a physical meaning. From the T-circuit, the equations for the inverse- $\Gamma$  equivalent circuit are derived with the position in Equation (2.34),

$$\begin{aligned} \psi_R^s &= b \psi_r^s \\ \mathbf{i}_R^s &= \frac{\mathbf{i}_r^s}{b} \end{aligned} \quad (2.34)$$

where  $b$  is a transformation factor to be chosen.

$$\begin{aligned} \psi_s^s &= L_s \mathbf{i}_s^s + b L_m \mathbf{i}_R^s \\ \psi_r^s &= b L_m \mathbf{i}_s^s + b^2 L_r \mathbf{i}_R^s \end{aligned} \quad (2.35)$$

By choosing  $b$  such that the stator and rotor currents have equal coefficients in Equation (2.35) with the rotor quantities, i.e.,  $b L_m = b^2 L_r$   $b = L_m / L_r$ , the leakage inductance on the rotor side is eliminated.

$$\begin{aligned} \psi_s^s &= L_s \mathbf{i}_s^s + \frac{L_m^2}{L_r} \mathbf{i}_R^s \\ \psi_r^s &= \frac{L_m^2}{L_r} (\mathbf{i}_s^s + \mathbf{i}_R^s) \end{aligned} \quad (2.36)$$



where

$$L_M = \frac{L_m^2}{L_r}$$

$$L_\sigma = L_s - L_M = L_s - \frac{L_m^2}{L_r} = \frac{L_m (L_{sl} + L_{rl} + L_{sl}L_{rl})}{L_m L_{rl}} \approx L_{sl} + L_{rl} \quad (2.37)$$

$$\begin{aligned} \psi_s^s &= L_\sigma \mathbf{i}_s^s + L_M \mathbf{i}_M^s \\ \psi_r^s &= L_M \mathbf{i}_M^s \end{aligned} \quad (2.38)$$

The transformed rotor resistance is:

$$R_R = \left( \frac{L_m}{L_r} \right)^2 R_r \quad (2.39)$$

Substituting Equation (2.38) in Equation (2.27) the inverse  $\Gamma$ -circuit equations are found

$$\begin{aligned} \mathbf{v}_s^s - R_s \mathbf{i}_s^s - L_\sigma \frac{d\mathbf{i}_s^s}{dt} - L_M \frac{d\mathbf{i}_M^s}{dt} &= 0 \\ j\omega_r \psi_R^s - R_R \mathbf{i}_R^s - L_M \frac{d\mathbf{i}_M^s}{dt} &= 0 \end{aligned} \quad (2.40)$$

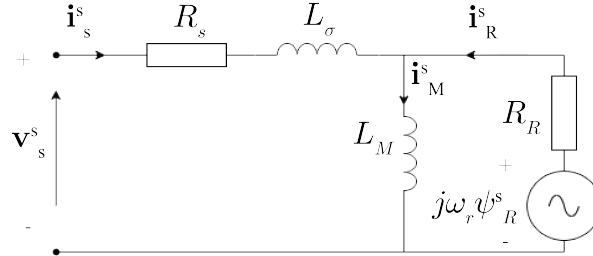


Figure 2.7: Dynamic inverse- $\Gamma$  equivalent circuit described by Equation (2.40).

Since the control for common electric drives is generally implemented on the stator side of the machine, one state variable is the stator current  $\mathbf{i}_s^s$ . In fact, the control loop can instead involve rotor currents in particular application such as the the control of a Doubly-Fed Induction Generator (DFIG).

Moreover, in most of the applications, the rotor circuit is not accessible in the case of an IM since it is not externally supplied. For this reason, the measurements of the the rotor currents are not easily available. The rotor flux

$\psi_R^s$  is chosen as the second state variable, following the equation:

$$\mathbf{i}_R^s = \mathbf{i}_M^s - \mathbf{i}_s^s = \frac{\psi_R^s}{L_M} - \mathbf{i}_s^s \quad (2.41)$$

Substituting Equation (2.41) in Equation (2.40), Equation (2.42) is found.

$$\begin{aligned} L_\sigma \frac{d\mathbf{i}_s^s}{dt} &= \mathbf{v}_s^s - R_s \mathbf{i}_s^s - \underbrace{\frac{d\psi_R^s}{dt}}_{\mathbf{E}^s} \\ \frac{d\psi_R^s}{dt} &= R_R \mathbf{i}_s^s - \left( \frac{R_R}{L_M} - j\omega_r \right) \psi_R^s \end{aligned} \quad (2.42)$$

In conclusion:

$$L_\sigma \frac{d\mathbf{i}_s^s}{dt} = \mathbf{v}_s^s - (R_s + R_R) \mathbf{i}_s^s - \left( j\omega_r - \frac{R_R}{L_M} \right) \psi_R^s \quad (2.43)$$

Subsequently, Equation (2.42) is transformed into the dq0 synchronous reference frame by rotating the  $\alpha_s \beta_s 0_s$  reference frame at the synchronization angle  $\theta_e$ .

$$L_\sigma \frac{d\mathbf{i}_s^{dq0}}{dt} = \mathbf{v}_s^{dq0} - (R_s + j\omega_e L_\sigma) \mathbf{i}_s^{dq0} - j\omega_e \psi_R^{dq0} - \frac{d\psi_R^{dq0}}{dt} \quad (2.44)$$

$$\frac{d\psi_R^{dq0}}{dt} = R_R \mathbf{i}_s^{dq0} - \left( \frac{R_R}{L_M} + j\omega_{slip} \right) \psi_R^{dq0} \quad (2.45)$$

where the slip angular speed is  $\omega_{slip} = \omega_e - \omega_r = s\omega_e$  and  $s$  is the slip.

Finally, the dynamic of the **IM** is completed with the electromagnetic torque expression in Equation (2.46).

$$\tau_m = \frac{3n_p}{2K^2} (\psi_{s,d} i_{s,q} - \psi_{s,q} i_{s,d}) \quad (2.46)$$

## 2.3 Magnetic saturation

When the inductance estimation is performed, its behavior in saturation conditions is studied. The theory in this section is used for the DC+AC method. The reference [8] proposes to study the magnetically saturated

machines modelling them as generic inductors, which follows Equation (2.47).

$$v(t) = \frac{d\psi(i(t))}{dt} \quad (2.47)$$

where  $v$ ,  $i$  are the voltage and current in the bipole, and  $\psi(i(t))$  indicates the magnetic flux linkage as function of the current. The instantaneous flux linkage is expressed as function of the instantaneous current by Equation (2.48),

$$\psi(i(t)) = L_a(i(t))i(t) \quad (2.48)$$

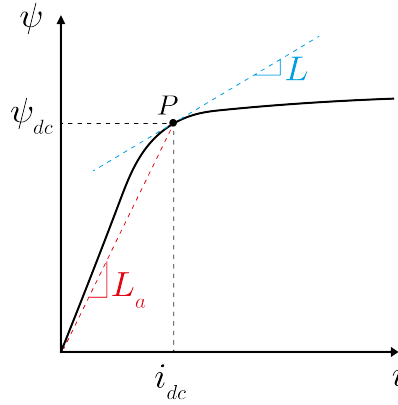
in which the apparent inductance  $L_a$  is function of the current only. Subsequently Equation (2.48) is substituted in Equation (2.47) and the flux derivative is developed.

$$\begin{aligned} v(t) &= \frac{d\psi(i(t))}{dt} = \frac{d(L_a(i(t))i(t))}{dt} = \\ &= \left[ L_a(i(t)) + i(t) \frac{dL_a(i(t))}{di(t)} \right] \frac{di(t)}{dt} = \\ &= [L_a(i(t)) + L_d(i(t))] \frac{di(t)}{dt} = \\ &= L(i) \frac{di(t)}{dt} \end{aligned} \quad (2.49)$$

From Equation (2.49), the instantaneous inductance  $L(i)$  is the sum of two terms, the apparent inductance  $L_a$  and the differential inductance  $L_d = i(t) \frac{dL_a(i(t))}{di(t)}$ , which graphical interpretation is given in Figure 2.8.

$$L(i) = L_a(i) + i(t) \frac{dL_a(i)}{di} \quad (2.50)$$

The instantaneous inductance  $L(i)$  represents the actual inductance around the operating point ( $i_{dc}$ ;  $\psi_{dc}$ ) and it expresses the derivative of the flux linkage to the current in that point.

Figure 2.8: Graphical interpretation of  $L$  and  $L_a$ .

## 2.4 Inverter non-linearity

Self-commissioning involves the utilization of an inverter for the regulation of voltage waveforms injected into an electrical machine. The presence of the inverter introduces a discrepancy between the reference voltage, administered by the controller, and the voltage received at the machine terminal. Non-idealities, as elucidated by Shafiq [2], encompass:

- the threshold voltage of semiconductor switches, enabling the switch to enter the conduction state.
- the on-state resistance of semiconductor switches, indicative of the voltage drop during operation once the switch is in the conduction state.
- the dead-time [9]. A converter leg consists of two semiconductor devices arranged in series. In an ideal switch, the switching moments are defined by the intersection of the control voltage and the carrier waveform. However, real switches have turn-on ( $t_{on}$ ) and turn-off ( $t_{off}$ ) durations, as illustrated in Figure 2.9. Specifically,  $t_f$  is the fall time,  $t_r$  is the rise time. They represent the time employed by the switch to go from a state on ( $90\%V_{ds}$ ) to a state off ( $10\%V_{ds}$ ), and vice versa.  $t_{d,on}$  is the turn-on time and  $t_{d,off}$  is the turn-off time, which corresponds to the time employed by the gate signal to be applied on the drain source.

$$\begin{aligned} t_{on} &= t_{d,on} + t_r \\ t_{off} &= t_{d,off} + t_f \end{aligned} \tag{2.51}$$

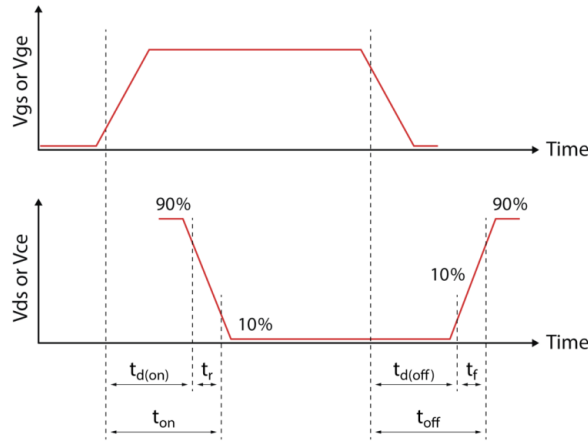


Figure 2.9: Switching delays of a power semiconductor.

To avoid “shoot through” or cross-conduction current through the leg, the dead time  $t_{\Delta}$  is introduced. This is done by delaying the turn-on control input of one transistor to the turn-off control input of the other transistor in the inverter leg, as shown in Figure 2.10. The dead time is conservatively chosen to be greater than the worst-case maximum storage time of the transistors. This dead time introduces an unwanted non-linearity in the converter transfer characteristic.

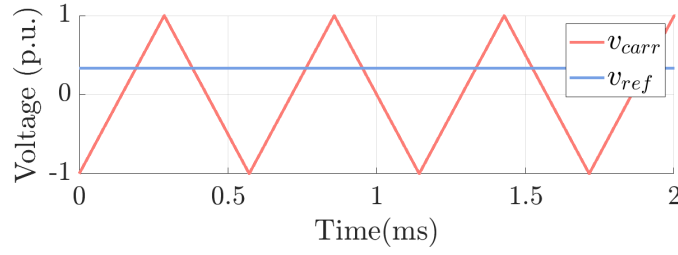
During the dead time, both the switches are off. The inverter output voltage is not controlled by the switching signals but it depends on the direction of the phase current [10]. The difference between the ideal and the actual output voltage is:

$$v_{ph}^{err} = v_{ph}^{ref} - v_{ph}^{actual} \quad (2.52)$$

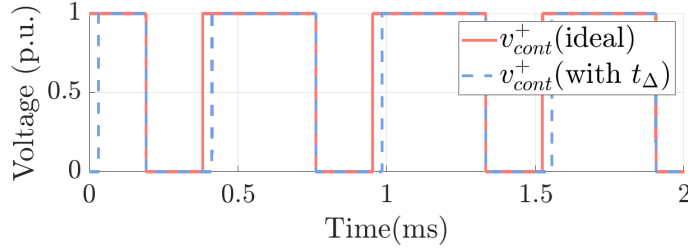
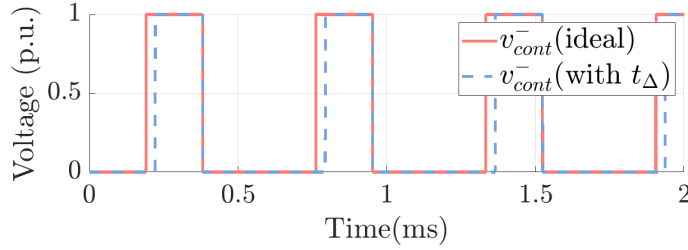
By averaging  $v_{ph}^{err}$  over one time period of the switching frequency in Figure 2.10, the change (defined as a drop if positive) in the output voltage due to  $t_{\Delta}$  is obtained:

$$\Delta V_{ph} = \begin{cases} +\frac{t_{\Delta}}{T_s} V_{DC} & i_{ph} > 0 \\ -\frac{t_{\Delta}}{T_s} V_{DC} & i_{ph} < 0 \end{cases} \quad (2.53)$$

$\Delta V_{ph}$  does not depend on the magnitude of the current but its polarity depends on the direction of the current.



(a) Carrier and reference voltage.

(b) Control voltage of the positive switch of the inverter leg ( $i_{ph} > 0$ ).(c) Control voltage of the negative switch of the inverter leg ( $i_{ph} < 0$ ).Figure 2.10: Effect of blanking time  $t_{\Delta}$ .

The self-commissioning procedure is performed at a standstill. For this reason, it involves very low values of voltage and currents, (for instance around 1% of the rated voltage). With such low voltages, the inverter non-linearity effects influence the estimate of the machine parameters. This problem could be solved by adding voltage sensors at the output of the inverter. On the other side, due to the fourth constraint of the self-commissioning definition given in Section 1.5, the procedure is performed using the available sensors, which are the stator currents sensors and the DC voltage sensor. No further voltage sensors are introduced in the system. Indeed, the measurement of the output voltage of the converter results in a switched waveform, which should be processed to extract its fundamental harmonic. For this reason, the voltage

sensor is not a practical choice in a self-commissioning procedure. The phase voltages can be then reconstructed by knowing the switch command from the output of the controller and the DC voltage, but an accurate compensation of the inverter non-linearity needs to be performed, as explained in Section 3.2.1.

## 2.5 Control strategies

### 2.5.1 Rotor Field Oriented Control (RFOC)

The company Imperix provides the Simulink file for the **RFOC** of an **IM**, explained in the knowledge base section [11].

The system model of the RFOC is shown in Figure 2.11.

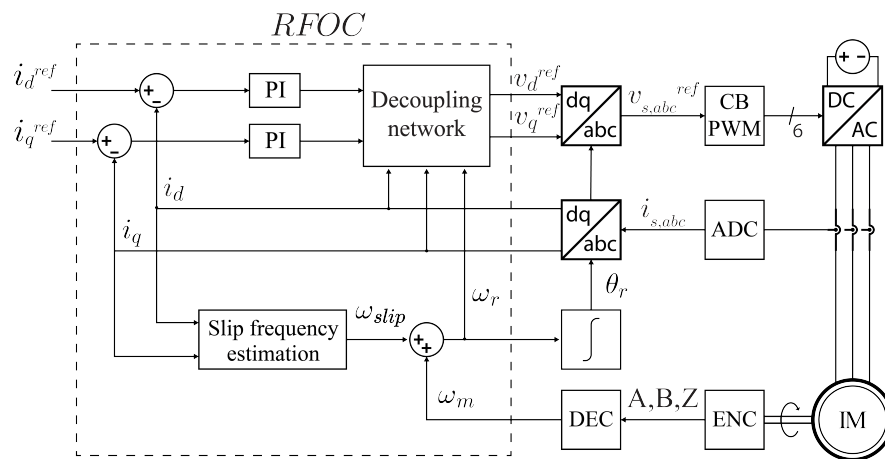


Figure 2.11: Rotor Field-Oriented Control block diagram.

Expressing the Equation (2.45) in components form and assuming perfect field orientation, namely  $\theta = \arg \psi_R$  and  $\boldsymbol{\psi}_R = \psi_R$ , the equations become:

$$\begin{aligned}\frac{d\psi_R}{dt} &= R_R i_{sd} - \frac{R_R}{L_M} \psi_R \\ \omega_{slip} &= \omega_e - \omega_r = \frac{R_R i_{sq}}{\psi_R}.\end{aligned}\tag{2.54}$$

In steady-state,  $i_{sd}$  is called the flux-producing current component and should be controlled such that

$$i_{sd} = \frac{\psi_{\text{ref}}}{L_M} \quad (2.55)$$

In the case of perfect field orientation, the flux had only a d-component and the q-component is zero ( $\psi_R = \psi_R = \psi_{s,d}$ ). Hence, the torque equation in Equation (2.46) is simplified as in Equation (2.56).

$$\tau_m = \frac{3n_p}{2K^2} \psi_R i_{s,q} \quad (2.56)$$

So  $i_{s,q}$  is called the torque-producing current component and it is controlled to have the desired electromagnetic torque  $i_{s,q} = \frac{2K^2 \tau_m^{ref}}{3n_p \psi_R}$ .

To control constant currents in the dq0 reference frame, the **Proportional Integral (PI) Current Controller (CC)** are used.

### 2.5.1.1 Current controller (CC)

In this subsection, the tuning of the **CC** is explained. First, the d and q axes of Equation (2.44) are decoupled by adding the corresponding compensation terms. The rotor flux is assumed constant, so its time derivative is zero,  $\frac{d\psi_R^{dq0}}{dt} = 0$ . As a result, the plant system can be modeled as a resistive-inductive impedance in dq0 reference frame in Equation (2.57).

$$L_\sigma \frac{d\mathbf{i}_s^{dq0}}{dt} = \mathbf{v}_s^{dq0} - R_s \mathbf{i}_s^{dq0} \quad (2.57)$$

The transfer function corresponding to Equation (2.57) is given in Equation (2.58). Because of the isotropic nature of the **IM**, the transfer function is the same in both the d and q axes.

$$H_d(s) = H_q(s) = \frac{I_s(s)}{V_s(s)} = \frac{1/R_s}{1 + sL_\sigma/R_s} = \frac{K_1}{1 + sT_1} \quad (2.58)$$

This type of transfer function in Equation (2.58) allows the use of the magnitude optimum criterion from the reference [12] for the tuning of the **PI CC**. The **CC** parameters are set as follows:

$$\begin{aligned} T_n &= T_1 \\ T_i &= 2K_1 T_d \\ K_p &= T_n/T_i \\ K_i &= 1/T_i \end{aligned} \quad (2.59)$$

where  $T_d$  is the sum of all system delays:

- sensing delay  $T_{d,sense}$ , due to finite sensor and analog chain bandwidth, and possibly filtering delay;



- control delay,  $T_{d,ctrl}$ , due to sampling instant and duty-cycle update instant in the PWM modulator (FPGA peripheral);
- modulator delay,  $T_{d,PWM}$ , average delay between duty-cycle update in the PWM modulator and the resulting change in modulator output;
- switching delay  $T_{d,tran}$ , between change in the modulator output to actual switching of the power device (can often be neglected).

In conclusion, the controller proportional and integral gains ( $K_p, K_i$ ) rely on the estimation of the machine parameter ( $R_s, L_\sigma$ ). These gains affect the performance of the **FOC** technique.



## Chapter 3

# Theory of parameter identification techniques

The purpose of this chapter is to provide a theoretical overview of the parameter identification methodologies. After the literature review in Section 3.1, some of the available solutions between those proposed from the state of the art are implemented first for the **SPMSM** and then for the **IM** in Section 3.2 and in Section 3.3, respectively.

### 3.1 Methodological classification

This section provides essential background information concerning parameter identification methods, highlighting their evolution and the diverse techniques developed over time. Primarily, these methods fall into two main categories: offline identification and online identification. The former involves performing identification with the machine at a standstill, and subsequently analyzing the parameters in post-processing. Conversely, the latter entails estimating parameters during normal machine operation, with updates made routinely.

Given the extensive range of parameter identification methods, various criteria can be employed to classify them. In agreement with [2], the identification procedures can be categorized between standstill methods and techniques allowing shaft rotation. The same author updated this classification in [4], categorizing the main methods into four groups:

- numerical analysis tools, related to **Finite Element Analysis (FEA)**, difficult to develop in an industrial environment where the geometrical design is not available;

- shaft rotation thanks to a prime mover;
- standstill identification (which includes self-commissioning);
- free shaft rotation.

Other potential methods that could be added to this list include:

- algebraic algorithms;
- machine-learning approaches, predominantly for online identification methods ([13] [14]).

Between all these methods the offline self-commissioning procedure is chosen in this project because it is not computationally demanding or mathematically complex, unlike some of the online procedures. Being a commercial product the solution for the parameter identification must be easy to understand and implement, widening the range of addressed customers. Moreover, self-commissioning is feasible for on-site applications because it does not require additional equipment such as a break or prime mover, widening the possible application fields.

Once the type of identification procedure to be investigated in this work is selected, its validation method has to be chosen. Most articles on self-commissioning procedures use as benchmarks either **FEA** simulations ([8], [15], [16]) or the IEEE traditional tests ([17], [18]). In this project, the **FEA** simulations are not used as a benchmark due to the lack of knowledge regarding the machine's geometrical design, so the IEEE standards are chosen.

The traditional tests provide information mainly on the machine at rated working conditions. A drawback of them is the lack of depth in evaluating saturation behavior, which is indeed studied in this project. Saturation behavior can be integrated into control algorithms like **FOC**, potentially enhancing control performance by dynamically adjusting control gains. In this study, the saturation conditions lack of a benchmark since neither **FEA** simulations nor IEEE standard tests can be used for this scope.

### 3.1.1 Literature review of parameter identification methods for SPMSM

In this section, the literature that pertains to the **SPMSM** for offline self-commissioning and standard IEEE 1812-2023 tests [5] is discussed.

The electrical parameters are the focus of this project. However, some references provide the mechanical parameters estimation [19], [20], such as inertia and friction coefficient.

Already existing methods, developed for other machines, are tested on the **SPMSM** because the literature on this machine is not as vast as for others, such as for the **IM** [8] and the **Synchronous Reluctance Machines (SynRM)** [21].

From the circuit used for the **FOC**, the **SPMSM** parameters studied are:

- stator resistance;
- synchronous inductance;
- **PM**-flux.

The methods tested in this work on the **SPMSM** are summarized in Table 3.1 and detailed hereafter.

Table 3.1: Identification techniques for **SPMSM**.

Offline self-commissioning			
Standstill			Shaft Rotation
Parameters	Open loop	Closed loop	
$R_s$	multiple levels voltage DC injection. [8]	<ul style="list-style-type: none"> <li>• one-level DC current injection [2].</li> <li>• two-level DC current injection [2].</li> </ul>	–
$L_s$	–	<ul style="list-style-type: none"> <li>• AC current injection [2].</li> <li>• DC+AC current injection [8].</li> <li>• hysteresis control [21].</li> </ul>	–
$\psi_{PM}$	–	–	I-f <b>Open Loop (OL)</b> startup + sensorless <b>FOC</b> at $i_s^{ref} = 0$ .
IEEE Standard 1812-2023 [5]			
$R_s$	DC measurement.		
$L_s$	Short circuit test.		
$\psi_{PM}$	Open-circuit test.		

### 3.1.1.1 SPMSM stator resistance

The studied references about the stator resistance are classified in Table 3.2.

Table 3.2: Literature overview for **IM** stator resistance offline self-commissioning identification

References	Signal injected	Control configuration	Output	need of <b>Lookup Table (LUT)</b> to estimate $R_s$
[2], [22]	Two-level DC current	with <b>CC</b>	$R_s$ estimate	No
[22]	Multiple-level DC voltage	with <b>CC</b>	<b>LUT</b> for non-linearity compensation	No
[2]	One-level DC current	with <b>CC</b>	$R_s$ estimate	Yes
[23]	One-level DC voltage	<b>OL</b>	$R_s$ estimate	Yes
[23]	Multiple-level DC voltage	<b>OL</b>	<b>LUT</b> for non-linearity compensation	No
[8] (adapted)	Multiple-level DC voltage	<b>OL</b>	$R_s$ estimate and <b>LUT</b> for non-linearity compensation	No
[19]	AC voltage	<b>OL</b>	$R_s$ estimate	Yes

The references in Table 3.2 are subsequently analyzed based on the signal injected in the **SPMSM** circuit.

- AC injection. Stator resistance identification is possible through sinusoidal injection [19]. However, the skin and proximity effects increase the resistance value to its DC value. The DC resistance at a standstill machine is commonly estimated in the literature with an injected signal at zero frequency. Consequently, the AC method is not tested in this project.
- DC injection. The DC test can be conducted in a closed loop configuration injecting one-level (i.e., step) or two-level DC currents [2]. With just one or two-level DC injection only the stator resistance is estimated. For the one-level DC injection and the subsequent **SPMSM** parameter estimation, the inverter non-linearity is usually compensated. So the inverter non-linearity has to be characterized before the self-commissioning starts. If this is done with a separate procedure, the automatic nature of the self-commissioning is affected. Additionally, **CC** tuning is usually performed before starting the self-commissioning procedure. Based on the tuning method, the interaction of the user could be required, which instead should be limited to keep the procedure

automatic. For the sake of comparison, the one-level and two-level DC injection in [2], previously mentioned, are developed respectively in Section 3.2.1.1 and Section 3.2.1.2.

To minimize user interaction and embed the inverter non-linearity estimate in the self-commissioning procedure, further research through the IEEE website is performed.

One-level DC voltage injection in OL configuration is proposed in [23]. While it avoids the tuning of the CC, it still requires prior identification of inverter non-linearity.

The effect of inverter non-linearity can be identified with multiple steps of DC current injected through a CC as in [22], [24], tested on a linear PMSM. However, this method is not entirely automatic because it requires the CC tuning.

The weakness of using a CC and of performing the tracking of inverter non-linearity before self-commissioning are outdated in [8]. Originally tested on the IM, this study extends its application to the SPMSM. It uses an OL procedure with which utilizing the same signal injection, both stator resistance estimation and LUT for inverter non-linearity compensation are achieved. For these reasons, the method in [8], described in Section 3.2.1.3, is implemented in this project.

A benchmark for these procedures is the measured stator resistance defined by the standard IEEE 1812-2023 [5].

### 3.1.1.2 SPMSM synchronous inductance

The analyzed references about the synchronous inductance are classified in Table 3.3.

Table 3.3: Literature overview for **SPMSM** synchronous inductance offline self-commissioning identification

References	Signal injected	Control configuration	Saturation characteristic
[2]	high frequency AC current	with <b>CC</b>	Yes
[25]	rated frequency DC+AC current	with <b>CC</b>	No
[23]	DC+AC voltage	<b>OL</b>	No
[8]	DC+AC voltage	<b>OL</b>	Yes
[21], [26], [27], [28], [29], [30], [31]	square-wave voltage	with hysteresis control	Yes

The research on synchronous inductance aims to identify the saturation characteristic. When examining the inductance of the **SPMSM**, researchers frequently rely on sinusoidal injection [2], [25], [23]. However, variations exist in implementation methods.

[2] proposes a high-frequency (namely higher than the rated value) signal injection in a closed loop configuration, with which the unsaturated value is identified. However, with just one injection level the saturation characteristic cannot be studied. Since this work proposes to analyze the machine in rated and saturated conditions, further research is performed, However, this method is tested in this work for the sake of comparison of the unsaturated inductance in Section 3.2.2.1.

Similarly, [25] utilizes AC voltage injection at rated frequency, yielding only simulation results without considering saturation or non-idealities, making it not interesting for this project where the saturation characteristic is under analysis.

In [23], a DC bias is incorporated into the signal to mitigate inverter non-linearity. However, this adjustment alters the machine's saturation state and cannot be compared to the unsaturated value from the standard tests chosen as a benchmark in this project. Moreover, this reference does not take into account saturation, hence it is not addressed in this work.

To study the saturation characteristic, DC steps are superimposed on the sinusoidal signal [8] in a **OL** configuration. Originally tested on the **IM**, this thesis introduces its extension to the **SPMSM**, by modifying [8] in a closed-loop configuration. The corresponding description is in Section 3.2.2.2.

A weakness of the high-frequency sinusoidal signal injection is its



sensitivity to inverter non-linearity compensation which causes voltage drops not negligible looking at the low voltages involved in the test. To overcome this weakness, the saturation characteristic study through the hysteresis control is approached [21], in which the high voltages improve the robustness of the procedure. This method is popular among the literature [26], [27], [28], [29], [30], and [31]. While all these previous studies have tested this procedure on the **SynRM**, this work proposes its application to the **SPMSM** in Section 3.2.2.3.

A benchmark for the synchronous inductance estimate is the short circuit test from the standard IEEE 1812-2023 [5], which, however, returns only the unsaturated value and not the saturation characteristic.

In conclusion, this work compares [2], [8], [21], and [5] to validate a method for the **SPMSM** saturation characteristic identification.

### 3.1.1.3 SPMSM PM-flux

The last identified parameter for the **SPMSM** is the **PM**-flux. This estimation process typically falls into two main categories: quasi-steady-state [2], [32] and shaft rotation procedures [19], [24].

First, the quasi-steady-state solutions are analyzed. [2] involves controlling the machine speed to zero through a **Speed Controller (SC)** and exploiting its anisotropy under saturation conditions, which is challenging in a mostly isotropic machine like the **SPMSM**. Moreover, the **SC** must be tuned despite mechanical parameters being neither estimated nor calculated. This usually involves user interaction, which in self-commissioning procedures has to be minimal. Hence, this method is not addressed in this work. Another quasi-steady-state solution determines the **PM**-flux linkage based on minimum saliency tracking with minimal rotor movement [32]. However, this procedure has been tested on **PM**-assisted **SynRM** and it relies on the saturation of the **SynRM** bridges, which differs from that of a mostly isotropic machine such as in the **SPMSM**. So this method is not approached in this work.

A viable approach for **PM**-flux identification involves the shaft rotation procedures. Particularly, thanks to the suggestion of Professor I. R. Bojoi, this project proposes to accelerate the **SPMSM** in **OL** up to a certain speed and subsequently transition to sensorless **FOC** with zero current references. Since the machine is accelerated, the self-commissioning constraint of being standstill is not respected. Since this solution offers a reasonable compromise between the self-commissioning method and the implementation time, it is tested in this project and described in Section 3.2.3.1.

Between the shaft rotation procedures, there is the standard open-circuit test [5], chosen as a benchmark for the **PM**-flux estimate and described in Section 3.2.3.2.

### 3.1.2 Literature review of parameter identification methods for IM

This section delves into the literature concerning offline self-commissioning for **IM** and standard IEEE tests 112-2017.

The **IM** parameters, referred to the inverse- $\Gamma$  equivalent circuit used for **FOC** and investigated in this project, include:

- stator resistance;
- leakage inductance;
- rotor resistance referred to the stator side.

The literature review for the magnetizing inductance is addressed in Section 3.1.2.4, the associated methods are not developed in simulation or experiment due to time constraints.

The methods analyzed in this study for the **IM** are summarized in Table 3.4 and detailed hereafter.

Table 3.4: Identification techniques for **IM**.

Offline self-commissioning			
Standstill			Shaft Rotation
Parameters	Open loop	Closed loop	
$R_s$	multiple levels voltage DC injection. [8]	<ul style="list-style-type: none"> <li>• one-level DC current injection [2].</li> <li>• two-level DC current injection [2].</li> </ul>	–
$L_\sigma$	DC+AC voltage injection [8].	–	–
$R_R$	DC+AC voltage injection [8].	–	–
$L_M$	–	–	–
IEEE Standard 112-2017 [3]			
$R_s$	DC measurement.		
$L_\sigma$	Locked rotor test.		
$R_R$	Locked rotor test.		
$L_M$	No-load test.		

### 3.1.2.1 IM stator resistance

As already stated for the **SPMSM** in Section 3.1.1.1, the base principle for estimating the stator resistance consists of letting a direct current flow in the machine winding. While this is common to most of the references in the literature, the implementation is achieved in several ways. The references for the stator resistance estimate are classified in Table 3.5.

Table 3.5: Literature overview for **IM** stator resistance offline self-commissioning identification

References	Signal injected	Control configuration	Output	need of <b>LUT</b> to estimate $R_s$
[33], [2]	One-level DC current	with <b>CC</b>	$R_s$ estimate	Yes
[1], [34], [35], [2], [24], [16]	Two-level DC current	with <b>CC</b>	$R_s$ estimate	No
[8], [10]	Multiple-level DC voltage	<b>OL</b>	$R_s$ estimate and <b>LUT</b> for non-linearity compensation	No

The first solution available from the literature is the closed-loop one-level DC injection [33], [2]. This method requires inverter non-linearity compensation for  $R_s$  estimation. Hence its weaknesses are that both inverter non-linearity identification and **CC** tuning are performed before starting the self-commissioning routine. This usually implies user interaction that in an automatic procedure has to be minimized. For the sake of comparison, this method is analyzed in this project and described in Section 3.2.1.1. However, further research is performed.

A popular solution from the literature address the two-level DC injection in a closed loop configuration [1], [34], [35], [16], [24], [2]. The first improvement compared to the one-level DC injection is that no compensation of inverter non-linearity is needed to estimate  $R_s$ , as explained in detail in Section 3.2.1.2. However, tuning the **CC** has to be performed before starting the identification sequence. Moreover, this procedure estimates just the stator resistance but not the inverter non-linearity, usually employed for the following parameter estimation. A possible solution is to perform the inverter non-linearity identification in sequence to the  $R_s$  estimate [16], [24]. However, these last two references keep the closed loop configuration. Since widely spread in the literature, the two-level DC injection is tested in this project, but further investigation is performed toward an **OL** technique.

The weakness of using a **CC** and of performing the tracking of inverter non-linearity before self-commissioning are outdated in [8]. In this method, the stator resistance is extracted from the characteristic phase voltage-phase current in an **OL** configuration. This allows using the same injected signal to determine both stator resistance and inverter non-linearity tracking.

A benchmark for the chosen self-commissioning procedures is the stator resistance measurement as suggested by the standard IEEE 112-2017 [3].

In conclusion, despite the results presented in [8] being more efficient in terms of time consumption and result assessment, this project incorporates all four methods, namely one-level, two-level, **OL** solution, and measurement. This decision aims to evaluate the impact of both open-loop and closed-loop procedures on resistance estimation, as well as to examine the influence of inverter non-linearity across various injection levels.

### 3.1.2.2 IM leakage inductance

The references about leakage inductance identification are categorized in Table 3.6.

Table 3.6: Literature overview for **IM** leakage inductance offline self-commissioning identification

References	Signal injected	Control configuration	Frequency dependent characteristic	Saturation characteristic
[1], [34], [33], [18], [2]	short voltage impulses	<b>OL</b>	No	No
[2]	current ramp	with <b>CC</b>	No	No
[36]	low and high frequency DC+AC current	with <b>CC</b>	Yes	No
[37]	AC voltage	with <b>CC</b>	Yes	No
[16]	DC+AC current	with <b>CC</b>	No	Yes
[8]	DC+AC voltage	<b>OL</b>	No	Yes

The research on leakage inductance aims to identify the saturation characteristic, by respecting the automatic constraint of the self-commissioning routine.

A widely developed solution in the literature is to inject short voltage impulses in the system [1], [34], [33], [18], [2]. However, this procedure provides only the unsaturated value and not a description of the saturation behavior, which is of interest in this work. This method is hence not implemented in this project and further research is performed.

[36] addresses an identification in a closed loop configuration of the leakage inductance by taking into account the influence of the frequency, not considered in this work. It does not provide insight into the saturation behavior, so it is not of interest for this project.

The influence of the frequency on the leakage inductance is studied in [37] through sine-wave excitations in sequence. However, a solution for the saturation characteristic is not proposed.

[16] follows the same method of two sinusoidal current signals in sequence in [37] but in this case, stepped DC bias is introduced. The self-saturation characteristic is then built. Even though this represents a possible path, this method could be further simplified by considering just one injection frequency and changing the data post-processing.

[15] studies the self and mutual saturation of the leakage inductance. However, the experimental tests are performed by rotating the shaft. Hence, the standstill constraint imposed by the self-commissioning definition is not respected and this procedure is set aside.

[8] uses DC+AC voltage signals in OL, bypassing the need for CC tuning. This method provides insights into the saturation behavior of the leakage inductance. Due to its comprehensive and simple nature, this last method has been selected for implementation in this study and described in Section 3.3.2.1.

A benchmark for the chosen self-commissioning procedure is the locked rotor test, described in Section 3.3.2.2, from the standard IEEE 112-2017 [3], which however provides insight only into the unsaturated leakage inductance and not the saturation characteristic.

### 3.1.2.3 IM rotor resistance

In this study, the focus of the rotor resistance identification is related to its identification around rated working conditions. The analysis of rotor resistance based on frequency or current variations is not the objective of this work because these characteristics are not used to improve control performance in the literature. Instead, an online estimate is preferred to achieve this improvement. The references related to the rotor resistance identification are classified in Table 3.7.

Table 3.7: Literature overview for IM rotor resistance offline self-commissioning identification

References	Signal injected	Control configuration	Frequency dependent characteristic	Current dependent characteristic
[1], [34], [33], [2]	DC step	with CC	No	No
[2]	low-frequency DC+AC current	with CC	No	No
[8], [36]	low-frequency DC+AC voltage	OL	Yes	No
[16]	DC+AC current at two frequencies	with CC	No	Yes
[37]	DC+AC current at two frequencies	with CC	Yes	No
[2]	DC+AC current at two frequencies	with CC	No	No

The self-commissioning procedures for rotor resistance identification involve:

- DC step through a CC. While [34], [33], and [2] present the experimental results, [1] mainly presents the theory. However, the accuracy of this method relies on the tuning of the CC, which is based on parameters that still need to be estimated. This method is hence not implemented in this project.
- two DC-biased sine-wave excitations in sequence with different frequencies identifies the characteristics of the rotor resistance as a function of the DC current [16]. [37] tests this method to identify the rotor resistance characteristic varying the frequency. The frequency-dependent and the current-dependent characteristics contribute to machine knowledge at a standstill but are not in study in this project because not considered for control performance optimization. So this method is set aside.
- Low-frequency AC single-phase injection, implemented in this project and described in Section 3.3.3. The literature proposes different variations of these tests. [2] and [8] introduce a DC bias in the low-frequency AC signal to mitigate inverter non-linearity, in contrast to [18]. Hence, [18] is discarded. On the other side, [8] and [18] favor an

**OL** procedure, differently from [2]. Hence [2] is discarded. [18] present just the simulation results, instead, [2] and [8] validate the method on an experimental setup. So [18] is set aside. The method exposed in [8] is developed in this project because it allows to avoid the need for **CC** tuning, validating the test on an experimental setup. The frequency characteristic is studied also with this signal injection [8], [36], but it is not considered in this work.

A benchmark for the chosen self-commissioning procedures is the locked rotor test from the standard IEEE 112-2017 [3], described in Section 3.3.2.2.

### 3.1.2.4 IM magnetizing inductance

As seen for the leakage inductance in Section 3.1.2.2, the magnetizing characteristic based on the current variations is interesting from a controller point of view and it is an object of study in this project.

The references about the magnetizing inductance are classified in Table 3.8.

Table 3.8: Literature overview for **IM** magnetizing inductance offline self-commissioning identification

References	Signal injected	Control configuration	Frequency dependent characteristic	Saturation characteristic
[1], [2]	Iterative procedure from $\tau_r$	with <b>CC</b>	No	No
[2]	Iterative procedure from $\tau_r$	<b>OL</b>	No	No
[18]	low-frequency DC+AC current	with <b>CC</b>	No	No
[38]	low-frequency DC+AC current	with <b>CC</b>	No	Yes
[39]	AC current	with <b>CC</b>	No	Yes
[17], [16]	voltage ramp	<b>OL</b>	No	Yes
[8]	step down voltage	<b>OL</b>	No	Yes

The analyzed literature for magnetizing inductance identification involve:

- iterative procedures. An iterative procedure is addressed in [1]. However, this method uses the magnetizing current resulting from the no-load test, which has to be performed before the self-commissioning

procedure. Hence, the self-commissioning constraints are violated so this procedure is not suggested as a solution for this work. To overcome this limit, variations of this method are then proposed in [2]. It tests two iterative methods based on both a sinusoidal current as well as a DC current injected through CC. However, all the iterative procedures addressed in [1] and [2] do not track the magnetizing characteristic but only one value is identified. Hence they are excluded and further research is performed.

- voltage ramp injection in OL [17], [16]. However [16] shows that, despite the compensation of inverter non-linearity, this method is sensitive to the voltage error caused by the inverter and the stator resistance estimation. This method does not provide insight into the saturation conditions so it is set aside.
- step down with single-phase OL procedure [8]. This allows tracking the saturation characteristic based on the current amplitude. However, this method requires high accuracy of the voltage measurements to build a good point of comparison for the magnetizing curve. This accuracy is difficult to achieve by recording the measurement from a scope. Hence, it is not suggested for this application due to a lack of adapted equipment for the validation of this method.
- explicit functions [15]. It considers the mutual saturation effect. Traditionally the self-saturation effect is modeled as a function of one variable, instead with mutual saturation two variables are considered. The magnetizing inductance may saturate as a function not only of the stator flux but also as a function of the flux leakage. However, this method allows shaft rotation, so it is not considered as a self-commissioning procedure and hence not suggested for implementation.
- single-phase low-frequency AC test. [18] addresses an OL procedure. Since it is based on simulation, the non-idealities are not considered, such as compensation of voltage error due to inverter and saturation. For this reason, it is not developed in this project.

[39] identify the magnetizing characteristic through a single-phase test with CC without any DC bias, varying just the amplitude of the sinusoidal reference signal. With its simple implementation, this is a suitable procedure to be tested in this application.



However, [38] asserts that the traditional single-phase test gives an error. The inherent error above the rated saturation level comes from the fact that the static magnetizing inductance is alternating in a wide range. A direct numerical integration method is proposed to effectively correct the differential inductance effect. Moreover, this is one of the procedures that allow for building the magnetizing characteristic. This method represents a possible path to investigate. In [38] the DC bias is introduced in the traditional AC injection in single phase configuration to change the saturation state of the machine. The injection current signal is regulated through a CC.

These last two references represent a possible self-commissioning procedure to be tested in simulation and experiment. However, due to time constraints, this is not done in this project.

A benchmark for the chosen self-commissioning procedures is the no-load test from the standard IEEE 112-2017 [3].



## 3.2 Parameter Estimation for SPMSM

In this section, the theoretical explanation of the **SPMSM** parameter identification procedures tested in this project is presented.

### 3.2.1 SPMSM stator resistance

Three different methods are used to estimate the resistive part, classified based on the number of levels (i.e., steps).

1. One-level DC injection in dq0 reference frame proposed in [2].
2. Two-level DC injection in dq0 reference frame proposed in [2].
3. Multiple levels DC voltage injection in abc reference frame proposed in [8] and adapted in this work to the **SPMSM**.

The following considerations are made:

- The estimated resistance ( $R_s$ ) is not only the resistance of the machine phase, but it also includes the resistance of the entire system, which comprises the machine, cables, and inverter.
- The DC injection is suitable for resistance estimation because the derivative of the constant current during the time is zero, so there is no voltage drop on the inductors and the terminal voltage is equal to the resistive drop.
- The test is at a standstill. As a consequence the rotor speed  $\omega_r$ , and so the back-**EMF**, are zero.
- To prevent the generation of torque, a constant current is injected solely in the d-axis ( $i_{s,d}$ ), while the q-axis current remains at zero. Additionally, the voltage of the equivalent circuit terminal in Figure 3.1 represents the reference voltage in the d-axis ( $v_{s,d}$ ), the output of the controller.

Under these conditions, the equivalent circuit in the d-axis is drawn in Figure 3.1.

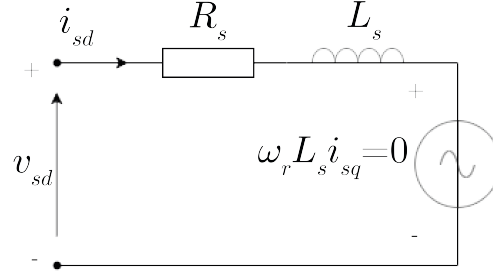


Figure 3.1: Equivalent circuit of the entire system under test in the d-axis for one-level and two-level DC injection.

### 3.2.1.1 One-level DC injection

In the first method [2], the rated current of the machine is injected in the d-axis in Figure 3.2 (a). The voltage output of the **CC** is recorded as in the simulation in Figure 3.2 (b). The steady-state behavior of the machine is then evaluated.

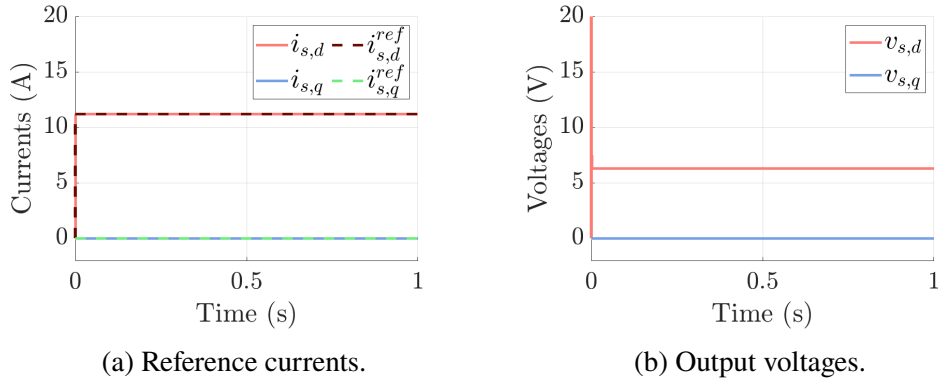


Figure 3.2: Simulation of one-level DC injection with **CC**, step at 0 s from zero Ampere to the rated value  $I_{sn}$ , ideal case, with no dead time simulation, and so, no compensation.

The voltage equation can be derived from Figure 3.1 to calculate the stator resistance  $R_s$ :

$$v_{s,d} = R_s i_{s,d} \Rightarrow R_s = \frac{v_{s,d}}{i_{s,d}} \quad (3.1)$$

For this reason, the nameplate data of the machine has to be known before performing this procedure. Moreover, the current is applied through a **CC**, which needs to be tuned a priori. It can be tuned manually or, if the parameters are available from the datasheet, with the magnitude optimum criterion, as in

this case. On the other side, accurate parameters of the machine are still not available, which can result in a long settling time for the controlled current. For this reason, the time window in which the current step is performed needs to be long enough to allow the current to stabilize. On the other side, if the step lasts too long, for example, more than two minutes, the machine risks heating up, leading to erroneous estimation. To ensure accurate testing, it is necessary to perform the test with the rotor at ambient temperature since the machine parameters are temperature-dependent. The machine should be at rest for a sufficient amount of time to ensure that its windings are also at ambient temperature. However, it is important to note that this work does not take into account the influence of temperature, as stated in Section 1.5.

In this case, to avoid the influence of the CC, the measured current is considered in the calculation, and not the reference one, so that any difference between the two values does not affect the estimation of the machine parameters.

The test is conducted both with and without the inclusion of dead time to assess its impact.

The voltage at the output terminals of the inverter is lower than the reference voltage due to the internal voltage drop (in the simulation caused by the dead time), as explained in Section 2.4. As a consequence, the current rise is slower than the ideal one (see Figure 3.3 (a)). When dead time is integrated into the system, the output voltage of the CC ( $v_{sd}$  with  $t_{\Delta}$ ) is higher than the voltage drop on just the resistance of the system ( $v_{sd}$  ideal), as depicted in Figure 3.3 (b). The mismatch between the reference voltage and the actual voltage represents a drawback. There are usually no voltage sensors installed at the output of the inverter to measure the actual voltage applied to the stator. For this reason, the output voltage must be estimated from the voltage reference, taking into account the effect of non-linearities, by using the LUT generated with the method in Section 3.2.1.3.

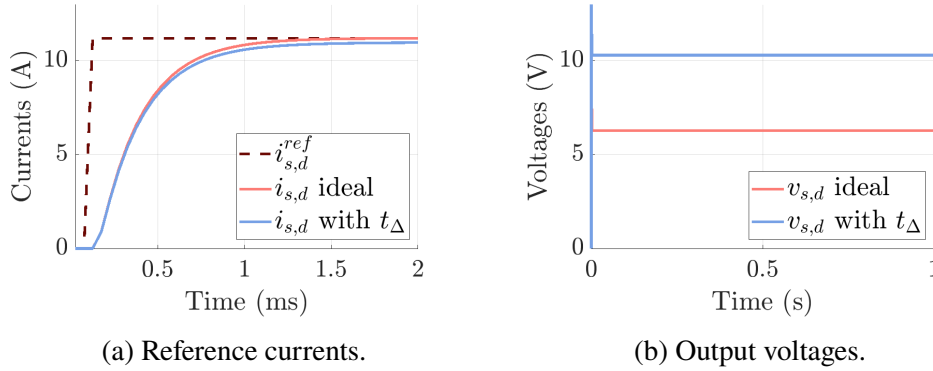


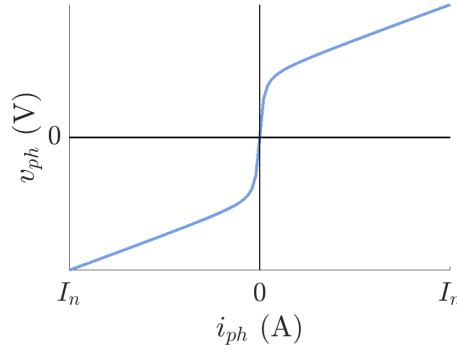
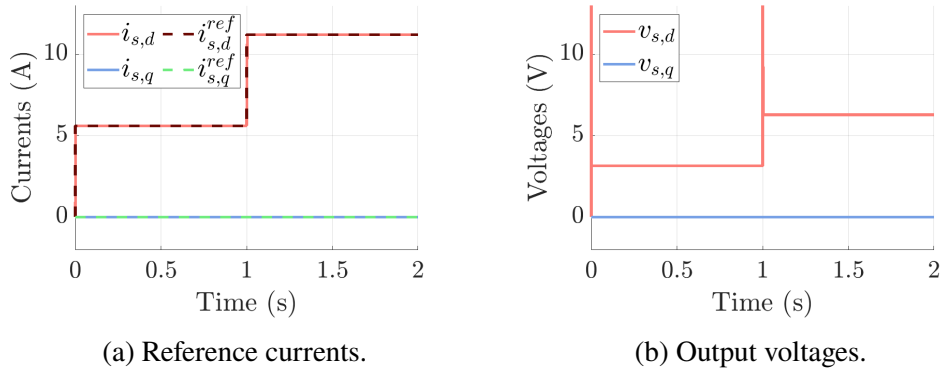
Figure 3.3: Effect of simulated dead time  $t_{\Delta}$  on control performances in the d-axis.

### 3.2.1.2 Two-levels DC injection

The second method [2] uses two levels of direct current in the d-axis. The slope of the characteristic voltage-current of the machine represents the stator resistance in the linear region and is computed with the Equation (3.2).

The **CC** is still used to set the current references, so the considerations regarding it, done for the first case, are still valid. The two-level DC injection method has a drawback in that the selection of set points is random. The choice of the second set point relies on the expert who performs the self-commissioning procedure. The main feature to take in mind is to remain at current levels close to the nominal value to avoid the nonlinear region of the characteristic phase current-phase voltage ( $v_{ph}(i_{ph})$ ) in Figure 3.4. In this work, the first set point  $i_{sd,1}$  is half of the rated current and the second one is the rated current  $i_{sd,2}$ . The simulated signals are shown in Figure 3.5.

$$R_s = \frac{v_{sd,2} - v_{sd,1}}{i_{sd,2} - i_{sd,1}} = \frac{\Delta v_{sd}}{\Delta i_{sd}} \quad (3.2)$$

Figure 3.4: Characteristic  $i_{ph} - v_{ph}$ .Figure 3.5: Two levels DC injection with **CC**, step at 1 s from  $0.5I_{sn}$  to  $I_{sn}$ , ideal case, without  $t_{\Delta}$  simulation.

### 3.2.1.3 Multiple levels DC injection

This last procedure is performed in [8] and it consists of the characterization of the phase voltage-phase current to identify the inverter non-linearities. This is an **OL** method, so no **CC** is used and no tuning of it is done before performing this procedure. A set of reference values of phase voltage is chosen to span the range between zero and the rated phase current of the machine. For this reason, the nameplate data needs to be known as in the previous methods. Per each step of voltage, the phase current is measured, to finally create the map voltage-current of the system under study, similarly as in the example waveform in Figure 3.4.

The maximum phase voltage that can be applied needs to be carefully known to avoid damaging the machine phase. One way is to increase the

voltage by small steps until the measured current reaches the rated value.

Another difference to the previous methods is the reference frame of the equivalent circuit. In fact, for the first two cases the calculations are performed in the dq0 reference frame, in this last procedure the abc reference frame is considered.

The goal of this method is to create a single-phase circuit by applying no voltage in phase c, so the voltage in phase a is going to be equal in the module and opposite in sign to that in phase b. The inverter acts as a full-bridge converter. The advantage is that phase c is virtually open, but the physical configuration does not change. This feature makes the procedure feasible for machines placed already on site. The resulting equivalent electrical configuration is shown in Figure 3.6.

$$\begin{aligned} v_{s,b} &= -v_{s,a}, v_{s,c} = 0 \\ i_{s,b} &= -i_{s,a}, i_{s,c} = 0 \end{aligned} \quad (3.3)$$

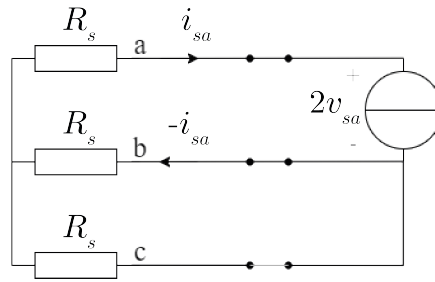


Figure 3.6: Selected single-phase topology for **IM** voltage supply with phase c "virtually" opened.

The other element that has to be carefully chosen is the number of voltage steps. The voltage is stepped very finely when the current approaches zero. the steps are wider at higher values of currents. This allows an accurate characterization of the knee of the curve at low currents (see Figure 3.4). Moreover, as for the previous methods, the duration of a step should be long enough (for instance one second) to allow the current to settle per each set point, removing the inductive component. This is also the reason why current steps are chosen to identify the set points and not a current ramp, where the time derivative of the current is not null. As a consequence, the impedance becomes partly inductive.

To further reduce the noise influence on the resistance estimation, a linear least square is performed on the last five samples, making sure to be far enough



away from the nonlinear area. The slope of the linearization represents the stator resistance.

The voltage error is due to the difference between the reference phase voltage  $v_{s,a}^{ref}$  and the linear component  $R_s I_{s,a}$ , as in Equation (3.4). If the curve of  $v_{err}$  presents some irregularities (for instance due to noise, especially at low currents), a linear least square is performed to maintain the monotonicity.

$$v_{err} = v_{s,a}^{ref} - R_s I_{s,a} \quad (3.4)$$

The  $v_{err}$  data are used to build the **LUT** to compensate for the voltage difference. The **LUT** takes the current as input and it outputs the voltage error  $v_{err}$ . This error is added to the voltage reference  $v_{s,a}$ , output of the current controller. If the phase current is positive the error is added, if the current is negative it is subtracted. The **LUT** corrects the three phases a, b, and c.

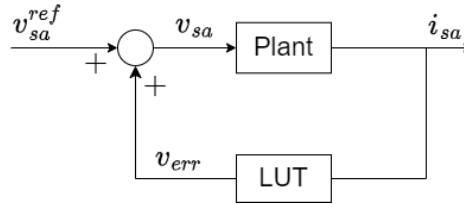


Figure 3.7: Schematic of the inverter non-linearity compensation.

After recording the experimental voltage and current values, the data is averaged within a specified window of observation, in this work arbitrarily one-twentieth of the sampling rate of 20 kHz. In this way, the transient of the voltage step is avoided and just the steady-state behavior is considered. On the other side, the number of samples for the average allows accurate results without requiring big computational efforts from the CPU.

In the final analysis,  $R_s$  is estimated from  $v_{sa}^{ref}$  and the measured current  $i_{sa}$ . Subsequently,  $v_{err}$  is computed to construct the **LUT**. This implies that the **LUT** is not required specifically for  $R_s$  estimation; instead, it proves valuable for other testing purposes.

In this work, the characterization of the inverter is performed before starting the self-commissioning routine. The last presented method is chosen for resistance estimation as it directly extracts resistance from the LUT without applying any further methods.

### 3.2.2 SPMSM synchronous inductance

#### 3.2.2.1 AC method

The high-frequency injection is used to estimate the impedance of the equivalent circuit in the d-axis. The AC method is based on the reference [2]. A sinusoidal current of known magnitude and known frequency is injected in the d-axis, keeping to zero the q-axis current, as in Equation (3.5).

$$\begin{aligned} i_{sd}^{ref} &= I_{sd,ac} \cos(\omega_h t) \\ i_{sq}^{ref} &= 0 \end{aligned} \quad (3.5)$$

In this way, the rotor is kept in a steady state  $\omega_r = 0$ , so the equivalent circuit under study is presented in Figure 3.8. The **Discrete Fourier Transform (DFT)** is used to extract the fundamental voltage and current from the waveform in the d axis ( $\dot{v}_{sd}^{fund}$ ,  $\dot{i}_{sd}^{fund}$ ). According to Kirchhoff's law:

$$\dot{v}_{sd}^{fund} = \dot{Z}_s \dot{i}_{sd}^{fund} \Rightarrow \dot{Z}_s = \frac{\dot{v}_{sd}^{fund}}{\dot{i}_{sd}^{fund}} \quad (3.6)$$

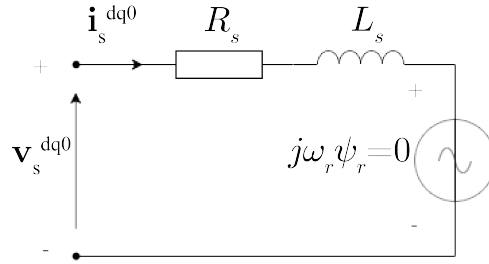


Figure 3.8: Vector equivalent circuit in case of AC injection in dq0 reference frame.

Knowing the circuit impedance  $\dot{Z}_s$  and the phase shift between the voltage and the current  $\theta_h$ , the resistance and the reactance are calculated as projections to the real and imaginary axes. From which the synchronous inductance  $L_s$  is known:

$$\begin{aligned} R_s &= |\dot{Z}_s| \cos \theta_h \\ X_s &= |\dot{Z}_s| \sin \theta_h \Rightarrow L_s = \frac{X_s}{2\pi f_h} \end{aligned} \quad (3.7)$$

A **PI** controller is not able to track a sinusoidal reference. To overcome this

problem, a **Proportional Resonant (PR)** is used instead. The **PR** controller is provided by imperix and it is available in the knowledge base website [40].

Even though this method can estimate both the resistance and the inductance, it is not accurate for the resistance. Skin and proximity effects increase the resistances at high frequency, giving erroneous results for the estimation.

How to choose the injection frequency?

The chosen value should be close to the machine's rated operating. A too-high injection frequency can alter the resistance due to the skin effect of the conductor. This causes a displacement of the test results from the normal operating conditions of the machine. In this work, 300 Hz is arbitrarily chosen.

However, the AC method is only valid in linear work conditions. In case of saturation, linearity is lost and the Thévenin impedance becomes irrelevant due to current distortion. The behavior of the inductance in saturation condition is studied in Section 3.2.2.2.

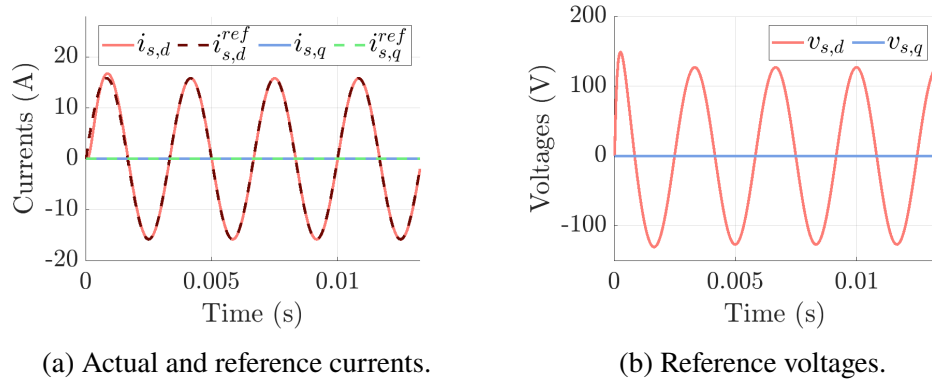


Figure 3.9: Current injection with frequency of 300 Hz in dq0 reference frame, ideal case with no dead time simulation.

### 3.2.2.2 DC+AC method for SPMSM

The DC+AC injection presented in the reference [8] is based on the theory in Section 2.3. This method was developed for **IM**, but it can be adapted to synchronous machines. Some differences are applied, for instance, for the **IM** the method is **OL**: voltage references are injected and currents are measured. Control is not explicitly applied over the flux vector orientation in synchronous machines operated in **OL**. For this reason, the current is controlled in a closed loop with a **PR** controller. Hence, the DC+AC signal is applied in the dq0 reference frame, as in Equation (3.8).

It consists of a small sinusoidal current ( $i_{sd,ac}(t)$ ) superimposed to a predefined set of increasing DC levels ( $i_{sd,dc}$ ) in the d-axis. The q-axis current is kept to zero to avoid torque production and maintain stationary conditions.

$$\begin{aligned} i_{sd}^{ref} &= i_{sd,dc} + i_{sd,ac}(t) = i_{sd,dc} + I_{sd,ac} \cos(\omega_h t) \\ i_{sq}^{ref} &= 0 \end{aligned} \quad (3.8)$$

The DC component is chosen to cover the entire current range based on prior knowledge of  $R_s$ , and it establishes the operating point (marked as P in Figure 2.8). The AC signal's low amplitude nature allows for using small-signal theory, assuming linearity around the operating point P. AC voltages and currents are utilized to determine the instantaneous inductance  $L_s(i)$ . The amplitude ( $I_{sd,ac}$ ) and frequency ( $f_h$ ) of the current are predetermined and known, while the voltage is obtained from the output of the CC. Moreover, the inverter non-linearity is compensated through the LUT from Section 3.2.1.3, such that the actual phase voltage can be estimated from the reference voltage from the CC. The DFT is used to extract the fundamentals of voltage and current, so the synchronous inductance  $L_s$  is calculated as in Equation (3.7).

### 3.2.2.3 Hysteresis control

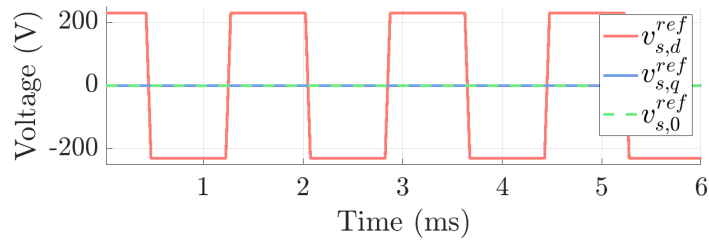
The DC+AC method in Section 3.2.2.2 is very sensitive to phase shift error caused by time delays introduced by the Pulse Width Modulation (PWM) and the experimental setup. Furthermore, a good compensation of the inverter non-linearity has to be achieved due to the low voltages. This section aims to analyze a more robust method for estimating the saturation characteristic of SPMSM using hysteresis control. The corresponding reference is N. Bedetti [21].

From Equation (2.13), if the saturation is considered in the model, the inductance is a function of the current and so it is considered inside the flux. The equations are

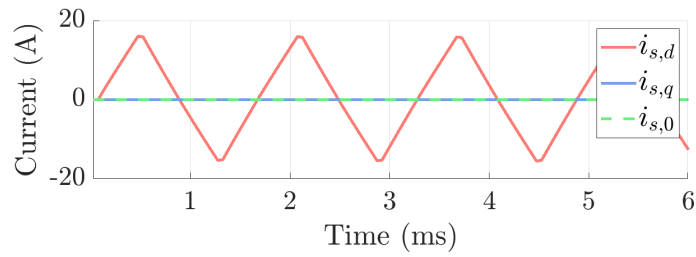
$$\begin{aligned} v_{sd} &= R_s i_{sd} + \frac{d\psi_{sd}}{dt} - \omega_e \psi_{sq} \\ v_{sq} &= R_s i_{sq} + \frac{d\psi_{sq}}{dt} + \omega_e \psi_{sd} \end{aligned} \quad (3.9)$$

The square wave reference voltage is applied on the d-axis, keeping to zero the voltage in the q-axis, following Equation (3.10) (see Figure 3.11 (a)). Zero q-current results in no torque production and stand-still condition of the machine ( $\omega_e = 0$ ).

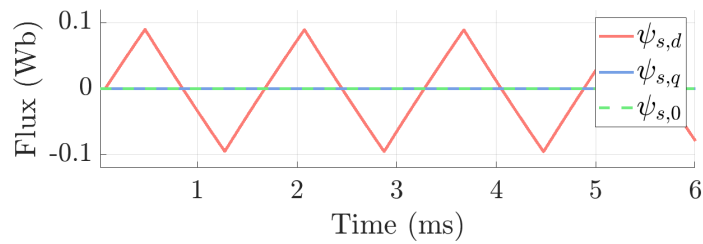




(a) Voltage.



(b) Current.



(c) Flux.

Figure 3.11: Hysteresis control simulation waveforms in dq0 reference frame.

From Figure 3.12, the flux and the current are zero at the same moment. A possible problem that can be experienced is not seeing the flux null at the same moment as the current. This offset is a consequence of the drift of the flux integrator. This drift changes with the initial condition in the integrator. The effect of the integrator offset is to translate the saturation characteristic on the y-axis, but the slope of the curve is not affected by this.

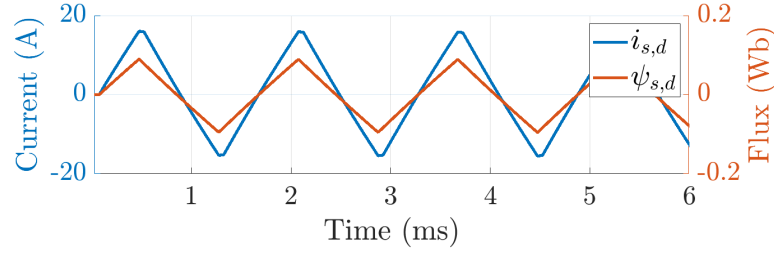


Figure 3.12: Current and flux in the d-axis in hysteresis control simulation.

The reference [21] uses **Multiple Linear Regression (MLR)** for the data post-processing to reduce the computational weight of the algorithm. The method is based on the identification of the slopes of two areas, saturation and linear region. However, **MLR** applied on the saturation characteristic not as curved as in a **SynRM** does not provide satisfying results because it is not able to track the small variation of the inductance. On the other side, the definition of the inductance in Equation (3.12) can not be used because once the current goes towards zero,  $L_s$  diverges to infinity.

$$L_s = \frac{\psi_{sd}}{i_{sd}} \quad (3.12)$$

For this reason, the discrete derivative in Equation (3.13) has been chosen to identify the slope of the saturation characteristic.

$$L_s = \frac{\psi_{sd}(k) - \psi_{sd}(k-1)}{i_{sd}(k) - i_{sd}(k-1)} = \frac{\Delta\psi_{sd}}{\Delta i_{sd}} \quad (3.13)$$

#### 3.2.2.4 Short-circuit test

The short-circuit test is proposed by the standard IEEE 1812-2023 [5]. It is not a self-commissioning procedure but it is used to find a benchmark for the **SPMSM** synchronous inductance  $L_s$ .

In the short-circuit test, the **SPMSM** is driven to a desired speed with the help of a prime mover (in this case, the **IM**), while short-circuiting its phases. The steady-state Equation (2.15) are modified by imposing  $\mathbf{v}_s^{dq0} = 0$ , because of the short circuit. The steady-state short circuit equations are given in Equation (3.14).

$$\begin{aligned} 0 &= R_s i_{s,d} - \omega_e L_s i_{s,q} \\ 0 &= R_s i_{s,q} + \omega_e (L_s i_{s,d} + \psi_r) \end{aligned} \quad (3.14)$$

If the resistance  $R_s$  is negligible or if the rotational frequency is high, the short-circuit equations can be simplified as in Equation (3.15).

$$\begin{aligned} 0 &= \omega_e L_s \dot{i}_{s,q} \\ 0 &= \omega_e (L_s \dot{i}_{s,d} + \psi_r) \end{aligned} \quad (3.15)$$

In conclusion, the current is null in the q-axis  $\dot{i}_{s,q} = 0$ , and the short-circuit current  $I_{sc}$  is just in the d-axis.

$$I_{sc} = \frac{V_{oc}}{\sqrt{3}X_s} \quad (3.16)$$

where the synchronous reactance at rated speed is  $X_s = \omega_s L_s$ .  $V_{oc} = \sqrt{3}\omega_s \psi_r$  is the line-to-line open circuit voltage.

The rotor excitation in a **SPMSM** is fixed due to the **PM**. As a consequence, the short circuit current cannot be controlled or varied as in a wound-field synchronous machine. For this reason, the steady-state short circuit current is expected to be higher than the rated current of the **SPMSM**. This leads to heating of the machine with risk of **PM** demagnetization and damages of electrical insulation.

A prior analysis is performed to ensure safe operating conditions, avoiding damage to the **SPMSM**. The short-circuit current is calculated with the Equation (3.16). If the  $I_{sc}$  exceeds the maximum allowable value for the **SPMSM**, the current can be limited by adding an external impedance  $\dot{Z}_{ext}$ .  $\dot{Z}_{ext}$  is reactive to avoid increasing the  $I_{sc}$ . The new short circuit current can be estimated by

$$I_{sc} = \frac{V_{oc}}{\sqrt{3} \left( |jX_s + \dot{Z}_{ext}| \right)} \quad (3.17)$$

Furthermore, the **IM** should be able to supply the necessary short-circuit torque to the **SPMSM**. If yes, the short circuit is applied before starting the test. If not, the short circuit is applied after the **SPMSM** reaches the desired speed through an open-circuit test, which is described in Section 3.2.3.2. However, in this case, the current may significantly exceed the rated value, even up to five times higher than the rated value, which poses a high risk of damage to the **SPMSM**. [7].

The test configuration in Figure 3.13 shows how the measurements are performed. Three differential current probes measure the line-to-line voltage of the **SPMSM** and three current sensors are used to measure the phase currents. The short circuit is applied before the test begins. Knowing voltages,



currents, and speed, the synchronous inductance is estimated:

$$L_s = \frac{V_{oc}}{\sqrt{3}\omega_e I_{sc}} \quad (3.18)$$

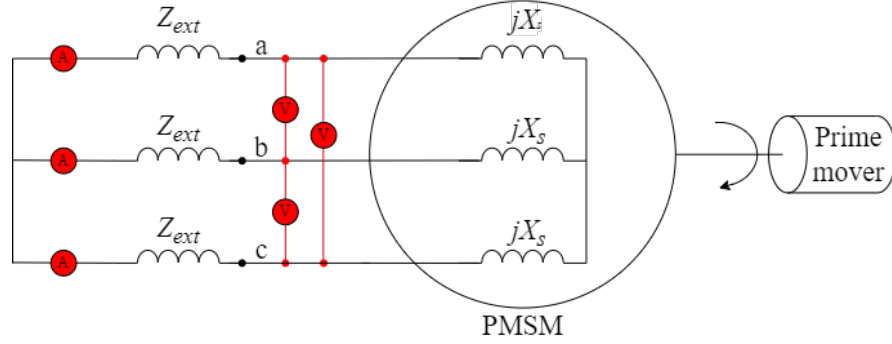


Figure 3.13: Short-circuit test configuration [5].

### 3.2.3 SPMSM PM-flux

#### 3.2.3.1 I-f startup + sensorless FOC

The **PM**-flux  $\psi_R$  is estimated using the voltage equation in the q-axis in Equation (2.13), where it is related to the electrical rotor speed  $\omega_r$ . To create a voltage drop in the q-axis due to the presence of the **PM**, the rotor speed has to be different from zero. For this reason, the constraint of a standstill procedure imposed by the self-commissioning definition cannot be respected. On the other side, the drawback of accelerating the machine at high speed is the temperature increment that can lead to a distortion in the **PM**-flux estimation since the magnetization of the **PM** is temperature dependent.

The I-f start-up procedure is then chosen to accelerate the machine. Once a constant speed is reached, a sensorless control is applied and the current is set to zero with a **CC**. The block diagram for the control method is presented in Figure 3.14. This method was already developed by imperix and it is available on its online knowledge base [41].

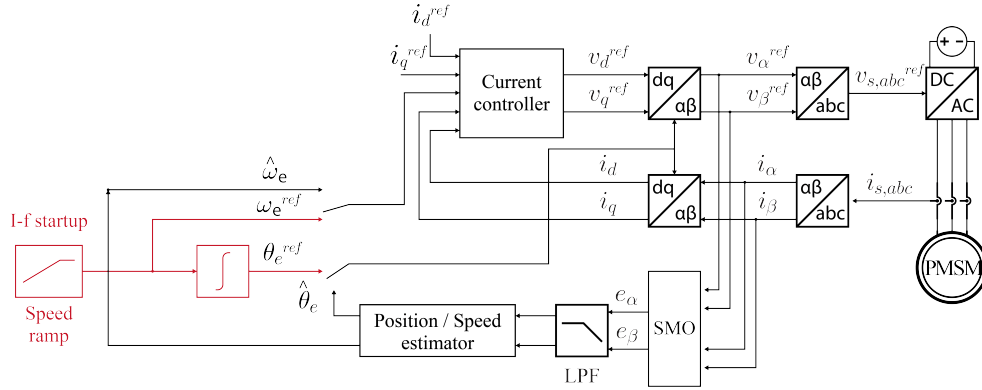


Figure 3.14: Block diagram of an **Sliding-Mode Observer (SMO)**-based sensorless **FOC** with I-f startup for a **PMSM**.

The i-f start-up is an **OL** procedure based on a virtual reference rotating frame. A speed ramp is set as a reference and integrated to find the position of the virtual reference frame.

$$\begin{aligned}\omega_m^{ref} &= \frac{d\omega_m^{ref}}{dt} \cdot t \\ \theta_e^{ref} &= \int_0^t \omega_e^{ref} dt = n_p \int_0^t \omega_m^{ref} dt\end{aligned}\quad (3.19)$$

The reference current  $i_{sq}^{ref}$  in the q-axis is set around the rated value, to provide enough power for the acceleration of the machine. Once the virtual  $\omega_m^{ref}$  is higher than a minimum speed, the reference speed is kept constant, and  $i_{sq}^{ref}$  starts decreasing. The simulated waveforms are shown in Figure 3.16.

How this minimum speed is selected?

The sensorless **FOC** is based on the knowledge of machine parameters to perform the field alignment. Since the parameters are not accurately known before the commissioning procedure, the inaccurate field alignment can result in poor performance of the speed control. At low speeds, this method is more sensitive to motor parameters. Moreover, at low currents, the measurements are not accurate enough to estimate the back-**EMF** and extract the position. To reduce the parameter sensitivity, the minimum constant speed is set "high enough", as a rule of thumb between 1/3 and 1/2 of the nominal speed.

The second step is to align the virtual reference frame with the real dq0 reference frame. This is achieved by canceling the error between their respective speeds. The error alignment  $\theta_{err}$  and its variation are defined in

Equation (3.20), respectively.

$$\begin{aligned}\theta_{err} &= \theta_e - \theta_e^{ref} \\ \frac{d\theta_{err}^{ref}}{dt} &= \omega_e - \omega_e^{ref}\end{aligned}\quad (3.20)$$

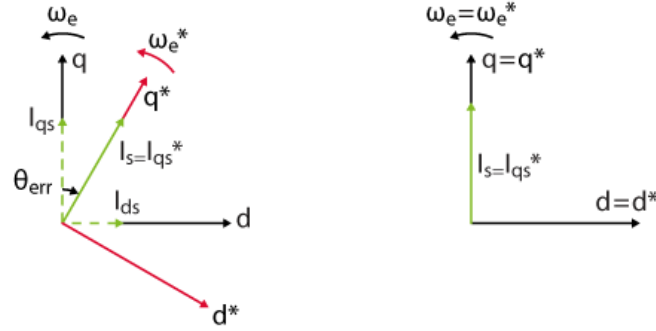


Figure 3.15: (left) rotational frame and current reference from the I-f method (right) rotational frame and current reference from the sensorless FOC.

Once that  $\theta_{err}$  and  $i_{sq}^{ref}$  are within a desired tolerance, the control is switched to a sensorless **FOC** with the current references set to zero. If no current flow in the dq0 equivalent circuit, there is no voltage drop on the impedance of the machine and Equation (2.13) become:

$$\begin{aligned}v_{s,d} &= 0 \\ v_{s,q} &= \omega_e \psi_r\end{aligned}\quad (3.21)$$

Finally, the **PM**-flux is calculated from Equation (3.21).

$$\psi_r = \frac{v_{s,q}}{\omega_e}\quad (3.22)$$

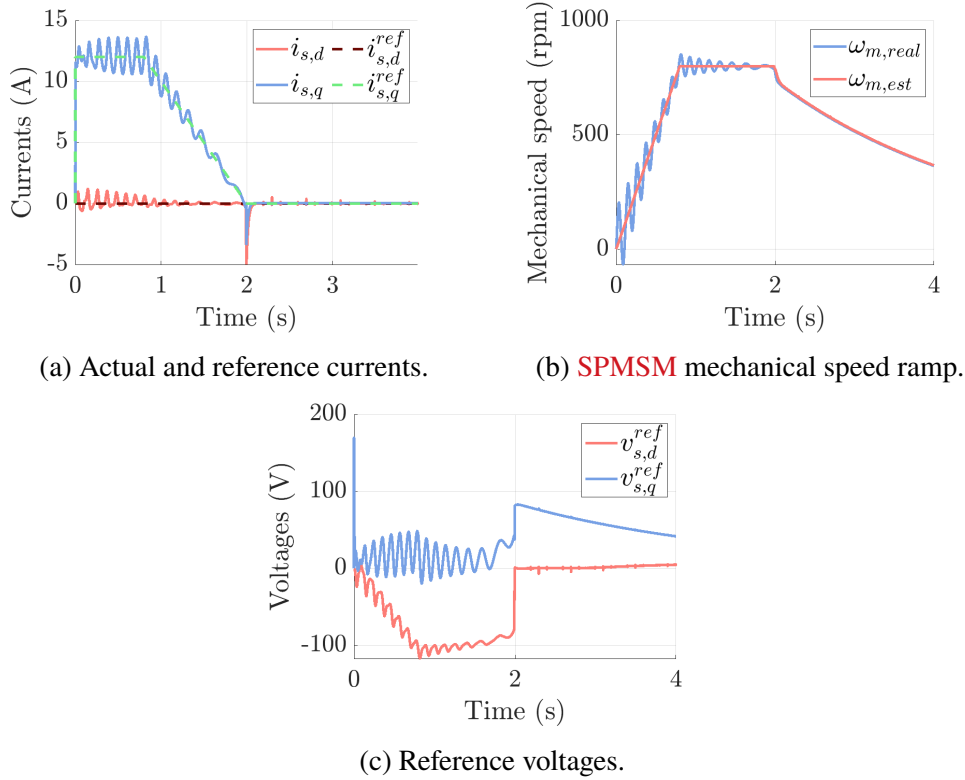


Figure 3.16: Simulated I-f startup from  $t = 0$ s and sensorless FOC at null references in dq0 reference frame introduced at  $t = 2$ s.

### 3.2.3.2 Open-circuit test

The second method is to accelerate the SPMSM up to a constant speed thanks to a prime mover (in this work the IM), as in Figure 3.17 (a). The reference speed is arbitrarily chosen following the same considerations as in Section 3.2.3.1. The SPMSM is in an open circuit so the currents  $i_s^{dq0}$  are null and the Equation (3.21) is valid. The voltage measured at the phase of the SPMSM represents the induced voltage due to the PM, which simulated waveforms are in Figure 3.17 (b). Once the machine reaches steady-state conditions, the PM-flux is estimated from Equation (3.21).

$$\psi_r = \frac{v_{sq}}{\omega_e} \quad (3.23)$$

The line-to-line voltage is measured since the neutral of the SPMSM is not user accessible. Three differential voltage probes are placed as shown in the schematic in Figure 3.17. The speed is known by derivating the measured

position from the resolver described in Section 4.2.3. Figure 3.18 represent the simulated mechanical **IM** speed and the **SPMSM** voltages.

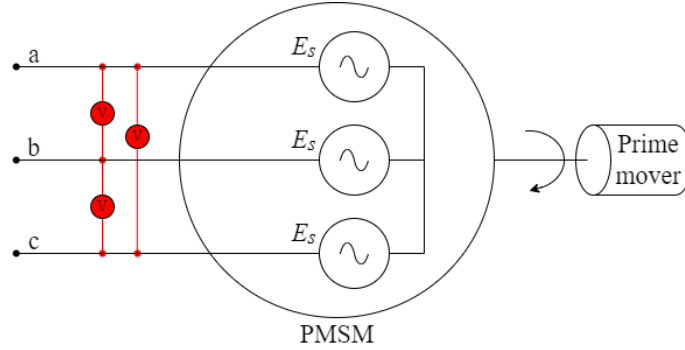


Figure 3.17: Open circuit electrical configuration.

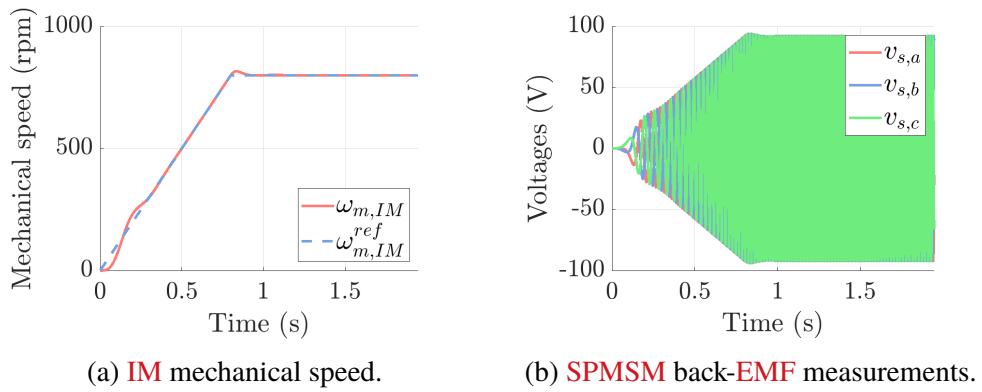


Figure 3.18: Simulation of the open-circuit test.

### 3.3 Parameter Estimation for IM

In all the **IM** self-commissioning procedures the single-phase configuration, represented in Figure 3.6 and described in Section 3.2.1.3, is used.

#### 3.3.1 IM stator resistance

The stator resistance is estimated with the same method used for the **SPMSM** through the DC injection in section Section 3.2.1. The theory is the same, the only difference is the equivalent circuit in which the voltage signals are

injected. Because the electrical frequency  $\omega_e$  is null due to DC injection, the inductances are short-circuited. Specifically, the magnetizing inductance is short-circuited, so no current flow in the rotor branch. The only element in the equivalent circuit that causes a voltage drop is the stator resistance  $R_s$ .

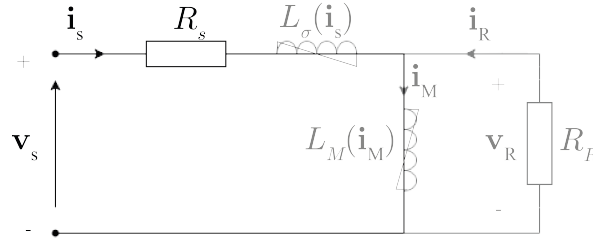


Figure 3.19: Electrical vector configuration in the abc three-phase reference frame in case of DC injection at stand-still ( $\omega_r = 0$ ).

### 3.3.2 IM leakage inductance

#### 3.3.2.1 DC+AC method for IM

Figure 2.7 is the dynamic IM inverse- $\Gamma$  equivalent circuit in case of linear conditions. If the stator teeth and yoke of the machine saturate, the current becomes a nonlinear function of the stator flux. If the iron saturation is considered and at a standstill, Equation (2.40) in the three-phase reference frame becomes:

$$\begin{cases} v_s = R_s i_s + L_\sigma(i_s) \frac{di_s}{dt} + L_M(i_M) \frac{di_M}{dt} \\ 0 = R_R i_R + L_M(i_M) \frac{di_M}{dt} \end{cases} \quad (3.24)$$

The saturation can be modeled by splitting its effect into two inductors: the leakage inductance  $L_\sigma(i_s)$  and the magnetizing inductance  $L_M(i_M)$ . At standstill, the rotor angular speed  $\omega_r$  is zero, by adding saturation, the circuit in Figure 2.7 becomes as in Figure 3.20.

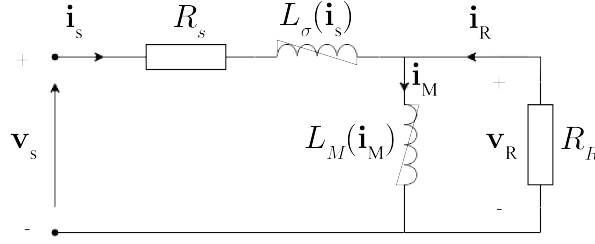


Figure 3.20: Inverse- $\Gamma$  vector equivalent circuit including stator iron saturation in abc reference frame, at standstill ( $\omega_r = 0$ ).

At steady state, the Thévenin equivalent impedance of the circuit in Figure 3.20 is:

$$Z(j\omega_h) = R_s + j\omega_h L_\sigma + \frac{j\omega_h L_M R_R}{j\omega_h L_M + R_R} \quad (3.25)$$

where  $\omega_h = 2\pi f_h$ , with  $f_h$  frequency of the injected signal. The last term of Equation (3.25) converges to  $R_R$  for sufficiently high values of frequency [42]. Subsequently, the approximation of the Thévenin equivalent impedance in Equation (3.25) is given in Equation (3.26).

$$Z(j\omega_h) \approx R_s + R_R + j\omega_h L_\sigma \quad (3.26)$$

As for the **SPMSM**, the DC+AC method explained in Section 3.2.2.2 is employed to estimate the instantaneous inductance. All the considerations already done in Section 3.2.2.2 are valid. The difference is the reference frame in which the procedure is performed. The single-phase configuration in Figure 3.6 is considered. Since it is an **OL** method, the injected signal in Equation (3.27) is the sum of a small sinusoidal voltage with a predefined set of increasing DC voltage levels while measuring the phase currents at each stage.

$$v_{sa}(t) = v_{sa,dc} + v_{sa,ac}(t) = v_{sa,dc} + V_{sa,ac} \cos(\omega_h t) \quad (3.27)$$

Applying the **DFT** on the reference phase voltage  $v_{sa}$  and phase current  $i_{sa}$ , measured from the current sensor in the PEB 8038, the fundamental component is extracted. Knowing the Thévenin impedance with Equation (3.28), the instantaneous leakage inductance is calculated using Equation (3.29).

$$v_{sa}^{fund} = \dot{Z}(j\omega_h) i_{sa}^{fund} \Rightarrow \dot{Z}(j\omega_h) = \frac{v_{sa}^{fund}}{i_{sa}^{fund}} \quad (3.28)$$

$$X_\sigma = |\dot{Z}(j\omega_h)| \sin \theta_h \Rightarrow L_\sigma = \frac{X_\sigma}{2\pi f_h} \quad (3.29)$$

The leakage inductance is calculated per each set point defined by the direct current so that the characteristic curve  $L_\sigma(i_{sa})$ . Notice that the injected voltage in the system is corrected by applying the compensation to the reference voltage with the apposite lookup table to overcome inverter non-linearity.

As for the **SPMSM** in Section 3.2.2.1, the high-frequency test is not indicated for the resistance estimation. The rotor resistance  $R_R$  can be extracted from the real part of the Thévenin impedance  $\dot{Z}(j\omega_h)$ , by subtracting the stator resistance  $R_s$ . However, the high frequency can result in increasing resistance due to the skin effect and proximity effect.

### 3.3.2.2 Locked rotor test

The locked rotor test is performed by following the standard IEEE 112-2017 [3]. It is used to estimate the leakage impedance and the rotor resistance of the **IM**. This test is not a self-commissioning procedure, but it represents a benchmark for the self-commissioning method explained in Section 3.3.2.1.

The rotor of the **IM** is locked by a mechanical mean. It contrasts with self-commissioning techniques that ensure the standstill condition through control. The phase voltage at the rated frequency is increased until the phase currents reach the rated load value. This allows to have the same saturation condition as normal operation. In locked rotor condition the phase voltage is below its rated value. Special care should be taken when increasing the voltage as there is a risk of damaging the machine due to the low value of the machine impedance resulting in high currents and so overheating. Once the steady-state condition is reached, the measurements of the phase voltages are taken with three differential voltage probes. The current is measured with a current probe directly at the **IM** phases. In the post process, the **DFT** is applied to the current and voltage waveform, finding the real and imaginary part of the impedance.

$$v_s^{fund} = Z(j\omega_e) i_s^{fund} \Rightarrow Z(j\omega_e) = \frac{v_s^{fund}}{i_s^{fund}} \quad (3.30)$$

$$Z(j\omega_e) \approx R_s + R_R + j\omega_e L_\sigma \quad (3.31)$$

The magnetizing inductance  $L_M$  is neglected because it is much higher than leakage phase inductance  $L_\sigma$ . As a consequence, it can be assumed that there is no current floating to  $L_M$  parallel branch. The vector electrical configuration of the locked rotor test is given in Figure 3.21.



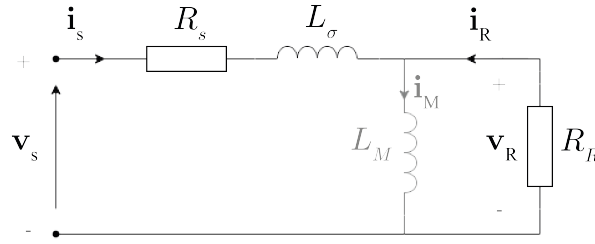


Figure 3.21: Vector electrical equivalent circuit for locked rotor test in the three-phase reference frame.

The reactive impedance is directly related to the leakage inductance  $L_\sigma$ , as shown in Equation (3.31). Instead, the resistive impedance represents the rotor and stator resistance  $R_R + R_s$ .

$$\begin{aligned} R_s + R_R &= |Z(j\omega_e)| \cos \theta_e \Rightarrow R_R = |Z(j\omega_e)| \cos \theta_e - R_s \\ X_\sigma &= |Z(j\omega_e)| \sin \theta_e \Rightarrow L_\sigma = \frac{X_\sigma}{2\pi f_e} \end{aligned} \quad (3.32)$$

The stator resistance is already known from the DC test described in Section 3.2.1.

### 3.3.3 IM rotor resistance

In this section, the method by L. Peretti in [8] for the rotor resistance estimation is studied. The rotor resistance is calculated by knowing the voltage drop over it and the corresponding rotor current. First, the current is found. A single-phase OL voltage at low frequency  $f_l$  is injected into the IM circuit. The configuration is the same already used for the multiple DC injection shown in Figure 3.6. Since it is a single-phase injection, just phase a is considered, with its corresponding equivalent circuit. A single-phase injection does not create a rotating magnetic field, so the machine is not rotating, the rotor angular speed ( $\omega_r$ ) is null and the slip is one.

The injected voltage is

$$v_{sa} = V_{sa,dc} + V_{sa,ac} \cos(\omega_l t) \quad (3.33)$$

Under normal working conditions, the frequency of the injected signal is below its rated slip value. Furthermore, at low frequencies, the skin effect of rotor bars is limited. For these reasons, the frequency is arbitrarily chosen to

be 5% of the nominal slip  $f_{slip} = f_e - f_r$ .

$$f_l = 0.05 f_{slip} \quad (3.34)$$

Looking at the inverse- $\Gamma$  equivalent circuit at a standstill in Figure 3.22, the rotor side is composed of just the rotor resistance  $R_R$ , since the rotor leakage inductance  $L_{lr}$  is shifted on the stator side.

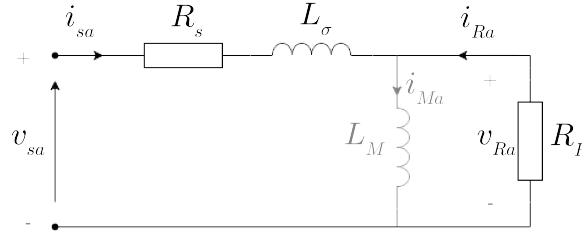


Figure 3.22: Single phase electrical equivalent circuit in phase a for locked rotor test.

As a consequence, the rotor current  $\mathbf{i}_R$  is a resistive current in phase with the voltage in phase a. The magnetizing inductance is neglected for the same reason as in Section 3.3.2.2. So, the  $\alpha$  (or a) component of the rotor current corresponds to the  $\alpha$  (or a) component of the stator current. Moreover, the a-axis overlaps with the  $\alpha$ -axis, as shown in the transformation.

$$\mathbf{i}_R = i_{Ra} = i_{sa} = i_{s\alpha} \quad (3.35)$$

The voltage on the stator is assigned. To find the voltage on the rotor resistance, the inverse formula from Equation (3.24). In the case of a sinusoidal constant frequency injection, the Equation (3.24) is written in phasor form.

$$\begin{aligned} \dot{V}_{Ra} &= (V_{R\alpha} + jV_{R\beta}) = \dot{V}_{sa} - (R_s + j\omega_l L_\sigma) \dot{I}_{sa} = \\ &= V_{s\alpha} - (R_s + j\omega_l L_\sigma) (I_{s\alpha} + jI_{s\beta}) \end{aligned} \quad (3.36)$$

where the stator resistance and the leakage inductance were previously estimated.

Knowing the voltage on the rotor resistance and the rotor current, the rotor

resistance of the inverse- $\Gamma$  equivalent circuit is:

$$R_R = \frac{|\dot{V}_{Ra}|}{|\dot{I}_{Ra}|} \quad (3.37)$$

$$\cos(\theta_R) = \frac{V_{R\alpha}I_{s\alpha} + V_{R\beta}I_{s\beta}}{|\dot{V}_{Ra}| |\dot{I}_{sa}|} \quad (3.38)$$

$$R_R = \frac{V_{R\alpha}^2 + V_{R\beta}^2}{V_{R\alpha}I_{s\alpha} + V_{R\beta}I_{s\beta}} \quad (3.39)$$

The rotor resistance, as the stator resistance, is very sensitive to temperature variation. For this reason, an online estimate is suggested also in this case.

From the standard IEEE 112-2017 in [3], the rotor resistance is found by performing the locked rotor test described in Section 3.3.2.2, whose result represents a benchmark for  $R_R$ .

## Chapter 4

# Practical implementation

### 4.1 Software tools

The first step to applying the methods chosen from the state-of-the-art self-commissioning in Section 3.1 is by creating simulation models for each of the electrical machines in analysis. These are later validated through the experimental setup, described in Section 4.2.

The primary software used is Matlab Simulink, which is directly linked with the Imperix **Software Development Kit (SDK)**. With the help of the **SDK**, a unified development environment is created that can be used to simulate the control and generate code for experiments through the **Automated Code Generation (ACG)**. This highlights the ability to easily switch between simulations and experiments. Each simulation file comprises a Controller block and a Plant model block. A typical scheme of the simulation model is presented in Figure 4.1.

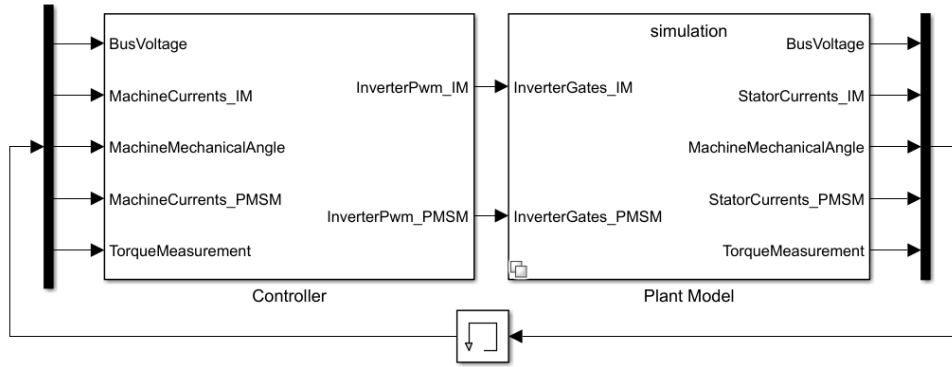


Figure 4.1: Simulink model of dual Imperix motor testbench.

#### 4.1.1 Full self-commissioning routine

Imperix provided files in which some control strategies, used in this work, are developed, for instance, **RFOC** for **IM**, **FOC** for **SPMSM**, **PR** controller for AC injection and I-f start-up (employed for **PM**-flux estimation). Figure 4.2 represent the flowchart of the entire self-commissioning routine for the **SPMSM** (a) and the **IM** (b). The procedure is composed of a set of sequential steps, since the estimation of a parameter depends on the knowledge of another one, for instance, to estimate the magnetizing inductance  $L_M$  the leakage inductance  $L_\sigma$  has to be known. Once the parameters are found, the control gains of the **CC** for the **FOC** are tuned. The only information that has to be entered into the algorithm by the user is the rated values from the nameplate data.

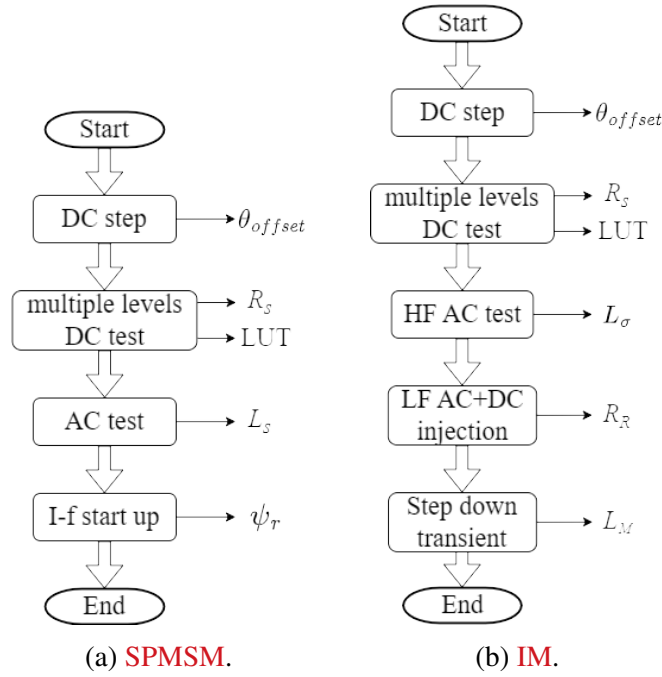


Figure 4.2: Algorithm flowchart of self-commissioning routine.

## 4.2 Hardware tools

The motor drive bundle, presented in the knowledge base section [43] of the Imperix website, is employed to experimentally verify the state-of-the-art self-commissioning. The motor drive bundle in Figure 4.3 is composed, from top to bottom, of the control stage and the power stage. The control stage is represented by a B-Box RCP and its motor interface. The power stage is composed of two inverters, in this project 4U Closed Rack – Type C, and a reversible DC supply.

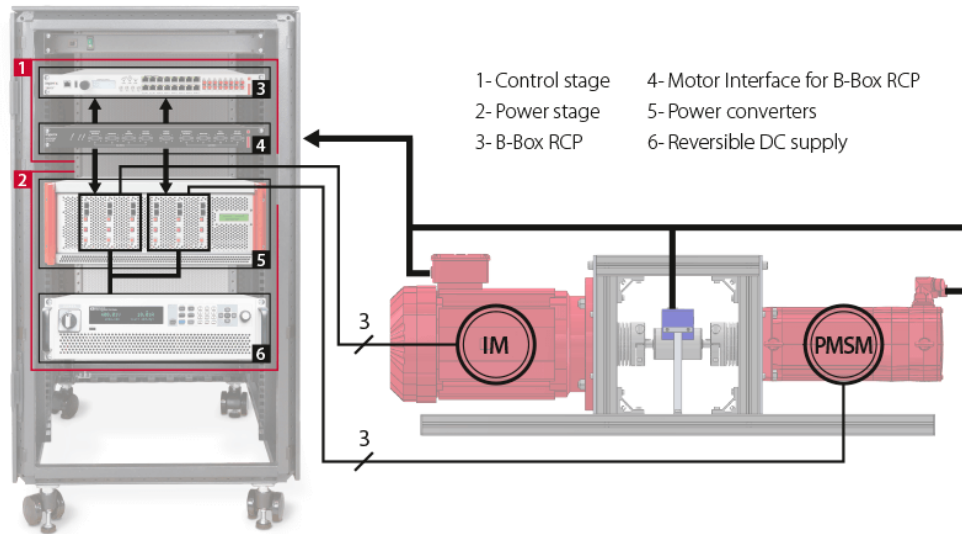


Figure 4.3: Default configuration of the motor drive bundle (front view).

#### 4.2.1 Control stage

The first element of the control stage is the B-Box **Rapid Control Prototyping (RCP)**.

The B-Box controller generates the control signals for the converter (PWM gate signals), based on the feedback of motor currents and DC bus voltage, measured with the embedded sensors on the PEB 8038. The gate signals are transmitted to the PEB 8038 modules through optical fibers, where the switches apply the signal by adjusting the duty cycle of the machine phase current waveform. The motor currents and the DC bus voltage are then fed back to the controller through RJ45 optical cables. To complete the loop the signal employs a delay time ( $T_d$ ) equal to one switching period ( $T_s$ ) and a half ( $T_d = 1.5T_s$ ) due to PWM time delay.

The second element of the control stage is the Motor Interface. The Motor Interface is an extension of the B-Box **RCP** and supports a wide variety of sensors relevant to motor control applications. It is designed for use with a dual motor setup such as the Imperix Motor Testbench. The position and speed of each motor can be measured either by an incremental encoder, a resolver, hall sensors, or a sin/cos encoder.

### 4.2.2 Power stage

The electrical equivalent circuit in Figure 4.4 shows the entire system composed of the motor testbench, two inverters, and a DC bus. One machine is the **Device Under Test (DUT)**, working as a motor (M) or as a generator (G), while the other one acts as a controllable load.

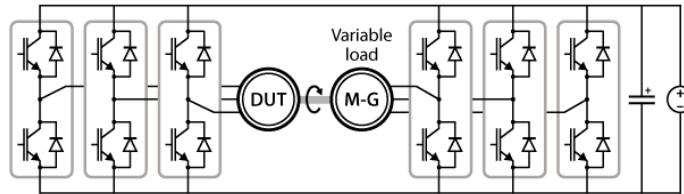


Figure 4.4: Dual-motor configuration with a shared DC bus.

The wiring of the power stage to the motor testbench is depicted in Figure 4.5.

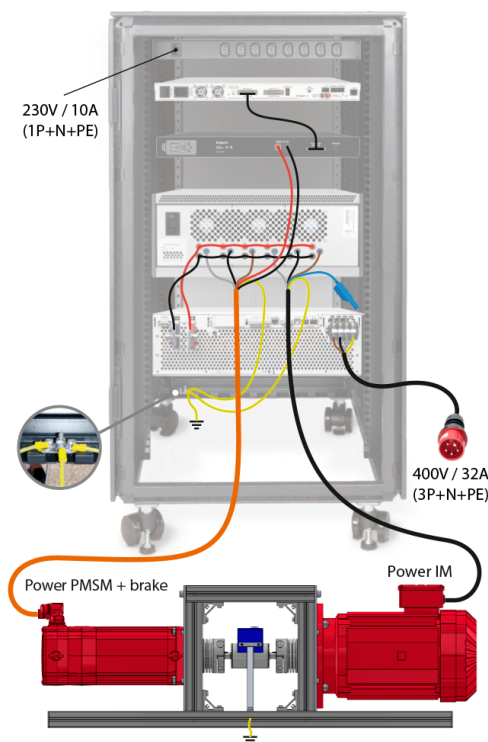


Figure 4.5: Wiring of the power stage and earthing connection (rear view).



### 4.2.3 Dual Motor testbench

The Motor Testbench shown in Figure 4.6 is composed of:

1. **IM** terminal box, in which the stator winding ends are connected to a terminal block for the **IM** power supply.
2. Squirrel cage DRN112M4 **IM** from SEW Eurodrive [44], consisting of a laminated rotor core attached to a steel shaft. The stator winding, encapsulated with synthetic resin, is inserted into the half-closed slot on the laminated stator core. This laminated core and the motor housing form the stator. The stator is star-connected at the factory. However, since the windings (and the neutral) are user-accessible, it is possible to wire them in a double-star or delta configuration. The temperature feedback is provided by a 4-wire PT1000 sensor installed on one of its windings. The main specifications are given in Table A.1.
3. Flexible couplings. Both machines are coupled to the torque sensor using KB4HC/80-89-N14-N28 bellows couplings from KBK Antriebstechnik GmbH. They provide a high torsional stiffness while allowing shaft misalignments. The use of flexible couplings allows a small misalignment of the shafts. As a result, the torque sensor has some backlash by design and can vibrate a little bit. This translates into an oscillation in the measurement at the mechanical frequency of the rotor.
4. Bidirectional torque sensor series 2200 from NCTE 2.
5. Mechanical brake, installed on the **PMSM**. It is activated by default to hold the rotor in place, but it is also suitable for repetitive emergency braking. The brake is released by energizing its coils with a 24 V signal.
6. CM3C80L **PMSM** from SEW Eurodrive [45] with a star connection. The three-phase stator winding is user accessible but, unlike the **IM**, not the neutral cable. The rotor is characterized by surface mounted **PM**. Like the **IM**, it features a 2-wire PT1000 sensor for temperature feedback directly installed on the motor winding. The main specifications are given in Table A.3.
7. Power and signals plugs for **PMSM**.
8. Resolver, installed on the **PMSM** for the measurements of absolute mechanical rotor angular position. Since **PMSM** and **IM** are coupled

on the same shaft, the resolver provides the position of both machines. Following IEC 60034-8 [46], the position angle increases when the shaft rotates in the clockwise direction of the **PMSM**. The resolver has to be aligned with the pole of the machine. For this reason, the resolver offset is found with the apposite calibration procedure before starting the self-commissioning routine. A direct current is injected into phase a of the **PMSM** to force the alignment of the rotor and stator fluxes. Once the rotor reaches a steady state, the measured mechanical angle representing the resolver offset is registered. This procedure is performed only once since the absolute zero of the resolver is fixed, consequently the offset angle is constant.

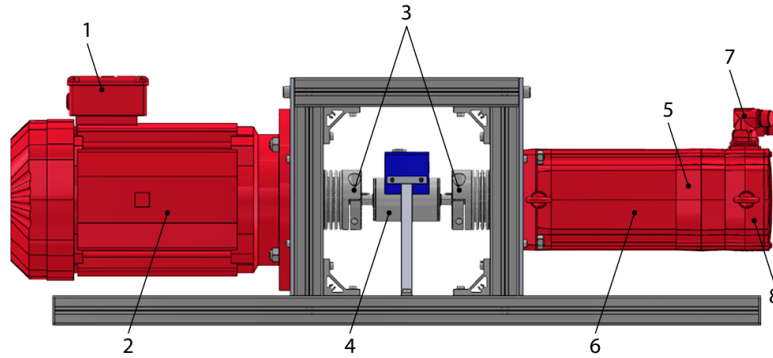


Figure 4.6: Overview of the dual motor testbench.

# Chapter 5

## Results and Analysis

In this chapter, the results from the method described in Chapter 3 are presented and discussed. They are performed using the experimental setup in Section 4.2, mated with the software environment in Section 4.1. The differences between the ideal case and the real case are highlighted.

During all the experimental tests, these values are set:

- the DC bus voltage is 300V.
- the value of deadtime of the MOSFET shown in Section 4.2.2 is  $t_{\Delta} = 500$  ns.
- the switching frequency is 20 kHz.

### 5.1 Results for SPMSM

#### 5.1.1 SPMSM stator resistance

##### 5.1.1.1 One-level DC injection and effect of inverter non-linearity

**5.1.1.1.1 Test description** The signal employed for the one-level DC injection method is depicted in Figure 5.1. No dead-time compensation is applied in this experiment. The corresponding theory of this method is in Section 3.2.1.1. From Equation (3.1) the system resistance estimate is  $0.94 \Omega$  without correcting the reference voltage.

This setup can be compared with the corresponding simulation presented in Figure 3.2, which lacks any dead time. This comparison aims to demonstrate the extent to which the d-axis component of the reference voltage in Figure 5.1

(b) increases compared to the ideal scenario in Figure 3.2 (b) (indicated by the red curves).

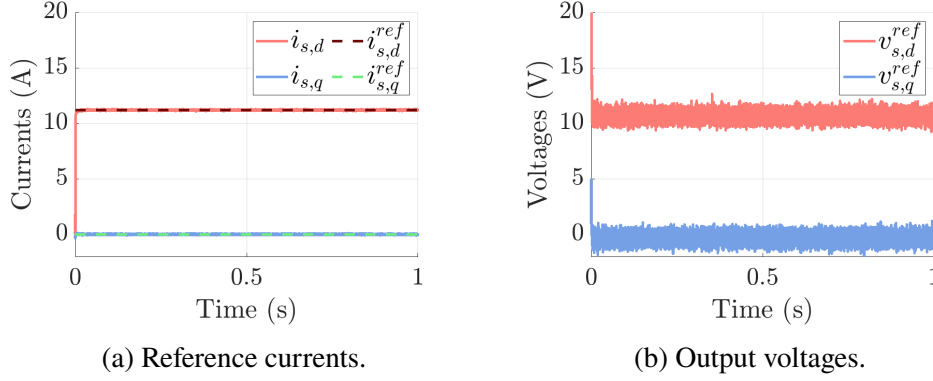


Figure 5.1: One level DC injection with CC, step at 0 s from zero Ampere to the rated value  $I_{sn}$  without dead time compensation.

**5.1.1.1.2 Test analysis** In both instances, the actual currents accurately follow their respective references. However, in the ideal scenario depicted in Figure 3.2 (b), the voltage is lower than in the experimental test shown in Figure 5.1 (b) (as indicated by the red curves, approximately half). This discrepancy arises because, in the ideal case, only the machine resistance contributes to the voltage drop. Conversely, in the experimental scenario, the total resistance is higher due to external factors such as the setup outside the machine and the non-linearity of the inverter.

**5.1.1.1.3 Test description** Following this, compensation for the inverter non-linearity is introduced by incorporating the LUT depicted in Figure 5.6 into the system. The effect of this compensation is demonstrated in Figure 5.2. The corresponding simulated scenario is shown in Figure 3.3.

In this case, from Equation (3.1) the system resistance estimate is  $0.73 \Omega$ .

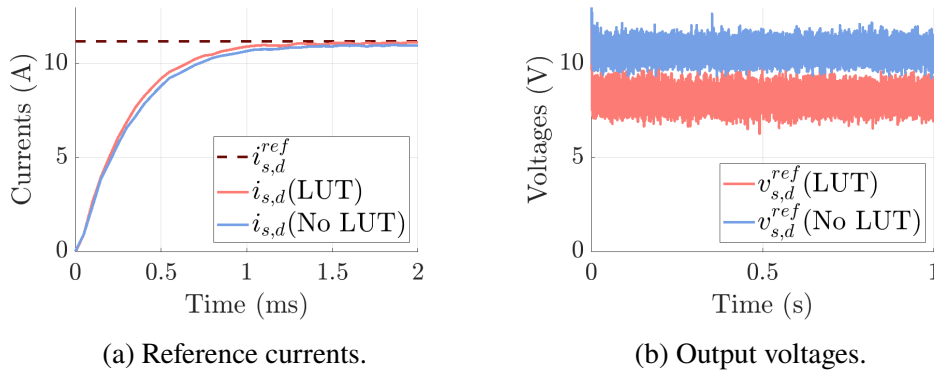


Figure 5.2: Effect of the **LUT** on control performances in the d-axis.

#### 5.1.1.1.4 Test analysis

1. Initially, the voltages with and without compensation for inverter non-linearity are compared (represented by the red and blue curves in Figure 5.2 respectively). When the **LUT** is integrated into the system, the voltage ( $v_{sd}^{ref}(\text{LUT})$ ) is lower compared to the case where no **LUT** is employed ( $v_{sd}^{ref}(\text{No LUT})$ ). With the inclusion of the **LUT**, the reference voltage more closely aligns with the actual phase voltage as it compensates for the non-linear drop ( $v_{sd} \approx v_{sd}^{ref}$ ). This allows using of the reference voltage for the estimation of the stator resistance from Equation (3.1).
2. Subsequently, the comparison between the simulated waveform (Figure 3.2) and the experimental waveform with compensated inverter non-linearity (Figure 5.2) is examined. Despite compensating for the inverter's non-linearity, the experimental voltage slightly exceeds the ideal case. This discrepancy arises because the resistance of the system in the experimental setup is higher than the simulated resistance, which only considers the machine resistance.

#### 5.1.1.2 Two-level DC injection

**5.1.1.2.1 Test description** The theory in Section 3.2.1.2 is subsequently analyzed in the experimental setup. The signal utilized for the two-level DC injection method is displayed in Figure 5.3. The corresponding simulation is presented in Figure 3.5. In Figure 5.3 (a), the dq currents accurately adhere to their references. The system resistance is identified with Equation (3.2). In this method, there is no need to apply the **LUT** for the  $R_s$  estimate because

Equation (3.2) gives directly the slope in the linear region of the characteristic voltage-current in Figure 3.4. As a result, the system resistance estimate is  $0.76 \Omega$ .

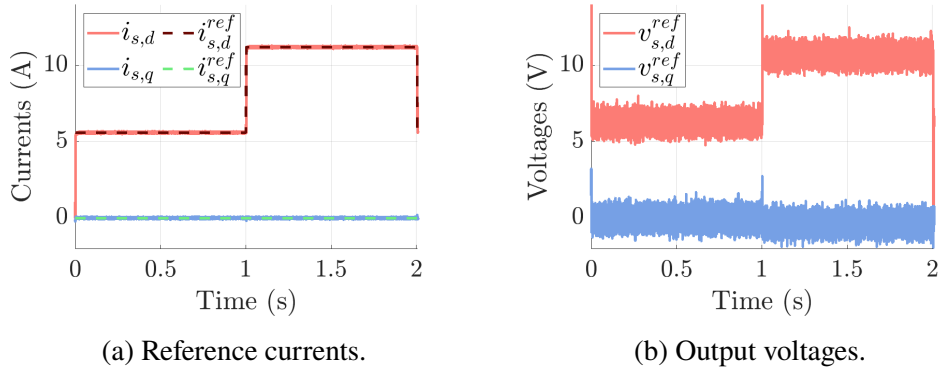


Figure 5.3: Two levels DC injection with **CC**, step at 1 s from  $0.5I_{sn}$  to  $I_{sn}$ , without  $t_{\Delta}$  compensation.

**5.1.1.2.2 Test analysis** In the experimental setup shown in Figure 5.3 (b), the voltage on the d-axis appears higher compared to the ideal scenario depicted in Figure 3.5 (b), as expected. This difference stems from the fact that, in the former case, the voltage drop is influenced by both the system's overall resistance and the inverter's non-linearity, whereas in the latter case, it is primarily governed by the machine's resistance.

### 5.1.1.3 Multiple-level DC injection and LUT identification

**5.1.1.3.1 Test description** For the multiple-level DC injection, the reference voltage and the measured current are shown in Figure 5.4. The number of steps is determined visually. Initially, 30 steps are taken between zero and a phase voltage of 5 V, followed by 12 steps until reaching the maximum value of 12 V, which corresponds to the rated current.

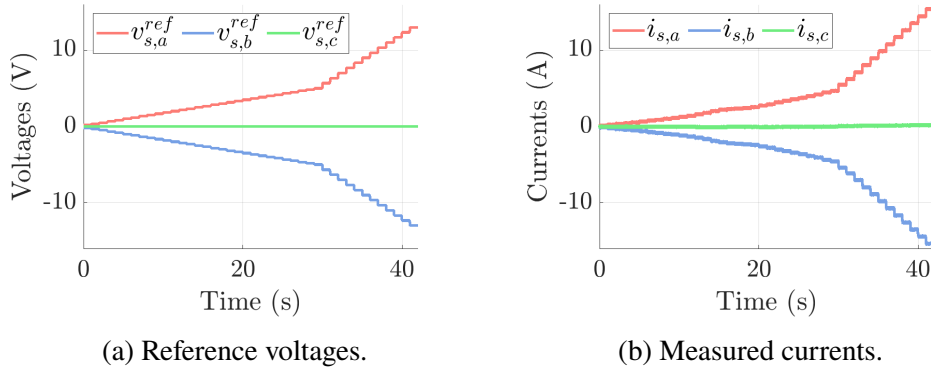


Figure 5.4: Multiple levels DC injection in OL, steps of 1 s.

For each step, the current and voltage values are recorded by averaging the samples within an observation window once the signals reach a steady state. These recorded data points are represented as dots in Figure 5.5 and Figure 5.6. Figure 5.5 reports the characteristic phase voltage-phase current ( $v_{s,a}^{ref}$ ,  $I_{s,a}$ ) and the ideal linear curve  $R_s I_{s,a}$ .

The system resistance extracted from the characteristic in Figure 5.5 through the Linear least-squares (LLS) is  $0.72 \Omega$ .

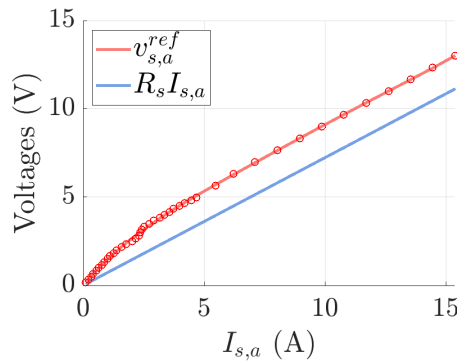


Figure 5.5:  $v_{sa}^{ref} = f(I_{s,a})$  for  $R_s$  estimation.

The voltage error  $v_{err} = v_{s,a}^{ref} - R_s I_{s,a}$  is then shown in Figure 5.6, where the blue dots are the data and the red curve represents the fit.

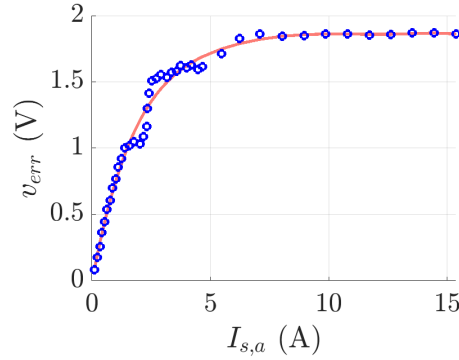


Figure 5.6:  $v_{err,a} = f(I_{s,a})$  for inverter non-linearity compensation.

#### 5.1.1.3.2 Test analysis

1. In Figure 5.5, the slope of the curve in the linear region represents the motor and cables' linear resistive elements. The difference between the ideal ( $R_s I_{s,a}$ ) and the reference curve ( $v_{s,a}^{ref}$ ) represents the non-linearity, and it is used to compensate for the voltage reference values generated by the control algorithm, to obtain a close match between the reference and the real phase voltage.
2. Figure 5.6 demonstrates that the error due to inverter non-linearity stabilizes at around 1.8 V. However, the expected theoretical value is around 3 V. The compensation of inverter non-linearity is achieved at 60% of the expected value. Further investigation is required to ascertain the reason for this discrepancy.

#### 5.1.1.4 Stator resistance benchmark measurement

The standard IEEE 1812-2023 proposes using a multimeter for measurements [5]. This is the benchmark for the self-commissioning procedures for stator resistance estimate. The comparison between the identification techniques is performed in Table 5.1.

The line-to-line system resistance is measured at the inverter input and halved to determine a phase resistance of  $0.705 \Omega$ . However, two digits after the decimal point for all comparisons are considered ( $0.70 \Omega$ ) because of the resolution of the multimeter. A Brymen BM785 multimeter is employed in this project, with its datasheet accessible in [47]. With an uncertainty of 0.03%, the measurement is deemed reliable and repeatable.



### 5.1.1.5 Discussion on the SPMSM stator resistance

The numerical results of the system resistance for the three estimation methods are given in Table 5.1 (second column).

The accuracy of the estimates is a consequence of the accuracy of the reference voltage and the measured current, which are subsequently discussed.

The measured current is taken from the current sensor embedded in the power module PEB8038 [43] of the inverter, with a sensitivity uncertainty of 1.1% to the actual value. This error can be reflected in the resistance estimate obtained from self-commissioning, leading to an error range of approximately  $\pm 0.008\Omega$  in the stator resistance estimate. Consequently, the error stemming from current measurements does not significantly impact the estimate.

The impact of noise on current measurement is assumed to be attenuated by considering the average value within an observation window.

As stated in Section 5.1.1.4, the measurement from a multimeter is considered in this work as a benchmark for the stator resistance estimate.

The errors relative to the measured value are calculated in the third column of Table 5.1.

Table 5.1: Comparison between stator resistance resulting from different methods, measured value of  $0.70\Omega$

Method	Estimate ( $\Omega$ )	$\frac{estimate - benchmark}{benchmark} (\%)$
One-level DC current injection (No LUT)	0.94	34.3
One-level DC current injection (With LUT)	0.73	4.3
Two-level DC current injection	0.76	8.6
Multiple-level DC voltage injection	0.72	2.8

Upon reviewing Table 5.1, it is inferred that the introduction of the LUT in the one-level current injection decreases the error to the benchmark of 30%.

The two-level DC injection method exhibits the highest error among the last three identification methods, with an error of 8.6%. This can be attributed to its consideration of the slope of the characteristic phase voltage-phase current (Figure 5.5) between half of the rated current and the rated current. In contrast, the multiple-level DC injection method only considers the last part of this characteristic (i.e., between  $0.7I_{sn}$  and  $I_{sn}$ ) for resistance estimation. It can be inferred that the closer the data used for the slope calculation are to zero current, the greater the effect of inverter non-linearity, leading to a higher deviation from the measured benchmark. Consequently, the two-level DC current injection method is deemed less accurate compared to the one-

level and multiple-level DC injection methods, whose results are consistent with the measurement uncertainties.

Additionally, the one-level DC injection is less accurate than the multiple-level case. A possible explanation for this is that the resistance estimate relies on the accuracy of the inverter non-linearity compensation. Instead, this dependency is eliminated by the **LLS** used with the multiple-level injection.

As a result, the last method outperforms the others, since the error to the measurement is less than 3%, resulting in being the more accurate.

## 5.1.2 SPMSM synchronous inductance

### 5.1.2.1 AC method

**5.1.2.1.1 Test description** The AC method detailed in Section 3.2.2.1 involves injecting a high-frequency (300 Hz) signal of d-axis current, with a peak current value equal to the rated value of  $11.2\sqrt{2}$  A. The q-current is kept to zero to avoid torque generation. Voltage compensation is performed using the **LUT** depicted in Figure 5.6. The actual current follows the sinusoidal reference in the d-axis thanks to the **PR** controller, as shown in Figure 5.7 (a). The action of the **PR** controller results in a distorted output voltage ( $v_{sd}^{ref}$ ) in Figure 5.7 (b). Its fundamental component ( $v_{sd}^{fund}$ ), used in the calculation of the synchronous inductance, is hence extracted with the **DFT**. Using eq. (3.6), the result of the synchronous inductance with the AC method is  $L_s = 5.5$  mH.

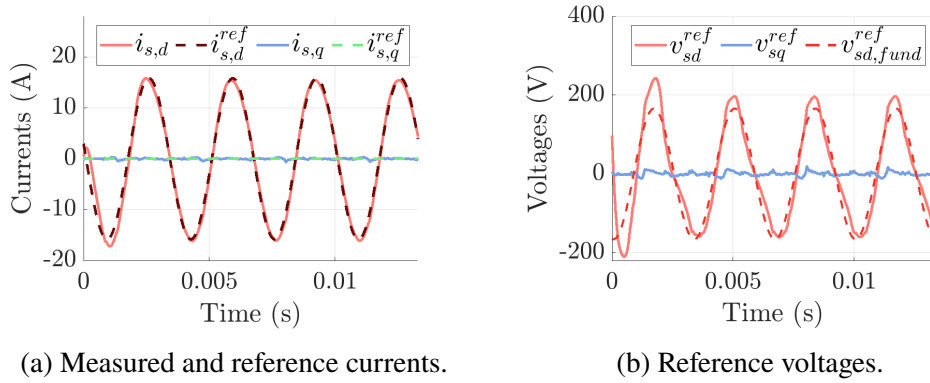


Figure 5.7: Current injection at a frequency of 300 Hz in dq0 reference frame.

**5.1.2.1.2 Test analysis** In this test, the reference voltage is used for the inductance estimation. However, the reference is applied with a delay due to the drive system that needs to be compensated to satisfy the identification of

reference and measurement voltage. Hence, this test is particularly sensitive to **PWM** phase delay compensation.

An additional drawback is that this test does not provide insights into the saturation behavior of the machine.

### 5.1.2.2 DC+AC method

**5.1.2.2.1 Test description** This section presents the experimental outcomes corresponding to the theory outlined in Section 3.2.2.2. The DC component of the reference current undergoes nine arbitrary steps, ranging from zero to the rated peak value of  $11.2\sqrt{2}$  A. To ensure steady-state conditions, each step is maintained for three seconds. Additionally, an AC component, with a peak of 2 A, is superimposed onto the DC current. For each DC step, the synchronous inductance is computed, which data are represented as blue dots in the characteristic  $(i_{sd}, L_s)$  in Figure 5.8.

From Figure 5.8, the inductance at zero current is 5.5 mH, this is called the "unsaturated value".

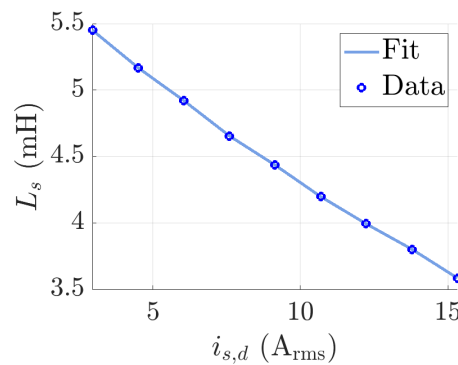


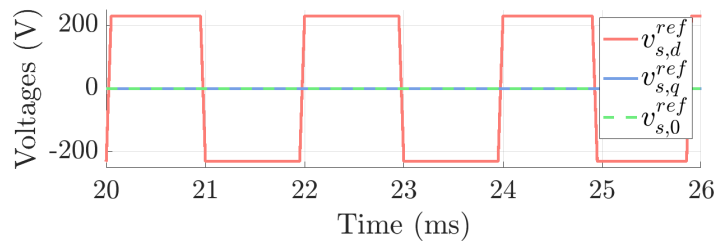
Figure 5.8: d-axis saturation characteristic with AC+DC injection at frequency of 300 Hz.

**5.1.2.2.2 Test analysis** Observing the saturation characteristic in Figure 5.8, a reduction of the inductance of around 35% is registered in the rated current range, unlike the **IM** with its 60% reduction (Figure 5.19). The less sensitivity of the **SPMSM** to saturation is due to its mostly isotropic structure, allowing the flux to primarily travel through the air gap.

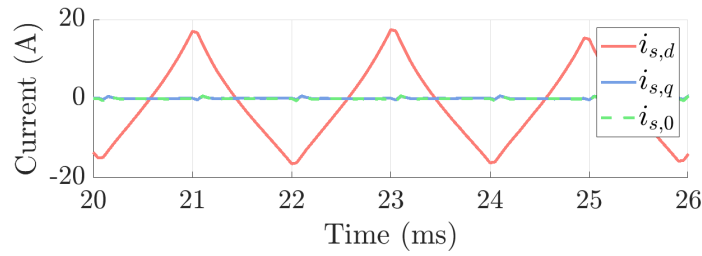
This work shows that even if **SPMSM** saturation is low compared to other AC machines (such as for the **IM**), it cannot be assumed constant in the entire rated range.

### 5.1.2.3 Hysteresis control

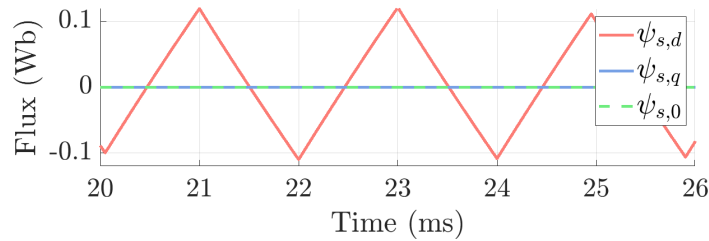
**5.1.2.3.1 Test description** The outcomes of the theory discussed in Section 3.2.2.3 are outlined in this section. The square wave reference voltage injected into the d-axis is depicted in Figure 5.9 (a). The output voltage of the hysteresis controller is arbitrarily chosen as  $\pm 230$  V for the d-axis and zero for the q-axis, intended to prevent torque generation and hence rotor movement. Subsequently, the corresponding measured current in the dq0 reference frame is presented in Figure 5.9 (b). Lastly, the flux resulting from the voltage integrator is illustrated in Figure 5.9 (c).



(a) Voltage.



(b) Current.



(c) Flux.

Figure 5.9: Hysteresis control experimental waveform in dq0 reference frame.

Subsequently, the saturation characteristic in Figure 5.10 (a) is obtained by plotting the flux versus current in the d-axis. The synchronous inductance,

extracted using Equation (3.13), represents the slope of the saturation characteristic and it is plotted versus the d-axis current in Figure 5.10 (b).

From Figure 5.10 (b), the unsaturated value of synchronous inductance, taken at zero current, is 6.7 mH.

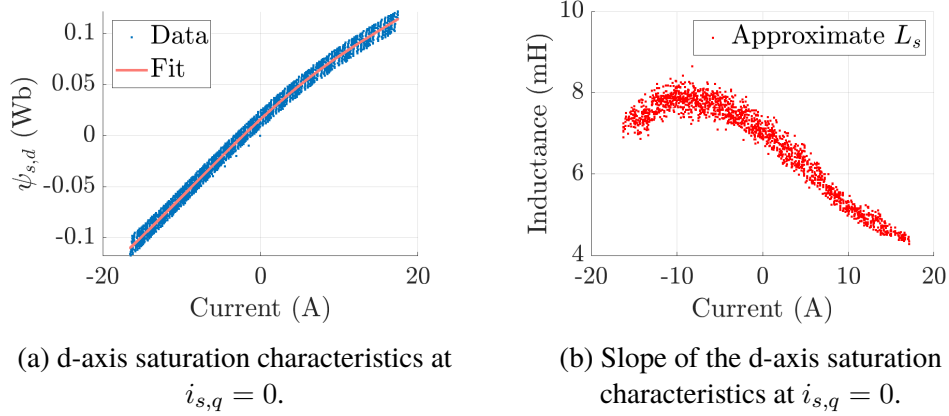


Figure 5.10: Hysteresis control on the d-axis.

#### 5.1.2.3.2 Test analysis

1. Figure 5.9 (b) can be juxtaposed with the simulated current depicted in Figure 3.11 (b), where constant inductance is assumed. This comparison highlights the effect of saturation on the rising fronts of the triangular waveform becomes evident, marking an inflection point at zero current. This comparison shows that even with this test the saturation effect affects the behavior of the machine and it cannot be neglected.
2. As observed in the simulation conducted in Section 3.2.2.3, the drift of the voltage integrator is also evident in the experimental tests. The drift worsens with increasing time, necessitating the limitation of the acquisition window. In this study, the voltage is injected for a duration of 100 ms. This duration corresponds to 2000 time samples based on the switching period. Following the 100 ms period, the reference voltage is reset to zero. The effect of the integrator offset is to translate the saturation characteristic on the y-axis. However, the slope of the curve is not affected by this. For this reason, the extracted inductance is assumed accurate.

### 5.1.2.4 Short-circuit benchmark test

**5.1.2.4.1 Test description** The experimental results corresponding to the theory exposed in Section 3.2.2.4 are subsequently presented.

The prior analysis is done subsequently.

- First, the safety conditions are verified by calculating the short circuit current, which results to be double the maximum allowed current value from the datasheet in Table A.3 ( $I_N^{max} = 34.9 \text{ A}_{pk}$ ,  $I_{sc} = 67 \text{ A}_{pk}$ ). For this reason, a mainly inductive external impedance is placed in series to each machine phase. However, they are slightly unbalanced, so the average value between the phases is computed resulting in 4 mH. From the datasheet, the SPMSM impedance is 4.24 mH. As a result, the impedance of the entire system is almost doubled and the safety conditions are satisfied by computing the new short circuit current. The peak phase current in Figure 5.11 (b) matches the theoretical calculations. To prevent the SPMSM from over-current, the protection system in the B-Box is set to the maximum allowed current.
- By testing, the torque capability of the IM is enough to supply the short-circuit torque to the SPMSM. Hence, the short circuit is applied before the start of the experiment. For this reason, the high currents at the start of the machine are avoided, as shown in Figure 5.11 (b).

The shown test in this section is performed by accelerating the IM up to 2000 rpm, which corresponds to the rated speed of the SPMSM. Once the IM is accelerated, the induced voltages in Figure 5.12 are recorded with differential voltage probes and visualized on the oscilloscope.

Using Equation (3.18), the short circuit inductance is 4.28 mH.

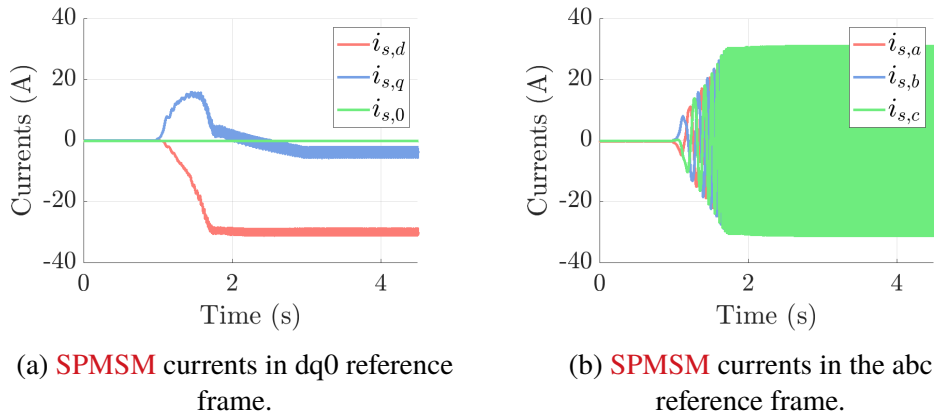


Figure 5.11: Measured current with DIN50 at rated frequency during the short circuit test.

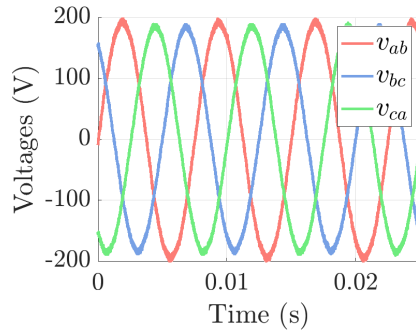


Figure 5.12: Short circuit test SPMSM line-to-line induced voltages at rated speed in the abc reference frame recorded with differential voltage probes and visualized on the oscilloscope.

#### 5.1.2.4.2 Test analysis

1. The possible risk of demagnetization is confirmed by the negative d-axis current in Figure 5.11 (a). The negative current of around 35 A is close to the threshold set by the machine manufacturer of 0.5 the maximum current. However, the test is performed for a limited amount of time (less than 5 seconds) so the machine does not demagnetize.

#### 5.1.2.5 Discussion on the SPMSM synchronous inductance

In this section, the results from the three estimation methods are summarized in Table 5.2. The estimates of the unsaturated synchronous inductance are in

the second column. In particular, the unsaturated inductance corresponds to a specific point on the saturation characteristic from the self-commissioning procedures where the current approaches zero.

The result of the short-circuit test is selected as a reference point. When the stator winding is short-circuited, the stator magnetic field is nearly neutralized by the rotor's reaction. This cancellation would be complete without any resistors. Consequently, under these circumstances, the magnetic material demonstrates almost linear behavior, even at the rated current.

Hence, the unsaturated inductance estimate from the self-commissioning procedures is compared to the short-circuit inductance. The resulting errors to the datasheet value and the short circuit value are calculated in the third and fourth columns respectively.

Table 5.2: Comparison between the unsaturated values of the synchronous inductance resulting from different methods, the result from the short circuit test is 4.28 mH.

Method	Estimate ( mH)	$\frac{estimate - benchmark}{benchmark} (\%)$
AC injection	5.5	28.5
AC+DC injection	5.5	28.5
Hysteresis control	6.7	56.5

The confidence in the outcome of the short-circuit test is increased by the correspondence with the measure from the LCR Matrix MCR-5200, which datasheet [48] shows an uncertainty of 0.1%.

Examining Table 5.2, all the self-commissioning procedures yield a higher inductance estimate compared to the benchmark. A possible explanation for this discrepancy could be found considering that the SPMSM is a low reactance machine. Hence the SPMSM inductance is very sensitive to compensation of PWM phase delay introduced by the experimental drive system.

A first observation is that the sinusoidal injections (AC and DC+AC methods) exhibit half the error recorded when using hysteresis control. The reason for this discrepancy needs to be further investigated in future works.

Additionally, from the comparison in Table 5.2, the finding of the AC+DC injection matches that of the AC method. This suggests that the amplitude of the injected sinusoidal signal does not affect the machine saturation state and so the estimation of the synchronous inductance.



### 5.1.3 SPMSM PM-flux

#### 5.1.3.1 I-f startup + sensorless FOC

**5.1.3.1.1 Test description** In this section, the results related to the theory presented in Section 3.2.3.1 are described. The experimental test in Figure 5.13 matches the corresponding simulation in Figure 3.16.

First, a reference mechanical ramp speed  $\omega_{m,est}$  is set at  $t=0$  s. The measured mechanical speed  $\omega_{m,real}$  rises in OL. As a consequence, the tracking of the reference results in high oscillations of real speed. During the speed ramp, the q-axis current is controlled close to the rated peak value to provide the power necessary to the SPMSM to speed up. The rated value is not set as a reference of the CC because the current oscillations trigger the protection system in the B-Box set to 1.2 the rated value of the current.

At 0.8 s, the constant speed of 800 rpm is reached. This value is arbitrarily chosen because it allows for a reduction of the amplitude of the speed oscillations at constant speed. These oscillations are due to a misalignment of the shafts in the test bench. This choice of speed prevents the SPMSM from heating up. Additionally, sensorless control mainly relies on the estimate of machine parameters for the back-EMF estimate. At higher speeds, the sensorless control is less sensitive to errors in the machine parameter estimate. As a consequence, the tracking of the estimated speed better matches the real one.

After 0.8 s the q-axis current starts to decrease, while the speed is kept constant.

At  $t=2$  s the reference current and the angle of the alignment error between the real and the virtual rotating reference frame are close to zero. So the control is switched to a sensorless FOC. The machine is not OL controlled anymore. Since the current is zero, the speed starts decreasing, as well as the phase voltage.

Their ratio in Equation (3.22) results in the PM-flux estimate of 0.2814 Wb.

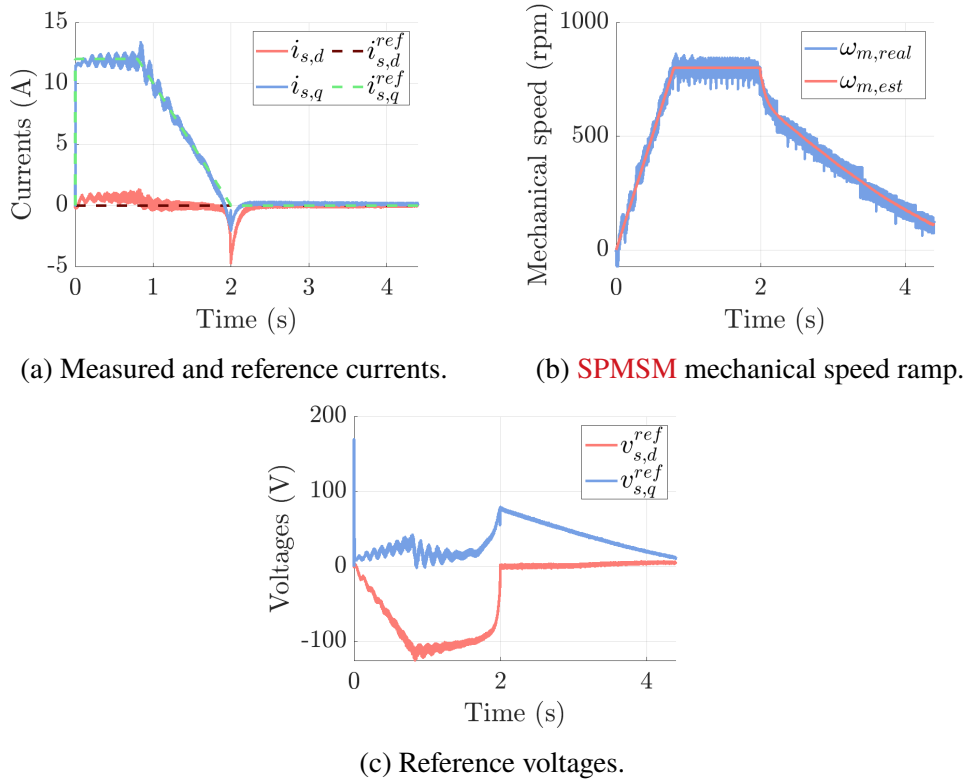


Figure 5.13: Experimental I-f startup from  $t = 0$  s and sensorless FOC at null references in dq0 reference frame introduced at  $t = 2$  s.

### 5.1.3.1.2 Test analysis

1. For this calculation, the speed in Equation (3.22) is the estimated one. At high speed the sensorless FOC is less sensitive to errors in parameter estimate. Hence, the estimated speed tracks the real speed with good performance, as seen in Figure 5.13 (b) (after 2 s). Using the estimated speed instead of the real one does not introduce any further significant inaccuracy in the system.
2. The PM-flux is estimated in Equation (3.22) using the reference voltage, instead of the measured one. This choice is justified by the inclusion of the LUT in the control algorithm to compensate for inverter non-linearity. Moreover, due to the high voltages, this test has low sensitivity to inverter non-linearity. As a consequence, inverter non-linearity does not represent a possible source of inaccuracies for the PM-flux estimate.

### 5.1.3.2 Open-circuit benchmark test

**5.1.3.2.1 Test description** The experimental results corresponding to the theory in Section 3.2.3.2 are shown in Figure 5.14. These match with the corresponding simulated test is in Figure 3.18.

In Figure 5.14 (a), the **IM** mechanical speed  $\omega_{IM}$  follows the reference  $\omega_{IM}^{ref}$  of 800 rpm. This value is chosen following the same reasoning presented in Section 5.1.3.1. The **SPMSM** line-to-line voltages are shown in Figure 5.14 (b). The **PM**-flux is estimated 0.2843 Wb using Equation (3.23).

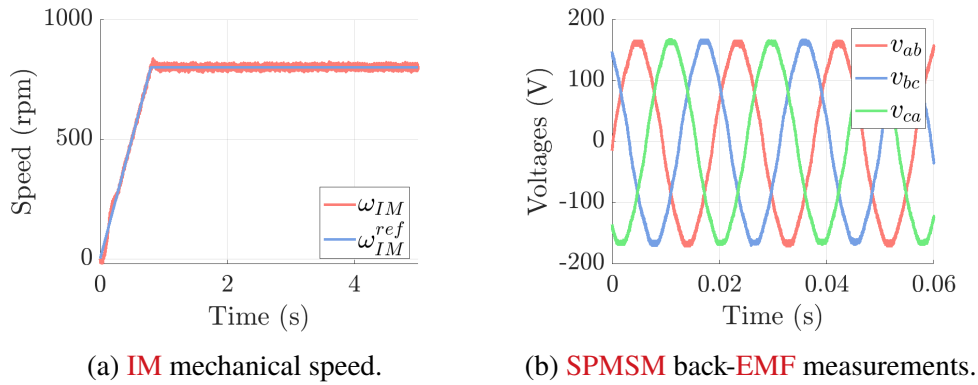


Figure 5.14: Open-circuit test.

**5.1.3.2.2 Test analysis** For the voltage measurements, a digital oscilloscope (RIGOL MSO5074 [49]) is used for the visualization of the waveforms. The voltage waveforms are directly measured from the phase of the electrical machine thanks to differential voltage probes (Micsig DP10013 [50]). The differential voltage probes have a gain accuracy of  $\pm 2\%$ , which gives an error range of  $\pm 3$  V out of around 150 V. This error range does not critically affect the **PM**-flux estimate, which is then considered as a reliable benchmark.

### 5.1.3.3 Discussion on the SPMSM PM-flux

The result for the **PM**-flux is presented in table 5.3 where the estimated value using the I-f startup + sensorless **FOC** is in the first column.

In the second column, the error between the outcome of the I-f startup + sensorless **FOC** and the result from the open-circuit test is given.

Table 5.3: Comparison between PM-flux estimates, the result from the open-circuit benchmark test is 0.2843 Wb.

Method	Estimate (Wb)	$\frac{estimate - benchmark}{benchmark} (\%)$
I-f start-up+sensorless <b>FOC</b>	0.281 4	-1.0

Table 5.3 shows that the outcomes from the two identification methods successfully align, technically validating the proposed procedure of I-f start-up+sensorless **FOC**.

## 5.2 Results for IM

### 5.2.1 IM stator resistance

The same methods used for the **SPMSM** in section 5.1.1, namely one-level, two-level, and multiple-level DC injection, are implemented for the **IM**. As for the **SPMSM**, the last method performs better than the first two (see Table 5.4). For this reason, only the waveforms related to the multiple-level DC injection method are subsequently shown.

#### 5.2.1.1 Multiple-level DC injection and LUT identification

**5.2.1.1.1 Test description** In Figure 5.15 (a), a total of 20 steps of reference voltages are executed, ranging up to 10 V. Subsequently, the number of steps is halved within the linear region between 10 V and 20 V. The number of steps is visually chosen. The phase currents, measured with the current sensors embedded in the power modules, are shown in Figure 5.15 (b).

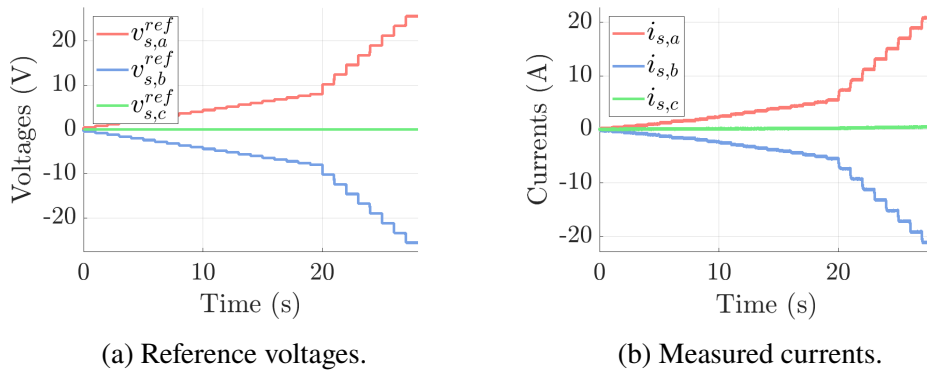


Figure 5.15: Multiple levels DC injection in **OL**, steps of 1 s.

The system resistance estimate is  $1.13 \, \Omega$ , extracted from the characteristic phase current-phase voltage in Figure 5.16 using the LLS.

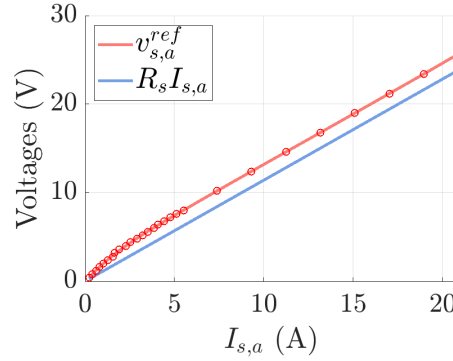


Figure 5.16:  $v_{sa}^{ref} = f(I_{s,a})$  for  $R_s$  estimation.

The voltage error versus phase current characteristic, used to build the LUT for the inverter non-linearity compensation, is finally shown in Figure 5.17.

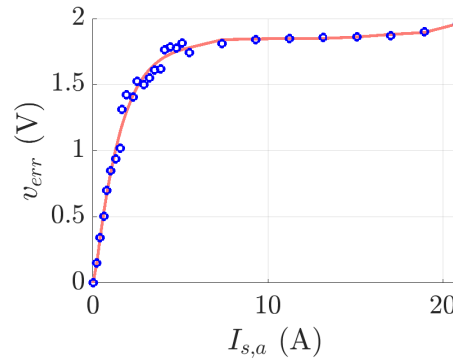


Figure 5.17:  $v_{err,a} = f(I_{s,a})$  for inverter non-linearity compensation.

**5.2.1.1.2 Test analysis** Different power modules are utilized for the IM and the SPMSM, potentially introducing different non-linear behaviors into the system. Hence, the LUT is re-estimated for the IM. Upon comparing the LUT constructed for the SPMSM in Figure 5.6 with that built for the IM in Figure 5.17, it becomes apparent that the voltage error trend is similar. This observation enhances confidence in these experimental findings.

### 5.2.1.2 Stator resistance benchmark measurement

As seen for the **SPMSM** in Section 5.1.1.4, the chosen benchmark for the self-commissioning procedures is the stator resistance measurement. The line-to-line resistance is measured and subsequently halved to estimate a phase resistance of  $1.115 \Omega$ . Two decimal digits are considered because of the multimeter resolution (Brymen BM785), which is the same used for the **SPMSM**. With an uncertainty of 0.03%, the measurement is deemed reliable and repeatable.

### 5.2.1.3 Discussion on the IM stator resistance

The numerical results of the system resistance for the three estimation methods are given in Table 5.4 (second column). The errors to the measured value are calculated in the third column.

Table 5.4: Comparison between stator resistance resulting from different methods, measured value of  $1.11 \Omega$  (Brymen BM785 multimeter).

Method	Estimate ( $\Omega$ )	$\frac{estimate - benchmark}{benchmark} (\%)$
One level DC current injection (No <b>LUT</b> )	1.36	22.5
Two-level DC current injection	1.14	2.7
Multiple-level DC voltage injection	1.13	1.8

As for the **SPMSM** in Section 5.1.1.5, the multiple-level injection is the more accurate between the self-commissioning procedures. The two-level DC injection performs better in the **IM** than in the **SPMSM**. Since the test features are not changed, it can be deduced that the two-level DC injection performs better on machines with higher resistance.

## 5.2.2 IM leakage inductance

### 5.2.2.1 DC+AC method

**5.2.2.1.1 Test description** The first method to estimate the leakage inductance is the DC+AC injection presented in Section 3.3.2.1. The reference voltages, shown in Figure 5.18 (a), are injected in **OL** to create a single-phase configuration, ensuring a balanced load. The frequency of the injected signal is 300 Hz, chosen because of the reasons given in Section 3.3.2.1. An AC voltage component of arbitrarily 4 V peak is overlapped on 12 steps of the DC component. Each step lasts for 3 seconds, ensuring the inductance estimation

is performed in steady state condition. The maximum voltage is chosen to give the rated peak current. The **IM** phase currents in Figure 5.18 (b) are then measured through the sensors in the power modules .

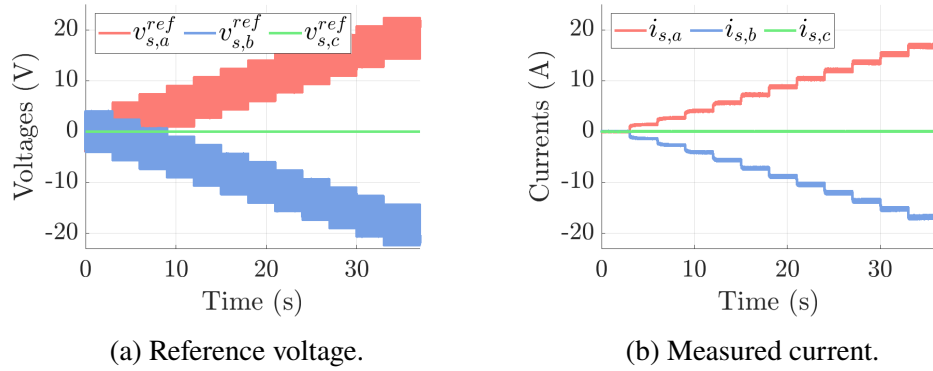


Figure 5.18: High frequency injection at 300 Hz.

For each set point the inductance is calculated from the fundamental components of voltage and current. The saturation characteristic of the leakage inductance is shown in Figure 5.19.

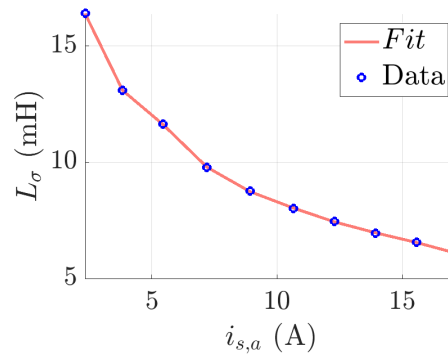


Figure 5.19: Saturation characteristic at a frequency of 300 Hz by DC+AC method.

**5.2.2.1.2 Test analysis** Unlike the **SPMSM**, the **IM** is more sensitive to the saturation effect, as shown by the reduction of its leakage inductance of around 60% between zero and rated current.

The saturation behavior of the machine is related to the structure of the rotor. Specifically, the **IM** stator windings are inserted into the half-closed

slot on the laminated stator core, as stated by the machine's manufacturer SEW Eurodrive [44]. In the case of a semi-closed slot, the bridges saturate by increasing the current, so its permeability becomes similar to that of the air. This phenomenon is modeled from a magnetic point of view by an increase in the openings.

Hence, a semi-closed slot design is sensitive to saturation and the behavior shown in Figure 5.19 is compatible with the theory presented in Electrical Machine by Cavagnino in [7].

### 5.2.2.2 Locked rotor benchmark test

**5.2.2.2.1 Test description** The second method used to identify the leakage inductance is the locked rotor test presented in Section 3.3.2.2. The current is measured through a current probe and the phase voltage with a differential voltage probe placed at the output of the inverter. The DFT is used to extract the fundamental component of phase voltage and current. The harmonic spectrum of the measured voltage and current is in Figure 5.20. The fundamental components are used in Equation (3.30) to calculate the impedance of the IM, which imaginary part is 16.7 mH. The real component of the IM impedance is 0.59  $\Omega$ .

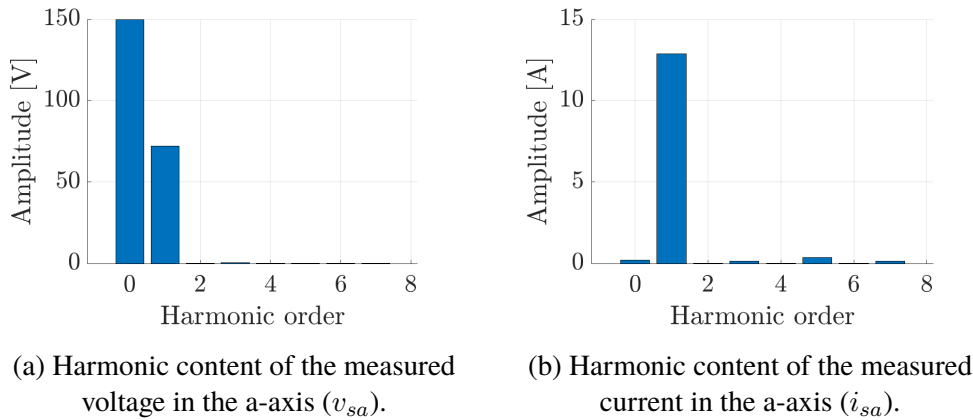


Figure 5.20: Harmonic content resulting from the DFT of current and voltage measurement in phase a.

**5.2.2.2.2 Test analysis** During the locked rotor test, the magnetizing inductance is neglected because it is assumed to be much larger than the leakage inductance. However, in the experimental test, there may be some magnetic saturation, depending on the profile of the magnetization



inductance. Despite this, the result from the locked rotor test is assumed to be the unsaturated value, since this eventual effect of magnetic saturation is negligible. The error range introduced by the voltage measurement instruments is  $\pm 2\%$ , so  $\pm 1,5$  V out of 75 V, that is acceptable.

A current probe Micsig CP2100B [51] is used for the current measurement. Its uncertainty of around  $4\%$  can be translated to the estimation.

The locked rotor test outcome is then characterized by an uncertainty of around  $\pm 6\%$ .

### 5.2.2.3 Discussion on the IM leakage inductance

The results from the two identification procedures are summarized in Table 5.5. The estimate of the unsaturated leakage inductance, from the self-commissioning method, is in the second column. This value corresponds to the set point of the characteristic in Figure 5.19 at zero current. The accuracy of this estimate relies on the current measurement and the reference voltages. The currents are measured with the embedded sensor in the power module PEB8038 [43], which is  $1.1\%$ . The locked rotor test result, with an uncertainty of around  $\pm 6\%$ , is considered a benchmark and it is compared to the self-commissioning outcome. The error between the two identification techniques is presented in the third column.

Table 5.5: Comparison between the unsaturated values of the leakage inductance resulting from different methods, the locked rotor test result is 16.7 mH.

Method	Estimate ( mH)	$\frac{estimate - benchmark}{benchmark} (\%)$
DC+AC injection	16.4	-2.3

Given the uncertainties, Table 5.5 shows that the two analyzed identification procedures successfully align. Other possible explanations that could introduce discrepancies between the two tests are subsequently investigated.

The primary distinction between the tests is the voltage source used: self-commissioning employs the reference voltage, while the locked rotor test directly measures voltage. A potential discrepancy may arise between them due to inaccuracies in compensating for inverter non-linearity. This discrepancy is particularly pronounced given the low voltages involved in this test (less than 20 V), rendering it highly sensitive to compensate for voltage drop attributable to the inverter.

A further difference between the tests is the use of different current sensors, characterized by different uncertainties; the current probe for the locked rotor test and the sensor in the power module PEB8038 for the self-commissioning procedure.

Another source of error can come from the compensation of the PWM phase delay introduced from the drive system. However, the **IM** in this project is not considered a low-reactance machine. For this reason, it is not as sensitive as the **SPMSM** to PWM phase delay compensation.

## 5.2.3 IM rotor resistance

### 5.2.3.1 DC+AC method

**5.2.3.1.1 Test description** The results corresponding to the theory in Section 3.3.3 are presented. The three-phase reference voltages are injected in **OL** in a single-phase configuration. As shown in Figure 5.21 (a), the voltage in phase a is equal and opposite to the voltage in phase c. The amplitude of the DC component of the injected signal is arbitrarily chosen as 7 V to shift the signal to the linear region of the characteristic current - voltage. The AC component of the injected signal is arbitrarily chosen as 2 V. The measured current in the three-phase reference frame is finally given in Figure 5.21 (b). The waveforms are presented in the  $\alpha\beta 0$  reference frame, where the calculation for the rotor resistance estimation in Equation (3.39) is performed.

The rotor resistance estimated with this method is  $0.63 \Omega$ .

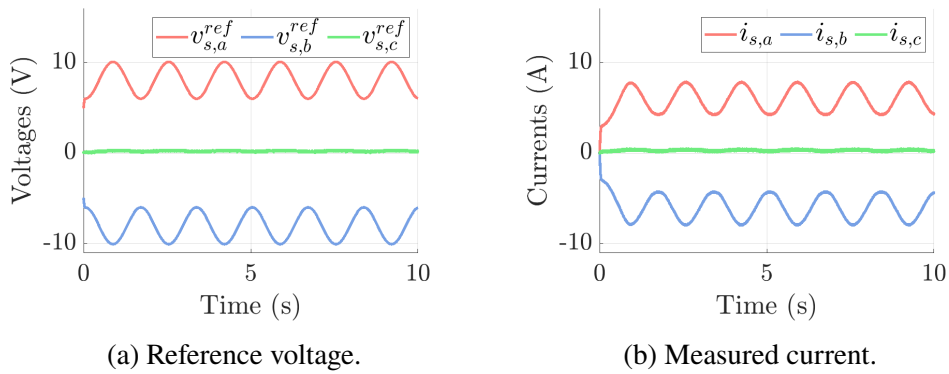


Figure 5.21: Single phase injection at a frequency of  $f_l = 0.6 \text{ Hz}$ ,  $V_{sa,dc} = 7 \text{ V}$ ,  $V_{sa,ac} = 2 \text{ V}_{pk}$  in the abc reference frame.

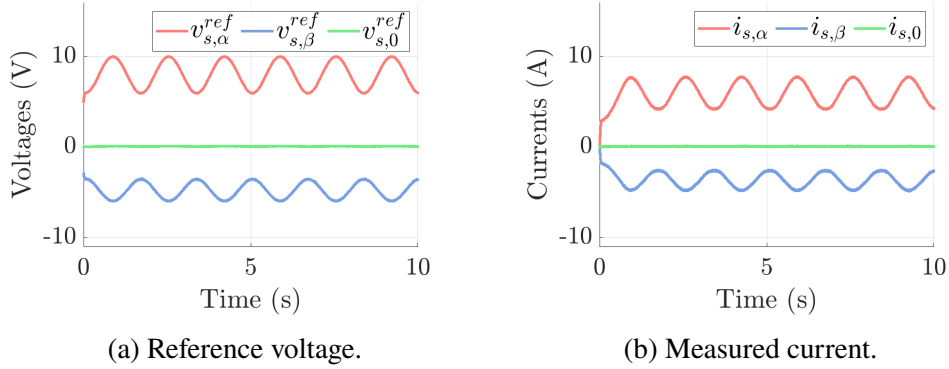


Figure 5.22: Single phase injection at a frequency of  $f_l = 0.6$  Hz,  $V_{dc} = 7$  V,  $V_{ac} = 2$  V<sub>pk</sub> in the  $\alpha\beta 0$  reference frame.

**5.2.3.1.2 Test analysis** In this analysis, just one arbitrary frequency is considered. However, the rotor resistance referred to the stator side ( $R_R$ ) changes with the slip, and hence with the frequency of the injected signal. For a more complete analysis, the characteristic  $(R_R, f_l)$  could be analyzed as in [8].

The current is measured from the sensor embedded in the power module PEB8038. Its uncertainty of 1.1% is translated to the self-commissioning outcome. Other possible uncertainties could be introduced by the difference between the reference voltage used for the self-commissioning procedure and the measured voltage in the locked rotor test due to inaccuracy introduced by the non-linearity compensation.

### 5.2.3.2 Locked rotor benchmark test

The second identification method of rotor resistance is the standard locked rotor test from IEEE 112-2017 [3] given in Section 3.3.2.2. The total value of the machine resistance  $R_{tot}$  is given by this test. By subtracting the stator resistance  $R_s$ , the rotor resistance referred to the stator side in the inverse-gamma equivalent circuit is  $R_R = R_{tot} - R_s = 0.59 \Omega$ .

### 5.2.3.3 Discussion on the IM rotor resistance

The results for the rotor resistance are summarized in Table 5.6. The estimated value with the self-commissioning procedure is presented in the first column. The uncertainty from the self-commissioning result is 1.1%. The locked rotor test result, with an uncertainty of around  $\pm 6\%$ , is considered a benchmark.

In the second column, the error between this estimate and the result from the locked rotor test is given.

Table 5.6: Comparison between rotor resistance resulting from different methods, the locked rotor test result is  $0.59 \Omega$ .

Method	Estimate ( $\Omega$ )	$\frac{estimate - benchmark}{benchmark} (\%)$
DC+AC injection	0.63	6.8

Given the uncertainties on the results, Table 5.5 shows that the two analyzed identification procedures successfully align.

## Chapter 6

# Conclusions and Future work

### 6.1 Conclusions

In industrial settings, a common challenge associated with electrical machines is the unavailability of machine parameters, which are not always provided by the manufacturer. These parameters play a crucial role in tuning the control gains, notably for Field Oriented Control (**FOC**).

Traditional parameter identification methods often rely on standard IEEE tests. However, implementing these tests can be impractical as they necessitate additional equipment that may be costly and not readily accessible. Additionally, they may require specific configurations, such as coupling with the load, which can be challenging for machines already installed on-site.

The self-commissioning procedures propose a solution to this problem. Self-commissioning for AC motor drives, addressed in this thesis, typically refers to the process of calibration, identification of machine parameters, and automatic tuning of control gains for a motor drive system. It is a standstill procedure that utilizes signal injection through a power converter and the available sensors with minimal operator intervention. It can be performed when the machine is operated (online) or one time before it starts up (offline).

This thesis aims to answer the research question of how can a state-of-the-art automatic identification procedure of parameters be implemented for the Imperix motor testbench, which is composed of Induction Machine (**IM**) and Surface Mounted Permanent Magnet Synchronous Machine (**SPMSM**).

To answer this research question the following goals were reached.

First, the electrical parameters to be identified were selected, based on the machine equivalent circuit used for the **FOC**. For the **SPMSM** the studied parameters were the stator resistance, the synchronous inductance,

and the Permanent Magnets (PM)-flux. For the IM the stator resistance, the leakage inductance, the rotor resistance, and the magnetizing inductance were identified.

A literature review regarding the parameter identification was performed. The references were analyzed and categorized based on the control configuration (open or closed-loop), and whether the method considers non-idealities on parameter identification, such as the effects of inverter non-linearity, saturation, or frequency.

Per each parameter, suitable methods were selected and implemented in simulation first, and then experimentally tested. To validate the self-commissioning procedure, the obtained results had to conform to those obtained following the IEEE standards, which were chosen as a benchmark.

The stator resistance was identified with one-level, two-level, and multiple-level DC steps. This parameter is sensitive to inverter non-linearity, whose effect was compensated through the characteristic voltage error-phase current used to build the Lookup Table (LUT) inserted in the control algorithm. The obtained value from the self-commissioning was compared to that from the corresponding standard test, which identified the stator resistance through measurements from the multimeter.

The result of the stator resistance analysis is that the multiple-level DC identification method aligned better with the standard than the first two estimation procedures. This is because the stator resistance is extracted from the phase voltage-phase current characteristic using the LLS, avoiding possible inaccuracies from the inverter non-linearity compensation. Other benefits of the multiple-level DC injection were that both stator resistance and inverter non-linearity characteristic were identified from the same signal injected and its Open Loop (OL) nature. Furthermore, unlike the one and two-level injection, the multiple-level injection avoids the necessary Current Controller (CC) tuning, leading to a more time-efficient identification routine.

Then, the high-frequency sinusoidal injection, with and without the DC bias, and the square wave voltage injection through hysteresis control were used to identify the synchronous inductance and its saturation characteristic. As a reference value, the corresponding IEEE standard implements a short circuit test to obtain the unsaturated synchronous inductance.

In all cases, a considerable mismatch was observed between the outcomes from the standard and the self-commissioning tests.

The last SPMSM parameter under study was the PM-flux, which was identified by rotating the SPMSM using the IM as a prime mover in open circuit configuration. This deviation from the standstill constraint of the self-

commissioning procedure was necessary as the **PM**'s effect becomes visible only when the rotor speed is non-zero. The result of this procedure aligns with the result from the IEEE standard open circuit test.

Regarding the **SPMSM**, it can be concluded that the self-commissioning procedure allows parameter identification with results almost aligned with the standard tests, except for discrepancies in unsaturated **SPMSM** synchronous inductance estimation. The confidence in the benchmark value from the standard tests is increased by the LCR measurement instrument, which has very high accuracy. A possible explanation for the discrepancy in inductance identification could be that the self-commissioning method applied to low reactance machines is very sensitive to the **PWM** phase delay introduced by the experimental drive system.

Subsequently, the **IM** parameters were discussed. The stator resistance was identified with the same procedures as for the **SPMSM**. The conclusions drawn for the **SPMSM** were confirmed also for the **IM**.

The leakage inductance of the **IM** was identified with the high-frequency sinusoidal injection with stepped DC bias to build the saturation characteristic. The unsaturated value, corresponding to the set point of the characteristic at zero direct current, aligned with the imaginary part of the impedance obtained from the locked rotor test, as recommended by the IEEE standard.

The rotor resistance referred to the stator side was estimated with low-frequency sinusoidal injection with DC bias. The outcome of this identification method matched with the real part of the impedance identified from the locked rotor test.

The magnetizing inductance was not determined in this work because of the extensive nature of the problem and time constraints.

It can be inferred that the self-commissioning strategies tested on the **IM** are technically relevant because their outcomes are comparable with the IEEE standard tests, widely accepted by the scientific community. Unlike the **SPMSM**, the **IM** is more sensitive to the saturation effect. For this reason, the effect of saturation on control performance could result in larger variations of the control gains than in the **SPMSM** applications.

Overall, the following general conclusions are raised.

- This work largely addresses the research question, comprehensively outlining the self-commissioning identification process for six out of seven parameters. Among these six, five align with the results obtained from the IEEE standard tests, making them technically relevant.
- This research reinforces the widely accepted idea in the literature

that utilizing a reference voltage for parameter estimation is viable with careful compensation of inverter non-linearity, eliminating the requirement for extra voltage measurements.

- This study inaugurates the application of DC-biased high-frequency injection and square-wave injection on **SPMSM** for saturation characteristic estimation. The resulting saturation characteristic significantly advances parameter identification knowledge.
- In the studied literature, saturation is frequently overlooked in self-commissioning algorithms, especially in the case of **SPMSM** analysis. However, this study reveals that the influence of saturation on inductance identification cannot be disregarded, even for isotropic machines like the **SPMSM**.
- Based on the outcome of this work, the implementation of high-frequency sinusoidal injection aligns more closely with the IEEE standard test when applied to machines with high reactance, rather than those with low reactance.

## 6.2 Limitations

This section discusses the limitations of the results presented in Chapter 5.

- Investigate why the compensation of the inverter non-linearity is achieved at around 60% of the expected theoretical drop (1.8 V instead of 3 V).
- Investigate the reason why the inductance results in higher values if estimated with the self-commissioning algorithms.

## 6.3 Future work

This section addresses the possible improvements that should be prioritized in future work.

- Estimate the magnetizing inductance. The corresponding literature review is given in Section 3.1.2.4 in which some potential methods are proposed. The traditional sinusoidal single-phase test with ([52]) or without ([39]) the DC bias is a possible self-commissioning procedure



to be tested in simulation and experiment. A benchmark for the magnetizing inductance estimate is given by the no-load test from the Standard IEEE 112-2017 [3].

- Automate the procedure. Once the parameters are identified with good accuracy, the procedure should be automated for both machines. The signals are sequentially injected into the electrical drive. This can be done with a state machine in Simulink. A prototype is created for the **SPMSM**. However, the estimation for the **SPMSM** synchronous inductance can be improved. So the final version of the procedure could be further developed. Similarly, the procedure can be automatized for the **IM** once all the techniques for the parameter identification are defined.

Notice that, once the self-commissioning algorithm becomes more complex, the states and their interaction would result in a chaotic vision. A directly coded function is for this reason suggested in place of the state machine.

- Validate the effectiveness of the **FOC** utilizing the newly identified machine parameters obtained through the self-commissioning procedure. Next, contrast this performance with that achieved using gains tuned based on parameters provided by the manufacturer. Finally, assess whether there is an enhancement in control performance.
- Extension to the online estimation of machine parameters, especially for the resistances. As already stated in this report, the temperature considerably affects the value of the resistance, which is a key parameter for control performance. For instance, its variations can be tracked by a resistance observer like in [53].
- Extension to other machines. In this work, both machines have a similar power rating of around 4 kW. A possible future analysis would be to validate the proposed self-commissioning procedure on machines of different power ratings.
- Extension to mechanical parameters identification, important for the tuning of the **SC** in the **FOC** strategy. This project focuses on the electrical parameters as said in Section 1.5. However, the control performance can be further improved if the mechanical aspects are taken into account. Some already existing works present a solution for this

problem such as in [19], which uses signal injection for the parameters estimation.

- Evaluate the impact of the frequency variations on control performance. Possible solutions are proposed in [8] by analyzing the characteristic rotor resistance-slip frequency, or considering the influence on the impedance due to current distribution in the rotor bars like in [36].
- Investigate the effect on control performance of saturation characteristic, if it is considered as a two-variable function of both flux and current such as in [15].
- Test the feasibility of the quasi-steady state technique for the **PM**-flux identification on the **SPMSM**, normally developed for the **SynRM** like in [32].

# References

- [1] P. Vas, *Vector control of AC machines*, ser. Monographs in electrical and electronic engineering ;, 22, Oxford science publications. Clarendon Press ; Oxford University Press, Oxford [England], New York, 1990, 1990. ISBN 0198593708 [Pages 1, 35, 36, 38, 39, and 40.]
- [2] S. A. Odhano, “Self-commissioning of ac motor drives,” *Porto Institutional Repository*, 2014. doi: <https://iris.polito.it/handle/11583/2543100> [Pages 2, 12, 20, 27, 29, 30, 31, 32, 33, 34, 35, 36, 38, 39, 40, 43, 44, 46, and 50.]
- [3] I. Societies and the Standards Coordinating Committee, “Ieee standard test procedure for polyphase induction motors and generators,” *IEEE Std 112-2017 (Revision of IEEE Std 112-2004)*, pp. 1–115, 2018. doi: 10.1109/IEEESTD.2018.8291810 [Pages 2, 4, 12, 34, 36, 37, 39, 41, 64, 67, 99, and 105.]
- [4] S. A. Odhano, P. Pescetto, H. A. A. Awan, M. Hinkkanen, G. Pellegrino, and R. Bojoi, “Parameter identification and self-commissioning in ac motor drives: A technology status review,” *IEEE Transactions on Power Electronics*, vol. 34, no. 4, pp. 3603–3614, 2019. doi: 10.1109/TPEL.2018.2856589 [Pages 2 and 27.]
- [5] IEEE, “Ieee guide for testing permanent magnet machines,” *IEEE Std 1812-2023 (Revision of IEEE Std 1812-2014)*, pp. 1–88, 2023. doi: 10.1109/IEEESTD.2023.10352399 [Pages 4, 28, 29, 31, 33, 34, 55, 57, and 80.]
- [6] L. Harnefors, M. Hinkkanen, and O. Wallmark, *Control of Voltage-Source Converters and Variable-Speed Drives*, Course of Control in Electrical Energy Conversion EJ2230, KTH, 2023. [Page 6.]

- [7] A. Cavagnino, “Electrical machines ii, part of electromechanical constructions, three-phase induction machine,” 2019. [Pages 7, 56, and 96.]
- [8] L. Peretti and M. Zigliotto, “Automatic procedure for induction motor parameter estimation at standstill,” *Electric Power Applications, IET*, vol. 6, pp. 214–224, 04 2012. doi: 10.1049/iet-epa.2010.0262 [Pages 8, 18, 28, 29, 30, 31, 32, 33, 34, 35, 36, 37, 38, 39, 40, 43, 47, 51, 65, 99, and 106.]
- [9] N. Mohan, T. M. Undeland, and W. P. Robbins, *Power Electronics: Converters, Applications and Design*. John Wiley & Sons Inc 1989, 1989. [Page 20.]
- [10] M. Ruff, A. Bunte, and H. Grotstollen, “A new self-commissioning scheme for an asynchronous motor drive system,” in *Proceedings of 1994 IEEE Industry Applications Society Annual Meeting*, vol. 1, 1994. doi: 10.1109/IAS.1994.345457 pp. 616–623 vol.1. [Pages 21 and 35.]
- [11] S. Strobl, N. Cherix, and G. Fernandez, “Rotor field-oriented control (rfoc) of an induction machine,” Jul 2023. [Online]. Available: <https://imperix.com/doc/implementation/rotor-field-oriented-control> [Page 23.]
- [12] K. J. Åström and T. Hägglund, *Advanced PID Controls*. CRC Press, Boca Raton, FL, 1995, 1995. [Page 24.]
- [13] A. Bechouche, H. Sediki, D. Ould Abdeslam, and S. Haddad, “A novel method for identifying parameters of induction motors at standstill using adaline,” *IEEE Transactions on Energy Conversion*, vol. 27, no. 1, pp. 105–116, 2012. doi: 10.1109/TEC.2011.2175393 [Page 28.]
- [14] Y. Shi, K. Sun, L. Huang, and Y. Li, “Online identification of permanent magnet flux based on extended kalman filter for ipmsm drive with position sensorless control,” *IEEE Transactions on Industrial Electronics*, vol. 59, no. 11, pp. 4169–4178, 2012. doi: 10.1109/TIE.2011.2168792 [Page 28.]
- [15] T. Tuovinen, M. Hinkkanen, and J. Luomi, “Modeling of saturation due to main and leakage flux interaction in induction machines,” *IEEE Transactions on Industry Applications*, vol. 46, no. 3, pp. 937–945, 2010. doi: 10.1109/TIA.2010.2045210 [Pages 28, 37, 40, and 106.]

- [16] K. Wang, W. Yao, B. Chen, G. Shen, K. Lee, and Z. Lu, "Magnetizing curve identification for induction motors at standstill without assumption of analytical curve functions," *IEEE Transactions on Industrial Electronics*, vol. 62, no. 4, pp. 2144–2155, 2015. doi: 10.1109/TIE.2014.2354012 [Pages 28, 35, 36, 37, 38, 39, and 40.]
- [17] L. Kalamen, P. Rafajdus, P. Sekerak, and V. Hrabovcova, "A novel method of magnetizing inductance investigation of self-excited induction generators," *IEEE Transactions on Magnetics*, vol. 48, no. 4, pp. 1657–1660, 2012. doi: 10.1109/TMAG.2011.2173312 [Pages 28, 39, and 40.]
- [18] J. Kania, T. Panchal, V. Patel, and K. Patel, "Self commissioning: A unique feature of inverter-fed induction motor drives," *IEEE Transactions on Industrial Electronics*, 12 2011. doi: 10.1109/NUiConE.2011.6153302 [Pages 28, 36, 38, 39, and 40.]
- [19] C. Yang, B. Song, Y. Xie, S. Lu, and X. Tang, "Speed-controller-independent mechanical parameter identification in spmsm drive achieved via signal injection," *IEEE Transactions on Industrial Electronics*, vol. 70, no. 2, pp. 1282–1297, 2023. doi: 10.1109/TIE.2022.3161760 [Pages 29, 30, 33, and 106.]
- [20] Y.-S. Lai and M.-H. Ho, "Self-commissioning technique for high bandwidth servo motor drives," in *2017 IEEE Energy Conversion Congress and Exposition (ECCE)*, 2017. doi: 10.1109/ECCE.2017.8095802 pp. 342–349. [Page 29.]
- [21] N. Bedetti, S. Calligaro, and R. Petrella, "Stand-still self-identification of flux characteristics for synchronous reluctance machines using novel saturation approximating function and multiple linear regression," *IEEE Transactions on Industry Applications*, vol. 52, no. 4, pp. 3083–3092, 2016. doi: 10.1109/TIA.2016.2535413 [Pages 29, 32, 33, 52, and 55.]
- [22] S. Odhano, M. Tang, A. Formentini, P. Zanchetta, and R. Bojoi, "Identification of linear permanent magnet synchronous motor parameters and inverter non-linearity effects," in *2018 International Symposium on Power Electronics, Electrical Drives, Automation and Motion (SPEEDAM)*, 2018. doi: 10.1109/SPEEDAM.2018.8445214 pp. 26–32. [Pages 30 and 31.]
- [23] M. Marchesoni, M. Passalacqua, L. Vaccaro, M. Calvini, and M. Venturini, "Low speed performance improvement in a self-

- commissioned sensorless pmsm drive based on rotor flux observer,” in *2019 21st European Conference on Power Electronics and Applications (EPE '19 ECCE Europe)*, 2019. doi: 10.23919/EPE.2019.8915004 pp. P.1–P.10. [Pages 30, 31, and 32.]
- [24] I. Bojoi, E. Armando, G. Pellegrino, and S. Rosu, “Self-commissioning of inverter nonlinear effects in ac drives,” in *2012 IEEE International Energy Conference and Exhibition (ENERGYCON)*, 2012. doi: 10.1109/EnergyCon.2012.6347755 pp. 213–218. [Pages 31, 33, and 35.]
- [25] M. Vučković, B. Dumnić, V. Vasić, B. Vujkov, and V. Popović, “Inductance identification of the surface permanent magnet synchronous machines with sinusoidal voltage test signals,” in *2021 21st International Symposium on Power Electronics (Ee)*, 2021. doi: 10.1109/Ee53374.2021.9628325 pp. 1–6. [Page 32.]
- [26] H.-J. Lee, J.-E. Joo, and Y.-D. Yoon, “Standstill sensorless self-commissioning strategy of synchronous machine considering rotor rotation reduction technique,” in *2022 International Power Electronics Conference (IPEC-Himeji 2022- ECCE Asia)*, 2022. doi: 10.23919/IPEC-Himeji2022-ECCE53331.2022.9807050 pp. 2694–2700. [Pages 32 and 33.]
- [27] P. Pescetto and G. Pellegrino, “Sensorless magnetic model and pm flux identification of synchronous drives at standstill,” in *2017 IEEE International Symposium on Sensorless Control for Electrical Drives (SLED)*, 2017. doi: 10.1109/SLED.2017.8078434 pp. 79–84. [Pages 32, 33, and 53.]
- [28] L. Ortombina, N. Bianchi, and L. Alberti, “Standstill self-commissioning procedure for synchronous reluctance motors based on coenergy model,” in *2023 IEEE International Electric Machines & Drives Conference (IEMDC)*, 2023. doi: 10.1109/IEMDC55163.2023.10238999 pp. 1–6. [Pages 32 and 33.]
- [29] H.-J. Lee, J.-E. Joo, and Y.-D. Yoon, “Standstill sensorless self-commissioning strategy of synchronous machines including initial positioning and torque canceling techniques,” *IEEE Transactions on Industry Applications*, vol. 59, no. 6, pp. 6817–6825, 2023. doi: 10.1109/TIA.2023.3308090 [Pages 32 and 33.]

- [30] M. Hinkkanen, P. Pescetto, E. Mölsä, S. E. Saarakkala, G. Pellegrino, and R. Bojoi, “Sensorless self-commissioning of synchronous reluctance motors at standstill without rotor locking,” *IEEE Transactions on Industry Applications*, vol. 53, no. 3, pp. 2120–2129, 2017. doi: 10.1109/TIA.2016.2644624 [Pages 32 and 33.]
- [31] ———, “Sensorless self-commissioning of synchronous reluctance motors at standstill,” in *2016 XXII International Conference on Electrical Machines (ICEM)*, 2016. doi: 10.1109/ICELMACH.2016.7732673 pp. 1174–1180. [Pages 32 and 33.]
- [32] P. Pescetto and G. Pellegrino, “Determination of pm flux linkage based on minimum saliency tracking for pm-syr machines without rotor movement,” *IEEE Transactions on Industry Applications*, vol. 56, no. 5, pp. 4924–4933, 2020. doi: 10.1109/TIA.2020.3000710 [Pages 33 and 106.]
- [33] G. B. Reddy, B. P. Muni, and G. Poddar, “Parameter estimation and self-commissioning of high power induction motor drive: Importance with a case study,” in *2020 IEEE International Conference on Power Electronics, Smart Grid and Renewable Energy (PESGRE2020)*, 2020. doi: 10.1109/PESGRE45664.2020.9070520 pp. 1–6. [Pages 35, 36, and 38.]
- [34] H. Schierling, “Self-commissioning-a novel feature of modern inverter-fed induction motor drives,” in *Third International Conference on Power Electronics and Variable-Speed Drives*, 1988, pp. 287–290. [Pages 35, 36, and 38.]
- [35] A. M. Khambadkone and J. Holtz, “Vector-controlled induction motor drive with a self-commissioning scheme,” *IEEE Transactions on Industrial Electronics*, vol. 38, pp. 322–327, 1991. [Online]. Available: <https://api.semanticscholar.org/CorpusID:110610094> [Page 35.]
- [36] Y.-S. Kwon, J.-H. Lee, S.-H. Moon, B.-K. Kwon, C.-H. Choi, and J.-K. Seok, “Standstill parameter identification of vector-controlled induction motor using frequency characteristics of rotor bars,” in *2008 IEEE Industry Applications Society Annual Meeting*, 2008. doi: 10.1109/08IAS.2008.227 pp. 1–7. [Pages 36, 37, 38, 39, and 106.]
- [37] A. Gastli, “Identification of induction motor equivalent circuit parameters using the single-phase test,” *IEEE Transactions on Energy*

- Conversion*, vol. 14, no. 1, pp. 51–56, 1999. doi: 10.1109/60.749147 [Pages 36, 37, and 38.]
- [38] J.-Y. Ruan and S.-M. Wang, “Magnetizing curve estimation of induction motors in single-phase magnetization mode considering differential inductance effect,” *IEEE Transactions on Power Electronics*, vol. 31, no. 1, pp. 497–506, 2016. doi: 10.1109/TPEL.2015.2401835 [Pages 39 and 41.]
- [39] S. A. Odhano, A. Cavagnino, R. Bojoi, and A. Tenconi, “Induction motor magnetizing characteristic identification at standstill with single-phase tests conducted through the inverter,” in *2015 IEEE International Electric Machines & Drives Conference (IEMDC)*, 2015. doi: 10.1109/IEMDC.2015.7409177 pp. 960–966. [Pages 39, 40, and 104.]
- [40] N. Cherix, “Proportional resonant controller,” Oct 2021. [Online]. Available: <https://imperix.com/doc/implementation/proportional-resonant-controller> [Page 51.]
- [41] Z. Wang, K. Lu, and F. Blaabjerg, “A simple startup strategy based on current regulation for back-emf-based sensorless control of pmsm,” *IEEE Transactions on Power Electronics*, vol. 27, no. 8, pp. 3817–3825, 2012. doi: 10.1109/TPEL.2012.2186464 [Page 57.]
- [42] R. Kerkman, J. Thunes, T. Rowan, and D. Schlegel, “A frequency based determination of the transient inductance and rotor resistance for field commissioning purposes,” in *IAS '95. Conference Record of the 1995 IEEE Industry Applications Conference Thirtieth IAS Annual Meeting*, vol. 1, 1995. doi: 10.1109/IAS.1995.530322 pp. 359–366 vol.1. [Page 63.]
- [43] S. Strobl, J. Orsinger, and S. Lovejoy, “Motor testbench quick start guide,” Aug 2023. [Online]. Available: <https://imperix.com/doc/help/motor-testbench-quick-start-guide> [Pages 70, 81, and 97.]
- [44] SEW, “Ac motors, asynchronous motors,” 2023. [Online]. Available: [https://www.seweurodrive.com/products/motors/ac\\_motors/ac\\_motors.html](https://www.seweurodrive.com/products/motors/ac_motors/ac_motors.html) [Pages 73 and 96.]
- [45] —, “Cm3c.. series synchronous servomotors,” 2023. [Online]. Available: [https://www.seweurodrive.com/products/servo\\_drive\\_tech](https://www.seweurodrive.com/products/servo_drive_tech)



nology/servomotors/synchronous-servomotors-cm3c/synchronous-servomotors-cm3c.html [Page 73.]

- [46] *Rotating electrical machines - Part 8: Terminal markings and direction of rotation*, International Electrotechnical Commission IEC Standard 60 034-8, 2007. [Page 74.]
- [47] Brymen, “Brymen bm785,” 2023. [Online]. Available: <https://brymen.eu/shop/bm785/> [Page 80.]
- [48] *MCR5000 series User Manual*, MATRIX TECHNOLOGY INC., 9 2019. [Page 88.]
- [49] Rigol, “Digital oscilloscope mso5074,” 2023. [Online]. Available: <https://rigolshop.eu/product/oscilloscope/mso5000/mso5074.html> [Page 91.]
- [50] Micsig, “Micsig dp series high voltage differential probe\_dp10007/dp10013/dp20003,” 2023. [Online]. Available: <https://www.micsig.com/Differential%20Probe04/> [Page 91.]
- [51] —, “Low frequency ac/dc current probe cp2100 series,” 2023. [Online]. Available: <https://www.micsig.com/current%20probe/> [Page 97.]
- [52] J. Ruan and S. Wang, “A prediction error method-based self-commissioning scheme for parameter identification of induction motors in sensorless drives,” *IEEE Transactions on Energy Conversion*, vol. 30, no. 1, pp. 384–393, 2015. doi: 10.1109/TEC.2014.2346198 [Page 104.]
- [53] S. Wang and M. Lin, “A novel stator resistance online identification method based on adrc,” in *2021 IEEE 4th Student Conference on Electric Machines and Systems (SCEMS)*, 2021. doi: 10.1109/SCEMS52239.2021.9646154 pp. 1–3. [Page 105.]



# Appendix A

## Electrical machines specifications

Table A.1: Main specifications of the **IM**.

Characteristic	Symbol	@50 Hz	Unit
Pole pairs	$n_p$	2	-
Rated line voltage	$V_{LL, N}$	380	V
Rated power	$P_N$	4	kW
Rated torque	$\tau_N$	26	Nm
Rated speed	$n_N$	1464	rpm
Rated current	$I_N$	8.4	A
Power factor	$\cos \varphi$	0.81	-
Starting torque ratio	$\tau_A/\tau_N$	2.4	-
Starting current ratio	$I_A/I_N$	8.2	-
Moment of inertia	$J$	178	kg cm <sup>2</sup>

Table A.2: Parameters of the **IM** steady-state T-equivalent circuit.

Characteristic	Symbol	Value	Unit
Stator resistance	$R_s$	1.24	$\Omega$
Stator leakage inductance	$L_{ls}$	11.5	mH
Mutual inductance	$L_m$	183	mH
Rotor resistance	$R_r$	0.73	$\Omega$
Rotor leakage inductance	$L_{lr}$	11.5	mH

Table A.3: Main specifications of the **SPMSM**.

Characteristic	Symbol	@50 Hz	Unit
Pole pairs	$n_p$	4	-
Rated line voltage	$V_{LL, N}$	400	V
Rated power	$P_N$	4.8	kW
Rated torque	$\tau_N$	22.8	Nm
Rated speed	$n_N$	2000	rpm
Rated current	$I_N$	11.2	A
Maximum torque	$\tau_m^{max}$	68.4	Nm
Maximum speed	$n_m^{max}$	2750	rpm
Maximum current	$I_N^{max}$	34.9	A
Moment of inertia	$J$	40.6	kg cm <sup>2</sup>

Table A.4: Parameters of the **SPMSM** steady-state equivalent circuit.

Characteristic	Symbol	Value	Unit
Stator resistance	$R_s$	0.559	$\Omega$
Synchronous inductance	$L_s$	4.24	mH
<b>PM</b> -flux	$\psi_r$	0.2748	Wb



